5-2014

Fault and Fluid Interactions in the Elsinore Fault-West Salton Detachment Fault Damage Zones, Agua Caliente County Park, California

Rebekah Erin Wood
Utah State University

FAULT AND FLUID INTERACTIONS IN THE ELSINORE FAULT-WEST SALTON DETACHMENT FAULT DAMAGE ZONES, AGUA CALIENTE COUNTY PARK, CALIFORNIA

by

Rebekah E. Wood

A thesis submitted in partial fulfillment
of the requirements for the degree

of

MASTER OF SCIENCE

in

Geology

Approved:

_____	_____
Dr. James P. Evans Major Professor	Dr. Mary S. Hubbard Committee Member
_____	_____
Dr. Dennis Newell Committee Member	Dr. Mark R. McLellan Vice President for Research and Dean of the School of Graduate Studies

UTAH STATE UNIVERSITY
Logan, Utah

2014

ABSTRACT

Fault and Fluid Interations in the Elsinore Fault-West Salton Detachment Fault Damage Zones, Agua Caliente County Park, California

by

Rebekah E. Wood, Master of Science

Utah State University, 2014

Major Professor: James P. Evans
Department: Geology

This study area provides a unique opportunity to study the intersection of the Elsinore and West Salton detachment faults in southern California, effusing warm springs, and alteration products in the midst of the fault intersection. Structural mapping and compiling previous maps supply an interpretation of the fault zone geometries within the Tierra Blanca Mountains. Geochemical analysis of the crystalline basement and altered protolith help determine the effects of faulting and fluid flow in the study area.
In the Tierra Blanca Mountains, the Elsinore strike-slip fault system transitions from the double-stranded Julian segment and Earthquake Valley fault in the northwest, to the single-stranded Coyote Mountain segment in the southeast. A network of cross faults striking northeast connects the fault segments. The Coyote Mountain segment encounters the inactive West Salton detachment fault in the study area. The detachment fault is a barrier to fluid flow and exhibits primarily brittle deformation, while the Coyote Mountain segment is a conduit for fluid flow along the northeastern flank of the Tierra Blanca Mountains. The damage zone of the Coyote Mountain segment reaches widths up to 500

m and contains intense fracturing and subsidiary faults striking parallel to the main trace. The tonalite protolith is bleached, stained, and altered from water-rock interactions. The most intense bleaching is at a county park, where the protolith is altered to clays and zeolites while the mineralogy of the stained regions contains iron oxides and clinochlore in addition to quartz, Ca-rich albite, and biotite preserved from the protolith.

The water chemistry at Agua Caliente hot springs shows the fluid is partially equilibrated. Groundwater temperatures likely reached 75-85°C at depths up to 2.14 km before rising to the surface. Frequent seismicity in the study region is related to the spring characteristics including water level, conductivity, and temperatures. Spring temperature and conductivity displayed three behaviors during the summer 2011 logging period, attributed to seasonal changes and most likely local seismicity as well. Conductivity seems to be the property most influenced by earthquake activity in the area. Changes in fluid chemistry between sampling periods may indicate mixture with other fluid sources.

(142 pages)

PUBLIC ABSTRACT

Fault and Fluid Interations in the Elsinore Fault-West Salton Detachment Fault Damage Zones, Agua Caliente County Park, California

by

Rebekah E. Wood, Master of Science

Utah State University, 2014

Major Professor: James P. Evans
Department: Geology

The Elsinore fault in southern California presents seismic hazards from the Los Angeles Basin southeast to the United States-Mexico border. The Julian and Coyote Mountain segments of the Elsinore fault bound the Tierra Blanca Mountains, and cross faults connect the two faults. On the eastern side of the range, the Coyote Mountain segment intersects the older, inactive West Salton detachment fault in the northern regions of the Tierra Blanca Mountains, and their intersection corresponds with several natural springs which are currently utilized for recreational pools. The meteorically-sourced springs emerge at the fault intersection and correspond with alteration of the granite to clay and iron staining. In this work, I address the geometry of the fault intersection, determine specific compositions of alteration associated with the fault zones and springs, and compare spring behavior with local microseismic events. Groundwater temperatures likely reached 75-85°C at depths up to 2.14 km before rising to the surface. Frequent seismicity in the study region influences water level, conductivity, and temperature behaviors. Spring temperature and conductivity display three signatures during the sum-

mer 2011 logging period, attributed to seasonal changes and local seismicity. Water level seems to be the property most influenced by earthquake activity in the area and increases after earthquakes. Ion concentrations and pH changed between sampling periods and may be related to how much fluid is moving through the area and how long the fluid remains within the granite. In such an arid region, water sources and migration pathways are very important to document.

(142 pages)

to my father, Bruce Wood,
who encouraged me to give geology a chance

ACKNOWLEDGMENTS

This research was funded through the Southern California Earthquake Center (SCEC). Jim Evans proposed and received funding for this research and his guidance has been invaluable. He has been the perfect adviser. I am grateful to my committee members, Mary Hubbard and Dennis Newell, for their time, input, and guidance. Susanne Janecke also offered significant guidance. I want to thank my willing field hands, Tamara Jeppson and Bruce Wood. Eric Mustonen graciously opened his home in Borrego Springs for our use while doing fieldwork. Mikayla Reid eagerly assisted in XRD sample preparation. I am thankful for Mark Stockdale's kindness, stories, and American Indian music. Tom Lachmar and Jerry Fairley were so helpful with their input on water sampling and analysis. Brennan Young helped calculate geothermometer values. Myles helped with accessing the spring box at Agua Caliente County Park. Gary O'Brien and Chris Sant helped me set up and run the XRD. I am grateful my family and friends encouraged me to continue my education. My experience at Utah State University has been one of significant growth, for which I am very thankful.

-Rebekah E. Wood

ABSTRACT....iii

PUBLIC ABSTRACT....v

ACKNOWLEDGMENTS....viii

LIST OF TABLES....xi

LIST OF FIGURES....xii

INTRODUCTION....1

RESEARCH OBJECTIVES....5

MOTIVATION....6

GEOLOGIC SETTING....8

DATA COLLECTION METHODS....20

- Structural Analysis....20
- Water Sampling & Analysis....24

RESULTS....30

- Macroscale Observations....30
- Mesoscale Observations....34
- Microscale Observations....64
- Fluid Chemistry....71
- Local Seismicity....79
- Protolith Alteration and Distribution....81

DISCUSSION....90

- Macroscale Interpretations....90
- Mesoscale Interpretations....92
- Microscale Interpretations....96
- Water Chemistry....98
- Protolith Alteration....102
- Earthquake Activity....108

CONCLUSIONS....110

REFERENCES.....114

APPENDICES.....124

Appendix A: Thin Section Descriptions..... 125
Appendix B: Water Chemistry.....CD
Appendix C: Earthquakes.....CD
Appendix D: X-Ray Diffraction.....CD

PLATE 1.....Pocket

LIST OF TABLES

Tables Page

1 Slip rates for faults in southern California.....13

2 Mineralogic facies within the La Posta pluton..... 15

3 A summary of water data collected during 2011.....25

4 A summary of water data collected during 2011.....26

5 Water elemental analysis concentrations in mg/L processed by USUAL.....28

6 Elemental concentrations in weight per volume and molality.....29

7 A summary of scanline data..... 68

8 Scanline data for the three scanlines in the Tierra Blanca Mountains..... 69

9 XRD interpreted minerals..... 84

10 Alteration reaction pathways if calculated at standard state..... 104

11 Water Chemistry reported by Agua Caliente County Park..... 105

LIST OF FIGURES

Figures Page

1 Fault zones geometry..... 2

2 Southern San Andreas fault system.....9

3 Fault traces in the Vallecito Valley and Tierra Blanca Mountains..... 11

4 Facies of the La Posta pluton.....14

5 View from Agua Caliente County Park.....17

6 Groundwater basins.....18

7 Agua Caliente County Park.....19

8 Geochemistry transect.....22

9 Spring box.....27

10 Focal mechanisms.....31

11 Northwest Tierra Blanca Mountains.....32

12 Stereonet parallel to the Coyote Mountain segment.....33

13 Cross sections through the Tierra Blanca Mountains..... 35

14 Canebrake Conglomerate and Palm Spring Formation..... 36

15 Undeformed La Posta tonalite..... 38

16 Damage within canyons..... 39

17 Stereonet of fractures in an arroyo close to the Carrizo Valley.....40

18 The La Posta pluton unaltered from fluid flow..... 41

19 Mesoscale study index map..... 42

20 Site 1 Vallecito Valley..... 43

21 Site 2 Marsh Canyon....45

22 Site 3 North of the county park....46

23 West Salton detachment fault surface orientation....47

24 Site 4 West Salton detachment fault....49

25 Site 5 Shuffleboard fault....51

26 Site 6 Moonlight Canyon....53

27 Site 7 Moonlight Canyon....55

28 Site 8 Cross faults related to the Coyote Mountain segment....56

29 Site 9 Coyote Canyon....57

30 Site 10 Cross fault....59

31 Site 11 Mountain front fault....60

32 Site 12 Bighorn Canyon....61

33 Site 13 Canebrake Canyon....63

34 Scanline in Marsh Canyon....65

35 Scanline in Moonlight Canyon....66

36 Scanline in Coyote Canyon....67

37 Thin section behaviors....70

38 Entrained biotite....71

39 Thin sections....72

40 Subsidiary fault from Site 9....73

41 $\delta^{13}C$ (‰) sources....74

42 Water types based on δD and $\delta^{18}O$ trends....75

43 Spring and local earthquake data from February 2011.....76

44 Spring and local earthquake data from summer 2011.....76

45 Geochemical gradient.....79

46 Earthquake 10 km in radius from the spring box during February 2011.....85

47 Earthquakes 5 km in radius from the spring box during summer 2011.....86

48 Earthquakes 10 km in radius from the spring box during summer 2011.....87

49 Two-dimensional and three-dimensional plots of seismic events.....88

50 Block diagram of the West Salton detachment and Elsinore fault zones.....89

51 Fault stepover geometries.....92

52 Cross fault geometries.....94

53 Geothermal gradient in the Peninsular Ranges batholith.....95

54 Piper diagram from cation and anion concentrations.....99

55 Na-K and K-Mg equilibrium temperatures.....100

INTRODUCTION

Determining the interactions between fluid flow and fault zones offers insight into seismic and fault slip history, fluid migration, mineral alteration, and deformation. Fault zones are often, or can be thought of, composed of a highly deformed fault core, a transitional damage zone, and an undeformed protolith (Figure 1; Chester and Logan, 1986; Caine et al., 1996; Anderson and Fairley, 2008). A fault core can be a series of roughly parallel surfaces hosting primary slip, or may not be clearly present, or be a localized single slip surface surrounded by cataclasite or ultracataclasite (Finzi et al., 2009). Damage zones are characterized by high densities of fractures, discontinuous subsidiary faults, pulverized rocks, mineralized veins (Kim et al., 2003; Finzi et al., 2009), abandoned primary slip surfaces (Sadler et al., 1993), and regions of increased pore space and enhanced permeability (Micklethwaite and Cox, 2004; Finzi et al., 2009). The intensity of damage typically decays with distance from the main fault trace, a relationship observed on all scales (Chester and Logan, 1986; Schulz and Evans, 1998; Faulkner et al., 2011). Fault damage zones contain records of seismicity, slip history, fluid migration, deformation, and alteration (Shipton and Cowie, 2003). Damage zone widths may be asymmetric, with wider damage on the hanging wall than the footwall or vice versa, and some workers associate width with fault zone maturity (Odling et al., 2004; Dor et al., 2006; Bailey et al., 2010).

Together, fault cores and fault damage zones behave as a conduit, a barrier, or both to migrating fluids (Caine et al., 1996; Evans et al., 1997; Fairley and Hinds, 2004; Shipton et al., 2005; Faulkner et al., 2010), and the fluids can increase pore pressure and

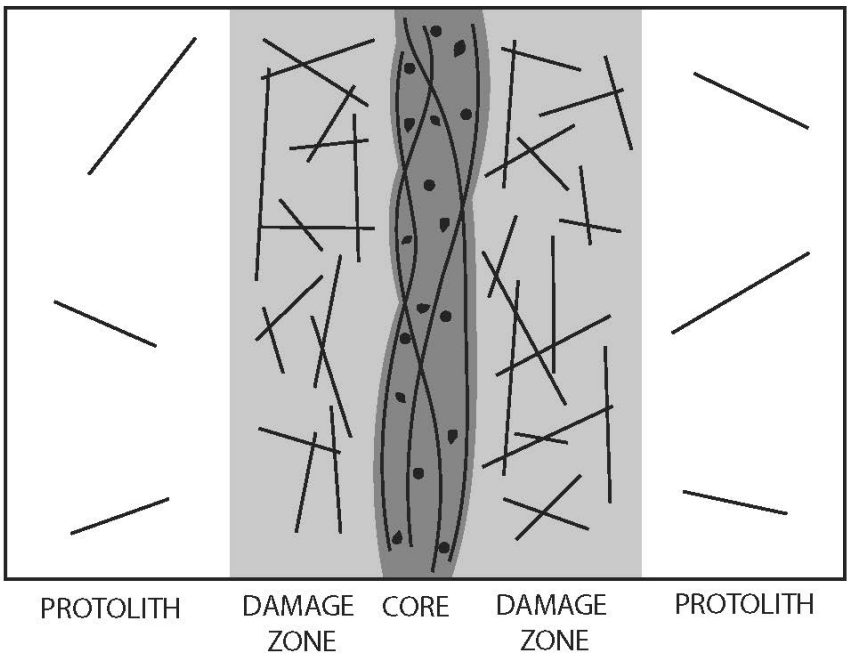

Figure 1 Fault zones are often defined by a core and adjacent damage zone that gradually returns to the undeformed protolith.

weaken the fault (Fairley et al., 2003; Faulkner et al., 2006; Manga and Wang, 2007). Subsurface fluids such as water or petroleum flow toward zones of high permeability and are expressed at the surface as seeps, springs, ponds, or reservoirs, and if the average water temperature is greater than the annual average temperature of the ground surface, it is a thermal spring. If fluids migrating through or residing within cracks in the damage zone are in disequilibrium with the host rock, and if their residence time is sufficient, dissolution or alteration of the host rock and precipitation of dissolved minerals from the fluids may occur (Oliver and Bons, 2001). Mineral assemblages formed along the fault core and within the damage zone can change the nature of faulting (Caine et al., 2010) and are a result of the fluid-rock interactions (McCaig, 1984). The development of clays along a fault plane may inhibit or cease migration of fluids across faults (Bouvier and Kaars-Sijpesteijn, 1989).

Generally, permeability decreases in granites as heated fluids migrate through the rock as the fluids dissolve and precipitate minerals along migration pathways (Vaughan et al., 1986) so the presence of thermal springs likely influences the ability for effective flow through the protolith. Evans et al. (2005) observed a correlation between permeability growth along faults and hydrothermal alteration in a granitic protolith which promotes the idea that the increased fracturing from faulting creates conduits for fluid flow and alteration occurs in zones of enhanced permeability. Fluids in fault zones usually move during or after seismicity, and most of the fluid flow occurs in aftershock zones because these zones maintain increased porosity for a longer period of time than main traces (Micklethwaite and Cox, 2004).

Damage zone formation and evolution record history of slip along fault zones, and the extent of fractures and subsidiary faults into the protolith may be proportional to slip and fault length (Fairley and Hinds, 2004; Odling et al., 2004; Andrews, 2005; Shipton et al., 2005; Savage and Brodsky, 2011). Damage zone widths and fault slip rates are variable along strike (Caine et al., 1996; Evans et al., 1997; Schulz and Evans, 1998; Fairley and Hinds, 2004; Faulkner et al., 2010). Fault slip rates vary for many reasons: separate segments of the fault zone have different geometry; the host rock encountered may change, and often does, along the fault zone; the slip surface may have significant roughness that controls frictional strength of the fault in that area (Power and Tullis, 1992; Kim et al., 2004); there may be thermal anomalies and different depths of the brittle-ductile transition within the lithosphere (Ehlers and Chapman, 1999); and faults may behave differently when they intersect with preexisting deformation or faulting (Shipton and Cowie, 2003).

When fault zones meet, the intersection zone can be quite complex (Dor et al., 2006). Much like water flowing down a path of least resistance, faults tend to form, break, and slip along the easiest course, so as faults intersect, the most recent fault may reuse the preexisting fault trace as a way to distribute strain until it continues its expression of stress. The younger fault may, however, cross-cut and displace the older fault without using its trace. The observed geometry of fractures and interpretation of fault growth largely depends on angles between the faults, dip direction, fault depths, the extent of annealing along the older fault, geometry at depth, whether both faults experience active slip, predominant stress regime, protolith, and unit thicknesses (Savage and Brodsky, 2011).

RESEARCH OBJECTIVES

The objectives of this study are 1) to identify the evidence for past and present interactions between fluids and fault-related rocks, 2) to determine how fluids may have influenced fault behavior, and 3) to establish a standard set of water sampling tests monitoring fluid composition variations, temperature and conductivity fluctuations, and changing flow rates. Questions driving this work include:

1. Is the damage on the Elsinore fault or the West Salton detachment fault at Agua Caliente County Park the result of slip along one or both faults or localized at the intersection between the two?
2. Does fault-related damage vary measurably from the detachment fault to the Elsinore fault zone? Does the damage vary with lithology of the host rock?
3. Is damage proportional to the amount of slip?
4. Does the geometry of the fault intersection control the location of, or is it related to, fluid accumulation, and does alteration of the protolith occur because it is in disequilibrium with the thermal fluids remaining in the protolith?
5. Are changes in modern water chemistry and alteration a result of or related to active deformation and local seismicity?

MOTIVATION

The faults within the Tierra Blanca Mountains, the altered protolith, the local seismicity, and the active warm springs at Agua Caliente County Park, San Diego County, California present an ideal location to observe the interactions between fluids, earthquakes, alteration, and fault damage zones. Many workers have documented damage zones and fluids, springs, or alteration present within fault cores or fault damage zones (e.g. Chester et al., 1993; Evans and Chester, 1995; Curewitz and Karson, 1997; Schulz and Evans, 1998; Billi et al., 2003; Hamaker, 2005; Hayman, 2006; Heffner and Fairley, 2006; Anderson and Fairley, 2008; Bellot, 2008; Brodsky et al., 2009; Caine et al., 2010; Faulkner et al., 2010). This work continues the theme of geological and hydrological fault zone studies by examining deformed rocks and warm springs emerging at the base of the northeastern Tierra Blanca Mountains, where the springs are focused at the intersection of two intersecting faults. The Elsinore fault experiences microseismic events almost daily in the region around our study area (SCEC Earthquake Catalog, 2012) while the West Salton detachment fault is inactive and cut by the more recent high-angle strike-slip faulting (Todd, 1977; Axen and Fletcher, 1998; Todd, 2004; Dorsey et al., 2011).

Numerous researchers have studied subsurface fluid properties to use as potential earthquake predictors by tracking hydrogeochemical shifts surrounding seismic episodes (Claesson et al., 2004, 2007), recording the movement of hydrothermal fluids (Claesson et al., 2004; Hartmann et al., 2005; Claesson et al., 2007; Manga and Wang, 2007; Inan et al., 2008; Suer et al., 2008; Cicerone et al., 2009; Manga and Rowland, 2009), and observing the effects of fluid pressure on fault nucleation and rupture (Sibson, 1981, 1992).

I attempt to examine the relationship between seismicity and hydrologic processes at Agua Caliente County Park, southern California by measuring spring characteristics (water level, temperature, conductivity, stable isotopes of deuterium, Oxygen-18, and Carbon-13, and major ion concentrations) and comparing them to local earthquakes. These data begin a hydrogeochemical database that I compare with local seismicity. Though weekly sampling of the spring is not feasible, the tests I completed may reveal seemingly insignificant changes that become more significant as hydrogeochemical research expands. Water is highly important in deserts, and the water accumulating at the arid Tierra Blanca Mountains impacts the sustainability of the county park, influences water availability to local residents, enables vegetation to grow, and provides a watering hole for the local wildlife.

GEOLOGIC SETTING

The study area for this research is located at the transition from ocean spreading in the Gulf of California to right-lateral strike-slip motion along western California between the Pacific and North American tectonic plates (Atwater, 1970; Elders et al., 1972). The Elsinore fault is the westernmost major strand of the right-lateral strike-slip southern San Andreas fault system in southern California (Figure 2; Jahns, 1954; Fay and Humphreys, 2005; Steely et al., 2009; Blisniuk et al., 2010; Janecke et al., 2010; Jennings and Bryant, 2010). Geodetic data shows the Elsinore fault accommodates ~ 2-6 mm of slip per year—far less than its sister faults, the southern San Andreas and the San Jacinto faults which accommodate 10-35 mm of slip each year (Blisniuk et al., 2010). The Elsinore fault is composed of six segments in the United States (Figure 2; Dawson et al., 2008), but this work focuses on the southern double-stranded Julian and the Coyote Mountain segments which have experienced 1-2 km of total horizontal displacement (Grove et al., 2003; Dorsey et al., 2012). The Julian segment makes a left step to the Coyote Mountain segment at the Tierra Blanca Mountains (Figure 3; Magistrale and Rockwell, 1996), and

Figure 2 (Following page) The Southern San Andreas fault system is composed of four fault systems. From east to west they are the Southern San Andreas fault zone, the San Jacinto fault zone, The San Felipe fault zone, and the Elsinore fault zone. The Elsinore fault system is composed of the Whittier fault, Chino fault, Glen Ivy segment, Temecula segment, Julian segment, the Earthquake Valley fault, Coyote Mountain segment, and the Laguna Salada fault in northern Mexico (not shown). The Earthquake Valley fault and the Julian segment form a double-stranded section of the Elsinore fault zone. The double-stranded zone transitions to the single-stranded Coyote Mountain segment at the Tierra Blanca Mountains. The San Andreas fault system is the easternmost major fault system in the Southern San Andreas fault network, and it terminates east of the Salton Sea. The study area is boxed in red. This fault map is modified from the 2010 Fault Activity Map of California by Jennings and Bryant.

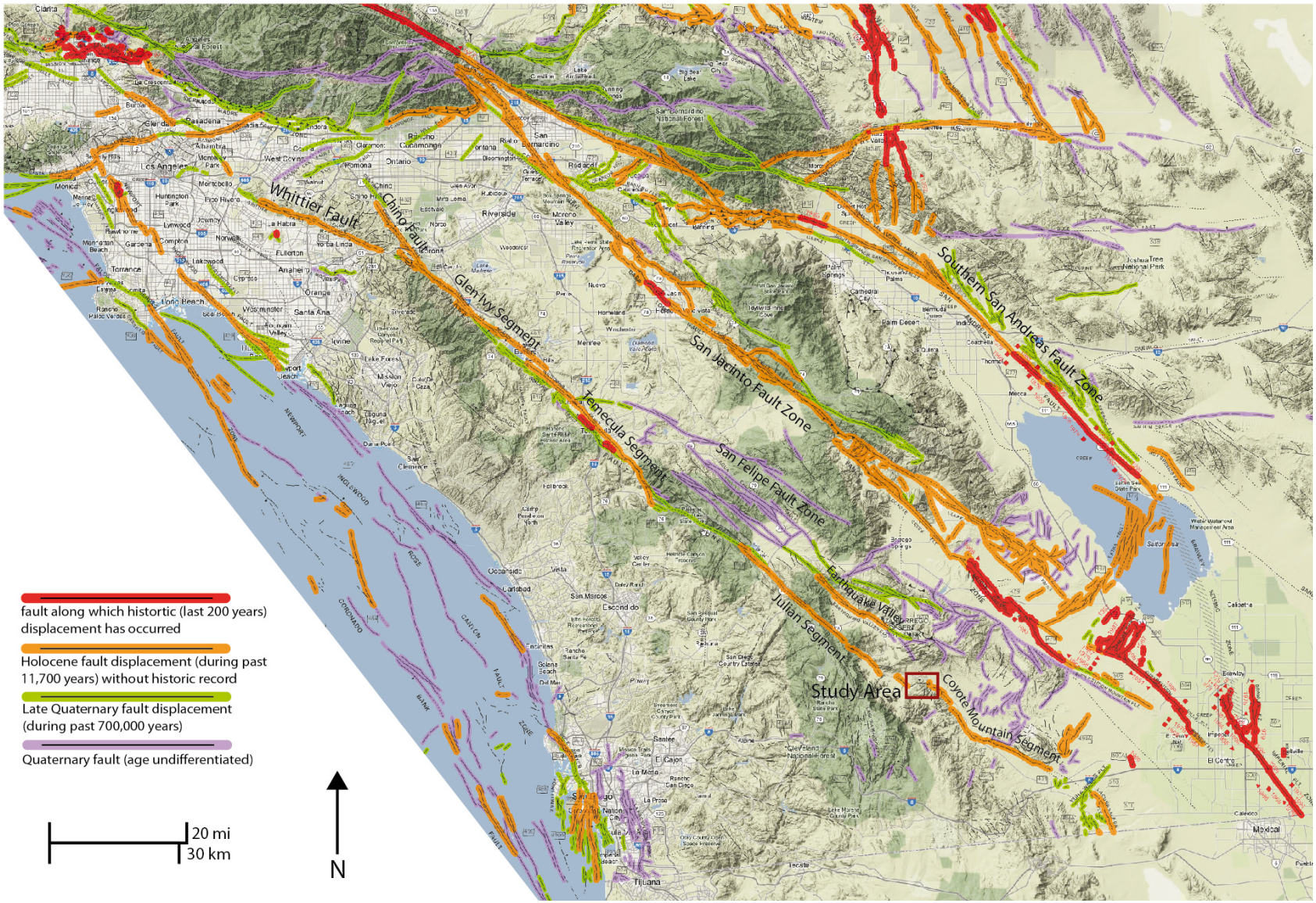
Whittier Fault
Chino Fault
Glen Ivy Segment
Temecula Segment
San Jacinto Fault Zone
San Felipe Fault Zone
Julian Segment
Earthquake Valley
Coyote Mountain Segment
Southern San Andreas Fault Zone
Study Area
fault along which historic (last 200 years) displacement has occurred
Holocene fault displacement (during past 11,700 years) without historic record
Late Quaternary fault displacement (during past 700,000 years)
Quaternary fault (age undifferentiated)
20 mi
30 km
N

the Coyote Mountain segment intersects the southern extent of the inactive West Salton detachment fault, a north-striking, low-angle normal fault responsible for most of the extension in the Salton Trough until ~ 2 mya (Figure 3; Shirvell et al., 2009).

In the northwestern part of the study area, the Julian segment is mapped as entering the Tierra Blanca Mountains on the northwest (Todd, 1977) and its trace continues through the tonalite and into the covered Inner Pasture (Allison et al., 1978) on the southwest flank of the mountain range. The northern extent of the Coyote Mountain segment begins ~ 3.3 km northwest of the county park and strikes southeast along the northeastern flank of the mountain range. North of the mountains, the right-lateral Earthquake Valley fault strikes through Earthquake Valley, parallels the Julian segment of the Elsinore fault, and enters the Vallecito Mountains northeast of Whale Peak where it meets, but does not appear to cut, the West Salton detachment fault (Kairouz, 2005). Within the Vallecito Mountains the Earthquake Valley fault transitions to a network of cross faults which strike ~ N25°E to N55°E through the mountains. The dominant strike is ~ N45°E (Figure 3). The cross faults are strike-slip-oblique and form linear canyons striking northeast-

Figure 3 (Following page) Fault traces in the Vallecito and Tierra Blanca Mountains overlying a Landsat image showing general rock types. The black faults are strike-slip and strike-slip-oblique faults related to the Elsinore fault system. The detachment fault exhibits predominately top-to-the-east slip (Axen and Fletcher, 1998). The faults in the Tierra Blanca Mountains have two consistent strike orientations: northeast and southeast. Faults in the Vallecito Mountains strike predominately east-northeast and southeast. Earthquakes cluster in the southeast Tierra Blanca Mountains in the Carrizo Valley. The Coyote Mountain segment of the Elsinore fault has a consistent southeast strike. They also cluster in Vallecito Valley north of the Tierra Blanca Mountains and adjacent to the southern Vallecito Mountains at the intersections of northeast-striking left-lateral and southeast-striking right-lateral strike-slip faults. The earthquakes occurred between June 9 and August 22, 2011. The faults are from Kairouz (2005), Todd (1977), Axen (unpublished, with permission), aerial mapping using Google Earth, and personal field mapping.

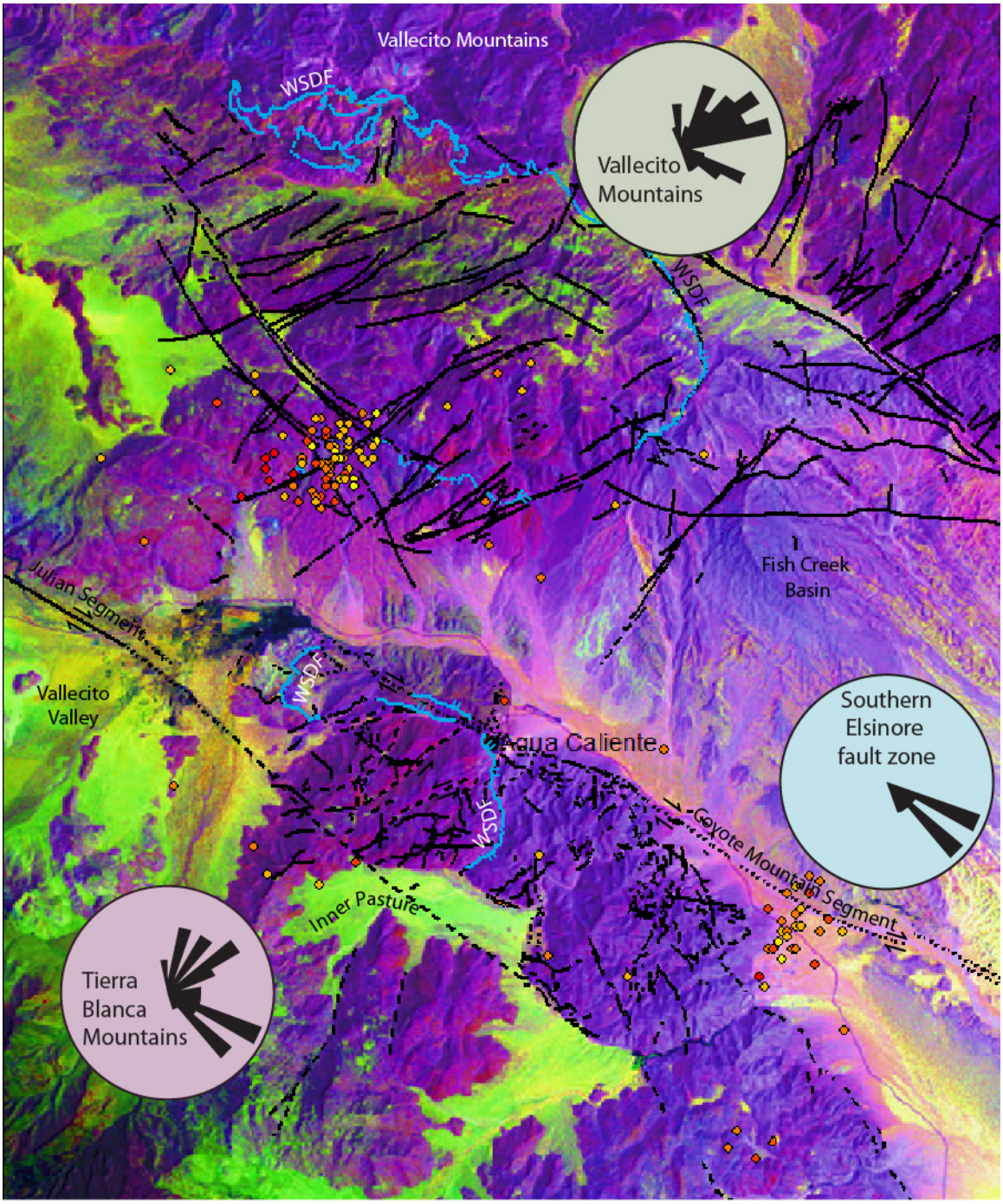
Vallecito Mountains
WSDF
Vallecito Mountains
WSDF
Fish Creek Basin
Julian Segment
Vallecito Valley
WSDF
Agua Caliente
Southern Elsinore fault zone
WSDF
Coyote Mountain Segment
Inner Pasture
Tierra Blanca Mountains
Alluvium, Valley fill
Palm Spring Formation & Canebrake Conglomerate
La Posta pluton
Prebatholithic Schist & Gneiss
5 miles
concealed fault
inferred fault
fault
West Salton detachment fault
Earthquakes Mw (0.3-3.63)

southwest (Figure 3). Kairouz (2005) also mapped small arrays of fault segments striking northeast-southwest forming scarps in the alluvial fans north of Vallecito County Park in Vallecito Valley. The Earthquake Valley fault network either dies out in the Vallecito Mountains or continues as the Hapaha Flat fault southeast of the Vallecito Mountains (Dorsey et al., 2012). Similar cross faults exist within the Tierra Blanca Mountains.

Fletcher and others (2011) determined the slip rate for the Coyote Mountain segment, based on ^{230}Th/U dating of pedogenic carbonate clasts, to be 1.6 ± 0.4 mm/yr. The Coyote Mountain segment experiences less strain than northerly segments (Fletcher et al., 2011). Researchers propose slip rates decrease in the southern regions of the Elsinore fault system because displacement is transferred and strain is accommodated on the Earthquake Valley and the San Felipe faults to the east of the Julian segment (Table 1; Vaughan et al., 1999; Grove et al., 2003; Dawson et al., 2008; Janecke et al., 2010; Dorsey et al., 2012).

The protolith of the Tierra Blanca Mountains is the La Posta tonalite, the largest pluton in the Peninsular Ranges batholith, which was emplaced 94 ± 2 Ma based on U-Pb zircon dating (Figure 4; Walawender et al., 1990; Miller, 1994; Catlos et al., 2000). The rock comprises subhedral plagioclase, alkali feldspar, quartz, biotite, sphene, allanite, epidote, apatite, and zircon (Todd, 1977; Clinkenbeard, 1987; Clinkenbeard and Walawender, 1989). A small area in the northeastern Tierra Blanca Mountains is bleached white providing the range's namesake, but away from the bleached rock, the plutonic rocks are red-brown and highly fractured (Figure 5; Todd, 1977). The bleached area is white and is fractured until it is friable. Grain size reductions and compositional changes lead to the formation of dark green mineralized surfaces striking parallel to the fault sur-

Table 1 Slip rates for faults in southern California.

Slip Rates along the Elsinore Fault & Other Neighboring Faults				
Fault	Length (km)	Type of Slip	Slip Rate (mm/yr)	Reference
Whittier Segment	36	rl/ss	2.5 ± 1.0	Petersen et al., 1996; Field, 2007
Chino Segment	20	rl/ss-oblique	1.0 ± 1.0	Petersen et al., 1996; Treiman and Lundberg, 1998; Field, 2007
			1.0-5.0	Treiman and Lundberg, 1998
			0.06	Treiman and Lundberg, 1998; Heath et al., 1982
			0.14-0.25	Treiman and Lundberg, 1998
			<2.0	Treiman and Lundberg, 1998
			0.3-0.5	Treiman and Lundberg, 1998
Temecula Segment	62	rl/ss	5.0 ± 2.0	Petersen et al., 1996; Treiman and Lundberg, 1998; Field 2007
Glen Ivy Segment	46	rl/ss	5.0 ± 2.0	Petersen et al., 1996; Treiman and Lundberg, 1998; Field, 2007
			5.6	Magistrale and Rockwell, 1996
Julian Segment	79	rl/ss	1.0-5.0	Treiman and Lundberg, 1998
			5.0 ± 2.0	Petersen et al., 1996
			3.0 ± 1.0	Field, 2007
Coyote Mountain Segment	33	rl/ss	4.0 ± 2.0	Petersen et al., 1996; Treiman and Lundberg, 1998
			1.6 ± 0.4	Fletcher et al., 2011
			3.0 ± 1.0	Field, 2007
			3.3-5.5	Magistrale and Rockwell, 1996
Laguna Salada Fault	61	rl/ss	3.5 ± 1.5	Petersen et al., 1996; Treiman and Lundberg, 1998; Field, 2007
Earthquake Valley Fault	25	rl/ss	2.0 ± 1.0	Petersen et al., 1996; Field, 2007
Southern San Andreas Fault	(1200)	rl/ss	25 ± 3	Fialko, 2006
			16 ± 2	Lindsey and Fialko, 2010
San Jacinto Fault	210	rl/ss	21 ± 3	Lindsey and Fialko, 2010

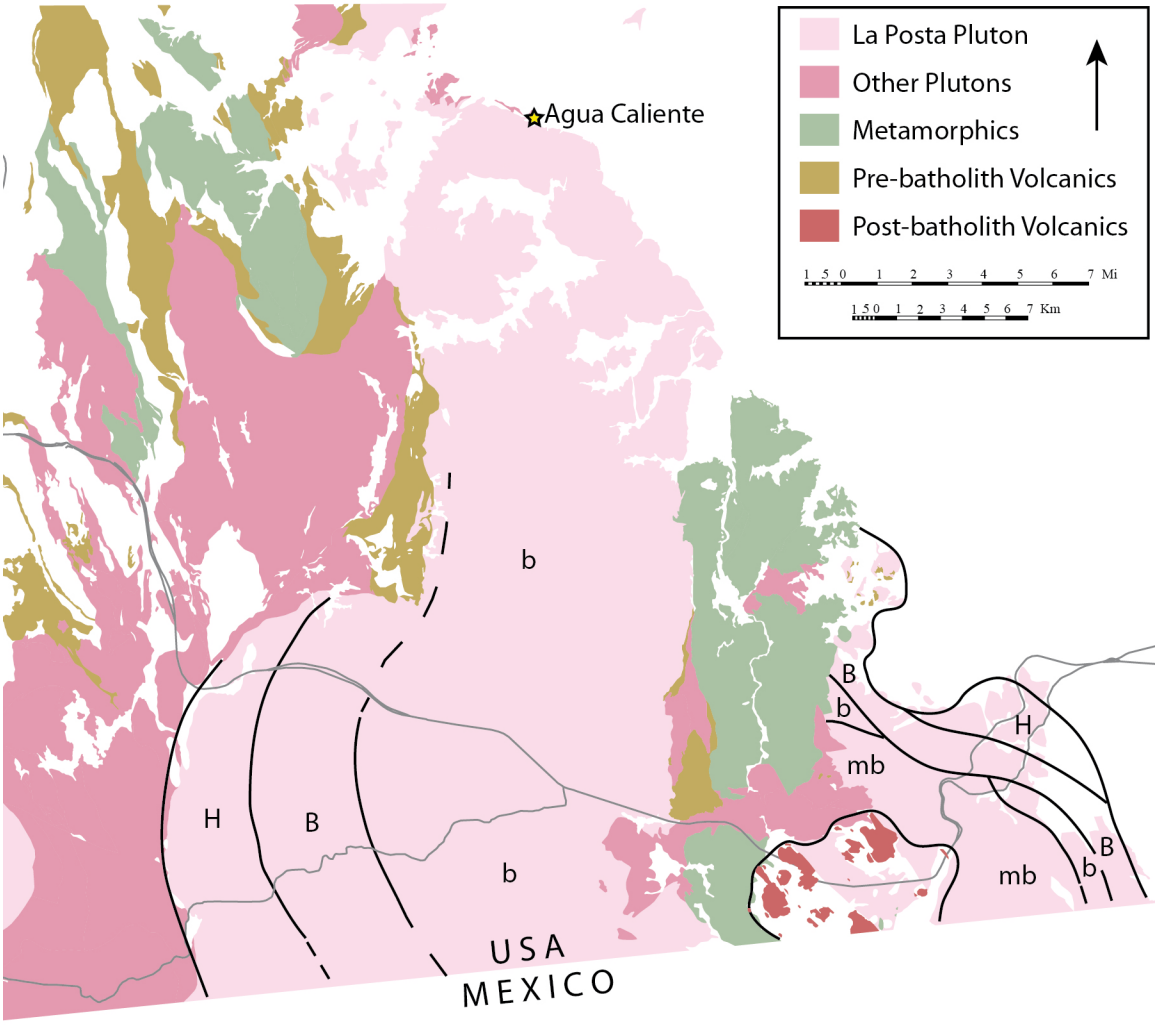

FIGURE 4 The La Posta pluton is concentrically zoned with five major facies. Inward, the facies are the border facies, hornblende-biotite facies (H), large biotite facies, (B), small biotite facies (b), and muscovite-biotite facies (mb) described in Table 2. Rocks on the western side of the pluton are other plutons in the Peninsular Ranges batholith. On the east are younger sedimentary rocks. The Triassic metamorphic Julian Schist is dispersed within the pluton. Figure is modified from Clinkenbeard and Walawender, 1989 and Todd, 2004.

faces. Metasedimentary rocks compose the northernmost section of the range, and previous mappers proposed there is a leucotonalite border zone where the pluton meets the metasedimentary rocks (Todd, 1977). On the northern and eastern sections of the range, the detachment fault footwall comprises the prebatholithic metasedimentary units and the

Table 2 Mineralogic facies within the La Posta pluton.

Facies (rim to center)	Composition
Border Facies	The border facies is present as a narrow band (<100 m wide) where the La Posta pluton intruded older igneous rocks on the western side of the pluton and not present where the pluton intruded into metasedimentary or metaigneous rocks (Clinkenbeard,1987; Clinkenbeard and Walawender, 1989). On the east, the hornblende-biotite or large-biotite facies are the edge of the pluton (Clinkenbeard and Walawender, 1989). The outermost 50 meters of the border facies has bands of subhedral to euhedral crystals of plagioclase and quartz alternating with hornblende and biotite, and inward from the banding, the rock is weakly foliated (Clinkenbeard and Walawender, 1989). Sphene, muscovite, and tourmaline are accessory minerals (Clinkenbeard, 1987).
Hornblende-Biotite Facies	The hornblende-biotite facies is a tonalite composed of <0.5 cm sphene crystals, large (<1 cm) euhedral, inclusion-free hornblende, pseudohexagonal biotite booklets, abundant and zoned euhedral plagioclase (<1 cm), anhedral quartz grains (Walawender et al., 1990) with weak undulatory extinction and sutured boundaries, and occasional interstitial alkali feldspars with "gridiron" twinning (Clinkenbeard and Walawender, 1989). The facies is the primary unit on the margins of the La Posta pluton (Clinkenbeard and Walawender, 1989).
Large Biotite Facies	The large biotite facies is composed of large (<1 cm) pseudohexagonal biotite booklets; Hornblende exhibits a gradual loss of euhedral, large crystals from the hornblende-biotite facies, to small (0.1-0.3 cm) subhedral hornblende crystals, which continue to decrease in abundance moving toward the inward parts of the pluton and into the small biotite facies (Clinkenbeard and Walawender, 1989). Alkali feldspar increases in abundance and forms oikocrysts <3 cm enfolding the other minerals within the rock (Clinkenbeard and Walawender, 1989; Walawender et al., 1990). Plagioclase crystals are subhedral and zoned, and quartz is coarser than but similar to the quartz in the hornblende-biotite facies (Clinkenbeard and Walawender, 1989).
Small Biotite Facies	The small biotite facies contains small (0.1-0.4 cm) euhedral to subhedral biotite crystals, few hornblende, which, if present, are within biotite or plagioclase crystals, subhedral faintly zoned plagioclase (0.1-0.3 cm) crystals, quartz with strong undulatory extinction, and alkali feldspar oikocrysts with well developed "gridiron" twinning (Clinkenbeard and Walawender, 1989) which reach <5 cm long (Walawender et al., 1990).
Muscovite-Biotite Facies	The innermost facies of the La Posta pluton is the muscovite-biotite facies composing the muscovite-biotite granodiorite rock type (Clinkenbeard and Walawender, 1989). This facies is like the small-biotite facies with the addition of 0.1-0.3 cm subhedral muscovite sheets and the lack of sphene crystals (Clinkenbeard and Walawender, 1989). Muscovite crystals are visible in hand sample and make up ~1% of rock (Walawender et al., 1990) and are thought to be primary minerals with the exception of trace amounts of sericite within plagioclase crystals (Clinkenbeard and Walawender, 1989).

La Posta tonalite while the Canebrake Conglomerate, Palm Springs Formation, and the tonalite compose the hanging wall in the Tierra Blanca Mountains (Todd, 1977).

The intersecting West Salton detachment and Elsinore faults produce a large damage zone correlative with emerging subterranean fluids. Subsidiary faults within the Tierra Blanca Mountains strike northeast (Todd, 1977; Jennings and Bryant, 2010) and are usually identified in the field by the presence of red and orange alteration zones.

The Tierra Blanca Mountains are extremely arid, and any precipitation or runoff infiltrating the soils becomes a part of either the Canebrake Valley or the Vallecito-Carrizo groundwater basins, sub-basins in the Colorado River Groundwater Basin (Figure 6; California Department of Water Resources, 2003), and these basins may be recharging the fluids emerging at the base of the mountains. Annual precipitation in the Vallecito-Carrizo Valley groundwater basin is 2.5-35.5 cm/yr, and the Canebrake Valley groundwater basin receives 25-40 cm/yr (California Department of Water Resources, 2003). As the mountains are composed of low-permeability tonalite, the runoff accumulates in Quaternary alluvium and underlying Tertiary alluvial deposits in the adjacent valleys. High amounts of evapotranspiration during the hot desert summers limit total infiltration, and

Figure 5 (Following page) A—View looking southeast across Agua Caliente County Park at the Cretaceous tonalite pluton (Kt), the heavily fractured protolith, the bleached protolith, and the stained bleached protolith. There are several spring boxes at the park, but the one labeled is the location for water sampling. The West Salton detachment fault wraps around the mountain front and turns southward down Moonlight Canyon. An oblique-right-lateral strike-slip fault strikes southeast and extends from the county park paralleling the mountain front. B—View of the alteration, West Salton detachment fault, and the heavily fractured protolith and protolith (Kt) in the footwall of the detachment fault directly west of the county park. The contact between the bleached and stained protolith and the detachment fault is sharp. The fault strikes northwest-southeast along this section of the mountain front.

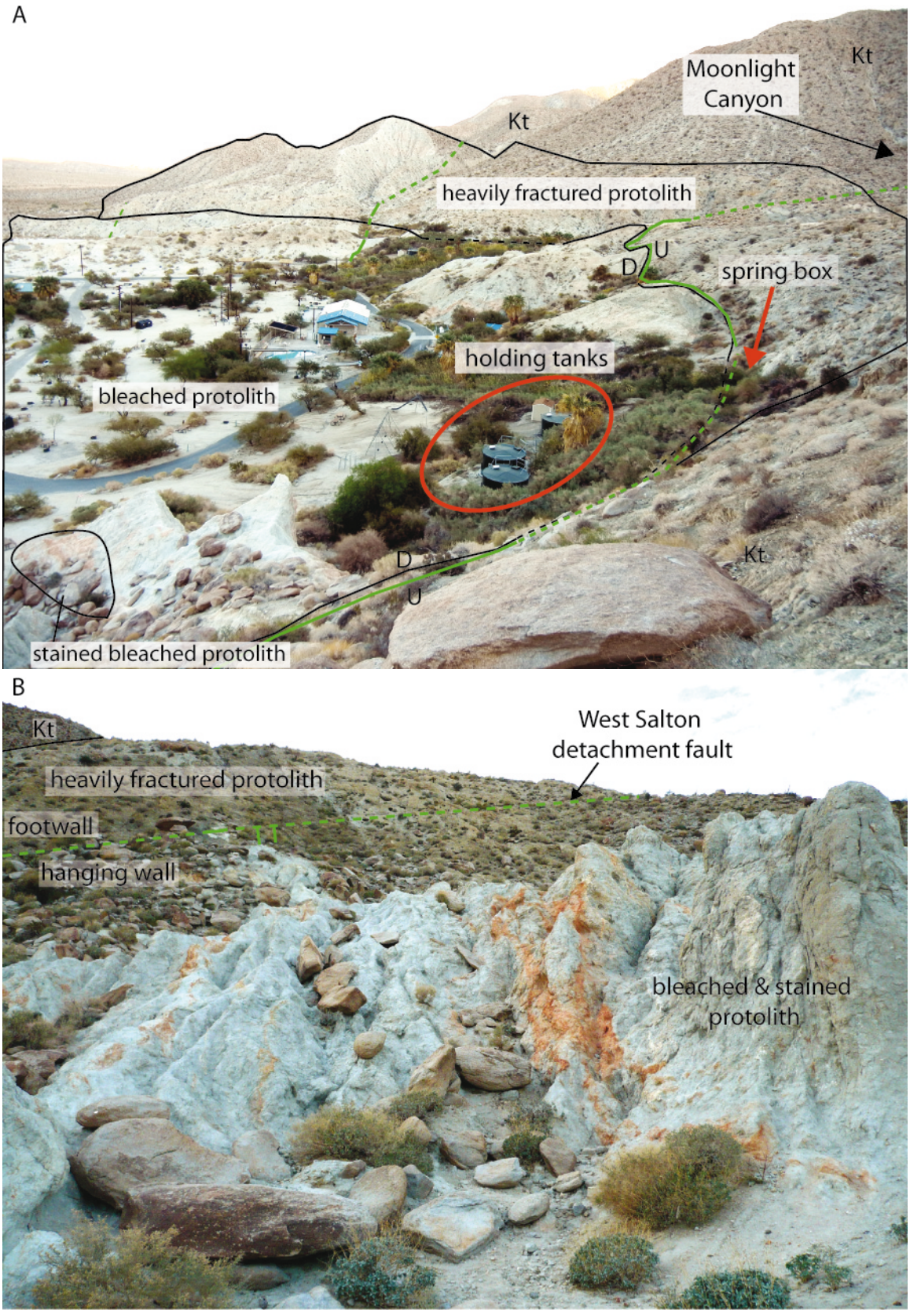
A
Moonlight Canyon
Kt
Kt
heavily fractured protolith
D
U
spring box
holding tanks
bleached protolith
D
U
Kt
stained bleached protolith
B
Kt
West Salton detachment fault
heavily fractured protolith
footwall
hanging wall
bleached & stained protolith

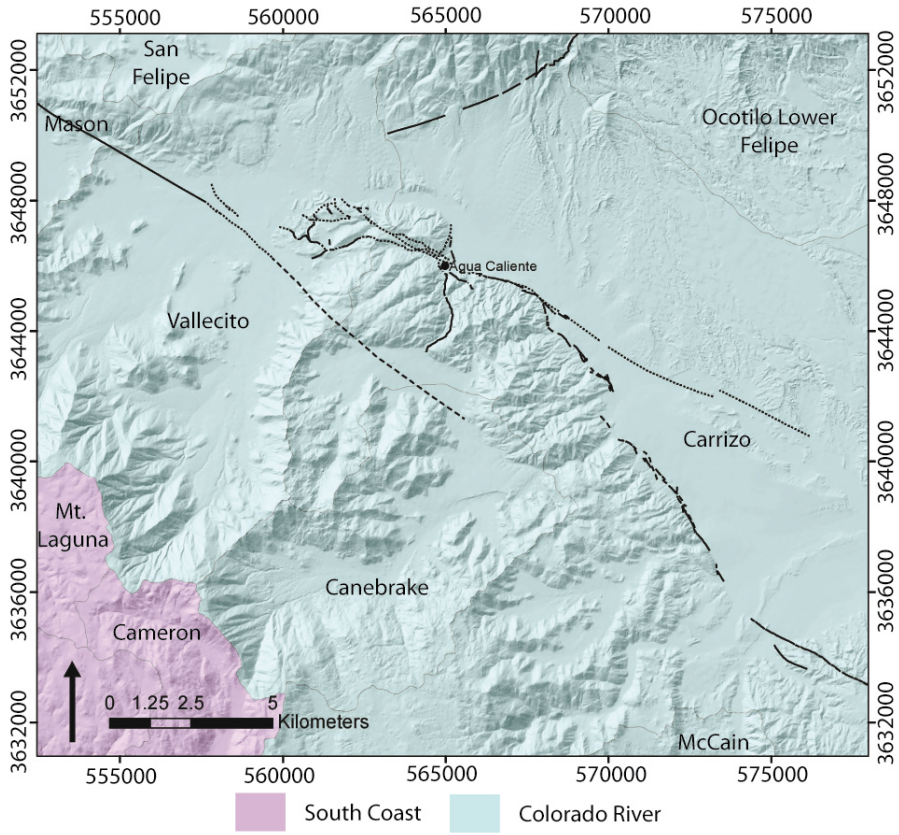

FIGURE 6 Two groundwater basins cover the Tierra Blanca Mountains: the Vallecito Groundwater Basin and the Carrizo Groundwater Basin. Both basins are part of the larger Colorado River Groundwater Basin.

this signature may be seen with lengthy seasonal logging of wells and springs.

Agua Caliente County Park is a small park located at the base of the Tierra Blanca Mountains that takes advantage of several closely-spaced springs emerging from the intensely fractured and altered La Posta tonalite pluton to supply recreational pools (Figure 7). Prior to refilling the pools, the spring fluids accumulate in spring boxes and are transported to and chlorinated in holding tanks (Figure 5). Agua Caliente County Park is the locus of intense alteration and damage as a result of complex faulting and fluid flow, and the geometry of the faults control where the fluids can easily migrate (Sibson, 1987).

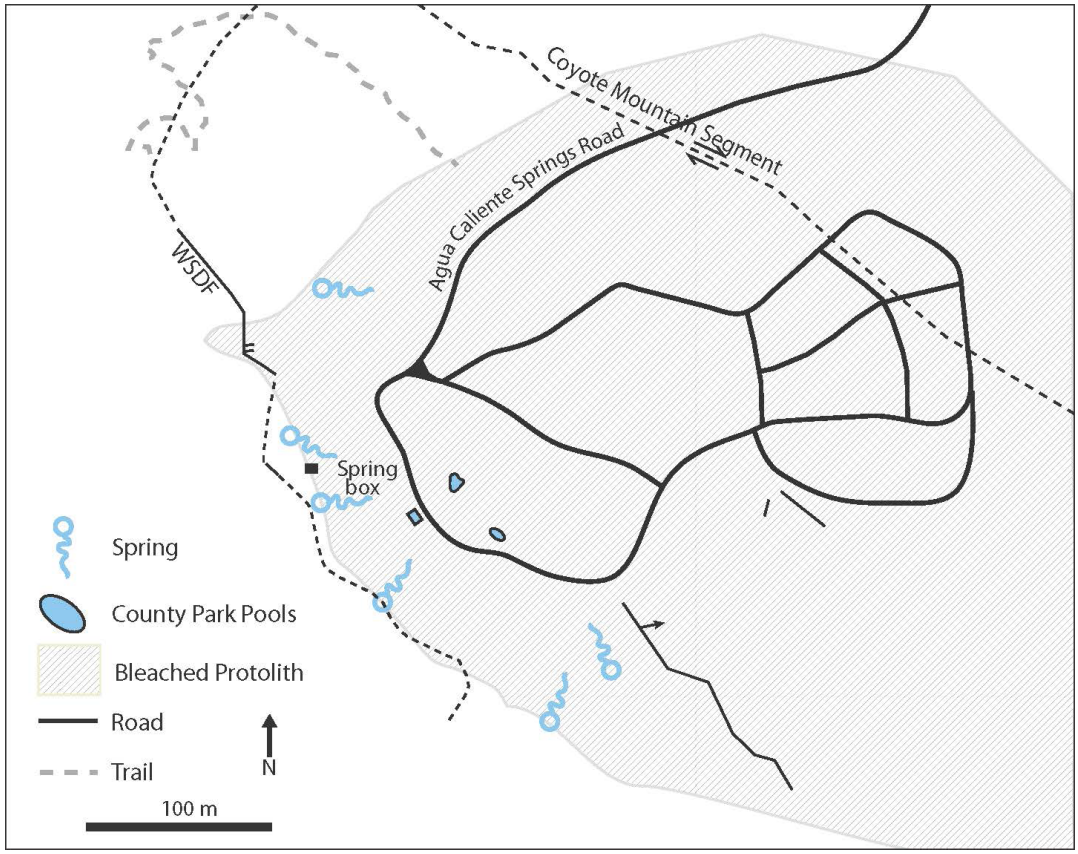

FIGURE 7 Agua Caliente County Park hosts commercially-developed warm springs derived from the natural warm springs effusing from the Coyote Mountain segment damage zone and within the hanging wall of the West Salton detachment fault. The Coyote Mountain segment is ~ 300 m to the east of the springs and the detachment fault trace along the mountain front.

DATA COLLECTION METHODS

Structural Analysis

Structural analysis included assembling available previous mapping interpretations of the field area, mapping the county park and the eastern mountain front arroyos, mapping faults in the Tierra Blanca Mountains with aerial imagery and fieldwork, determining fracture character at three scanlines, and plotting all data by location on stereonets. Agua Caliente County Park is easily accessed by the Great Southern Overland Stage Route of 1849 County Highway S-2. Access to the interior of the Tierra Blanca Mountains was possible by foot through arroyos trending roughly east-west and also from the north, south of the Vallecito Stage Station County Park in Vallecito Valley.

I mapped the fault traces and damage zones within the study area at 1:12,000 using the Agua Caliente Digital Orthophoto Quarter Quad (DOQQ) overlain with the Agua Caliente Digital Raster Graphic (DRG) 7.5' USGS topographic map. Landsat 7 images and Google Earth imagery were useful in locating fault traces and identifying lithologic variations. Landsat 7 images were downloaded from USGS Global Visualization Viewer and loaded into Adobe Photoshop with three bands per image. Each band was assigned to an R, G, or B to make an RGB image. Once the images were layered on top of one another, I adjusted the RGB levels or changed the Mode to Lab Color or CMYK from RGB. By adjusting the colors of the image to focus on certain wavelengths in both the visible spectrum and infrared, certain lithology variations became clear. The image in Figure 3 contains Landsat 7 Bands 752 with Band 8 overlain. The new image was created by combining bands 7, 5, and 2 in RGB, respectively, and then changing the mode to Lab Color

and overlying band 8 as the lightness channel. By using this new image, I was able to discern apparent compositional variations in the La Posta pluton and see lithology changes in the basins (Figure 3). The datum used for this mapping project is UTM NAD 1983 Zone 11 and all UTM locations are given in this system. To create shaded topographic relief on images, the hillshades were made using a z-factor 0.00001036 m provided by ESRI (http://blogs.esri.com).

The mesoscale analysis of the field area comprised measuring the orientations of small faults and fractures along the mountain fronts and in the arroyos where faults were previously mapped (Appendix A). I interpreted damage zones as areas that are heavily fractured, have reduced biotite grain sizes, and the protolith is friable and powdery. Subsidiary faults are often concealed by washes or inferred based on topography, but I identified faults by associated fault-related rocks including chlorite covered faces, slickenlines, and red-orange alteration. Initially, I sketched faults on available Google Earth and checked accessible locations in the field. Orientations of faults and fractures are plotted on the map with strike and dip symbols and stereonets. I designated three areas in the Tierra Blanca Mountains to measure fault and fracture orientations along three scanlines. In addition to personal mapping, I used mapping from Todd (1977) and Dorsey et al. (2012) to complete a compilation.

We collected 109 rock samples from the Tierra Blanca Mountains. Samples included fault cores, fractured damage zone, altered protolith, and not-visibly altered protolith. Forty-one of the samples were collected in a line west of the county park (Figure 8). These samples were ~ 10 m apart except the last few samples were farther apart on account of covered bedrock. Sample orientations, where available, were recorded in

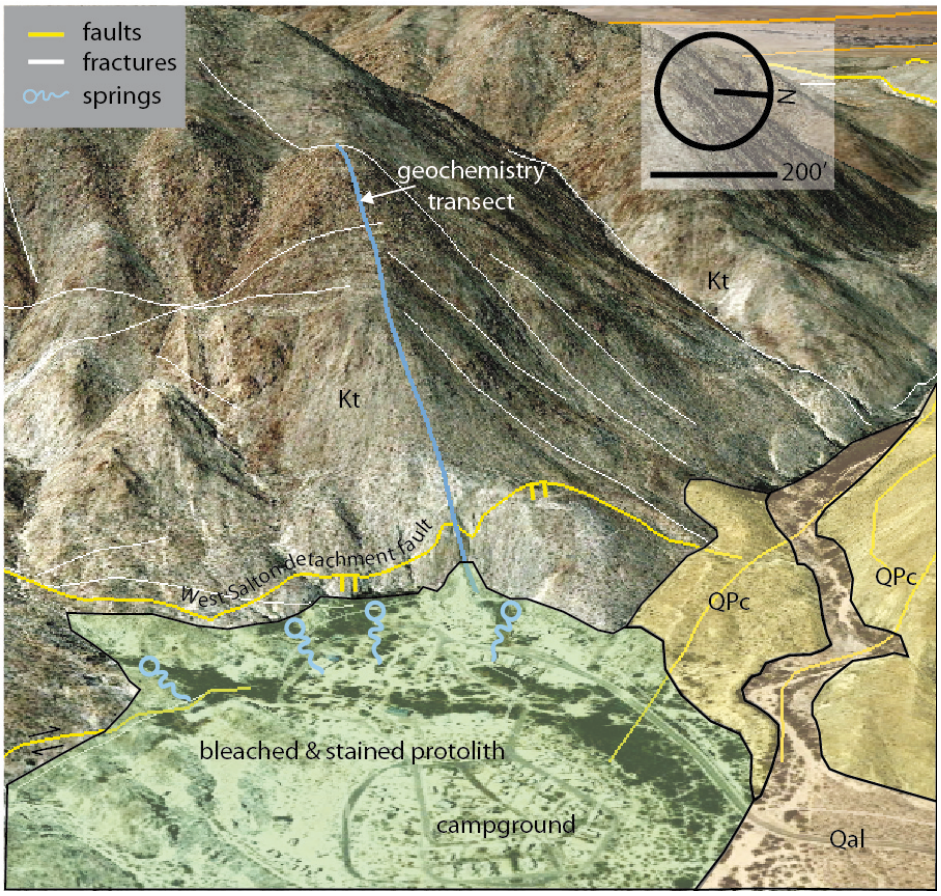

FIGURE 8 The oblique Google Earth view to the rest of the study area shows the geochemistry sampling transect (blue) ~ 640 meters long that strikes approximately east-west and crosses the bleached altered tonalite, a range-front fault associated with the detachment fault system directly west of the county park, and intact plutonic rock. Forty-one samples were collected along this transect, twenty-six of which were analyzed via x-ray diffraction. The bleached and stained protolith (green) is on the hanging wall of the West Salton detachment fault and the contact between the alteration and the detachment fault is sharp whereas there is no abrupt change associated with the strike-slip faults in the area. The Palm Spring and Canebrake Formations (tan, QPc) overlie the plutonic rock (Kt) in the northern section of the park. Quaternary alluvium (peach, Qal) fills an arroyo cutting through the tonalite and the Palm Spring and Canebrake Formations. The mountain front dips ~ 54° which corresponds to the dip of the detachment fault on some planes near the mountain base. The tonalite in the mountains grades from tan-pink to red and brown away from the valley floor. The tonalite weathers into very large boulders (a meter to ~ 6 meters in diameter) around the color change.

a field notebook. This spacing was chosen because it should show the changes on a field scale. Samples collected along this transect create a geochemical gradient roughly perpendicular to the West Salton detachment fault trace mapped by Dorsey et al. (2012; and references therein) seen in outcrop at 564845 m E, 3645905 m N, and field measurements show a strike of 164° and dip of 40° NE.

Thirty-eight samples were made into thin sections at Burnham Petrographics in Rathdrum, Idaho (http://www.burnhampetrographics.com/index.php). The samples selected for thin sections were from the geochemistry transect west of the county park, from faults in Moonlight Canyon, and from the damaged zone southeast of the county park along the edge of the Tierra Blanca Mountains. Forty-two samples were used in x-ray diffraction analyses. The samples were chosen based on their location and the alteration perceived in hand sample. Twenty-six of these samples were part of the aforementioned transect. Samples for x-ray diffraction were crushed using a ROCKLABS Standard Ring Mill Batch pulveriser for 3.5-4 minutes. After crushing the sample, I preserved the flour in a labeled glass vial until later use.

After running the sample through the Philips X-Pert PRO PANalytical machine, I used the X-Pert Highscore software package to select, analyze, and identify peaks. The samples were scanned from 2-75° in a 60 minute scan. The method for assigning minerals was based from thin section analysis and knowledge of the literature for the Peninsular Ranges batholith and granitic alteration. The mineral database for X-Pert Highscore is very specific, and though I satisfied all of the peaks proposed by the program with my best interpretation, the minerals that matched the peaks may not be the exact composition. After selecting the highest scoring candidates (50 or higher), I selected those probable

candidates working toward lower scores until the peaks were satisfied. X-ray diffraction analysis generated possible compositions of the unaltered and altered protolith mineralogy, showed fault core and damage zone compositions, and revealed an alteration gradient. The analyses were compared with collected water chemistry data to propose reactions occurring as a result of the traveling fluids and also to see the extent of fluid penetration away from the faults.

Water Sampling & Analysis

Rangers at Agua Caliente County Park permitted our access to a spring box located on the western edge of the camping area (Figure 5; 564910 m E 3645838 m N). We sampled and analyzed the spring from February 3-10, June 9-August 22, and on November 5, 2011 (Table 3). Water samples were analyzed for elemental concentrations, pH, stable isotopes, an on-site alkalinity titration. We logged temperature, conductivity, and water level using a Solinst LTC Levelogger Junior and air temperature and pressure using a Solinst Barologger. The park had a dated report of spring chemistry posted on the indoor pool building (Table 4).

Samples for elemental analyses were collected by filtering the water through a 0.45 micrometer nylon membrane filter with a 50 mL syringe and stored in a 50 mL polycarbonate centrifuge tube to ensure there was enough fluid for accurate analysis. The sample for cations required preservation by adding concentrated 2.5 mL nitric and 2.5 mL hydrochloric trace metal grade acid. The anion sample did not require preservation with acid. The Utah State University Analytical Laboratories (USUAL) analyzed our cation and anion samples (Table 5).

We collected two samples for δD and $\delta^{18}O$ analysis by the Stable Isotope Ratio Facility for Environmental Research (SIRFER) lab at the University of Utah. The lab reports that samples are run with reference samples calibrated against the NIST and/or IAEA standards. $\delta^{18}O$ has a precision of ± 0.2 ‰ (SMOW), and the precision for δD is ± 2 ‰. A third sample was sent to Geochron Laboratories in Chelmsford, MA where it was processed for $\delta^{13}C$. Samples for stable isotopes were sealed in an airtight vial after filtration to ensure no gases enter or exit before analysis. The $\delta^{13}C$ value of the dissolved inorganic carbon in spring water was computed as follows:

$$\delta^{13}C_{sample}‰ = \left[\frac{^{13}C/^{12}C_{sample}}{^{13}C/^{12}C_{standard}} - 1\right] \times 1000 \qquad \text{Equation 1}$$

where the $^{13}C/^{12}C_{standard}$ is the Peedee belemnite (PDB) with a value of 0.011237 (Coplen, 1994; Geochron Laboratories report). In February 2011, we determined pH using a colorpHast pH-indicator strip, and we re-measured in November 2011 using an Omega PHH-5012. We measured the spring temperature using the Digi-Sense Thermometer Type K Thermocouple Probe and performed an alkalinity titration in the field during November 2011 using a HACH Alkalinity Test Kit, Model AL-AP MG/L.

Table 3 A summary of water data collected during 2011.

	Feb 2011	Jun-Aug 2011	Nov 2011
Elemental	X		X
pH	X		X
Temperature	X		X
Stable Isotopes			X
Alkalinity			X
LTC Logging	X	X	
Barometric Logging		X	

A Solinst LTC Levelogger Junior calibrated with a 1413 µS Oakton conductivity solution was suspended in a park spring box and recorded conductivity, water level, and temperature of the springs every 15 minutes from June 9 to August 22, 2011 (Figure 9). Conductivity for February 2011 was measured without calibration so the specific values may be incorrect while the amounts of change are real. To obtain accurate water level values, we used the Solinst Barologger to determine the local barometric pressure and converted it to its water column equivalent. The equation for the conversion is

$$30.0551 \text{ in} \times 1.1330 = 34.0524 - 31.17 = 2.88 \text{ ft} \qquad \text{Equation 2}$$

where 30.0551 is the barometric pressure in inches, 1.1330 is a pressure conversion factor, and 31.17 (or 9.50 m) is an equation standard so water levels in the spring were lowered by 2.88 ft (0.877 m; Manual Barometric Compensation from Solinst, 2012). We examined the data using Levelogger 4.0.1 provided by Solinst.

Earthquake magnitudes and locations were collected from the Southern California Earthquake Center online database compiled by Hauksson et al. (2011) and are accessible at http://www.data.scec.org. The information is available for download in table format which then can be inputted in ArcGIS along with a Quaternary faults layer.

Table 4 A summary of water data collected during 2011.

	Feb 2011	Jun-Aug 2011	Nov 2011
Cations & Anions	X		X
pH	X		X
Temperature	X		X
Stable Isotopes			X
Alkalinity			X
LTC Logging	X	X	
Barometric Logging		X	

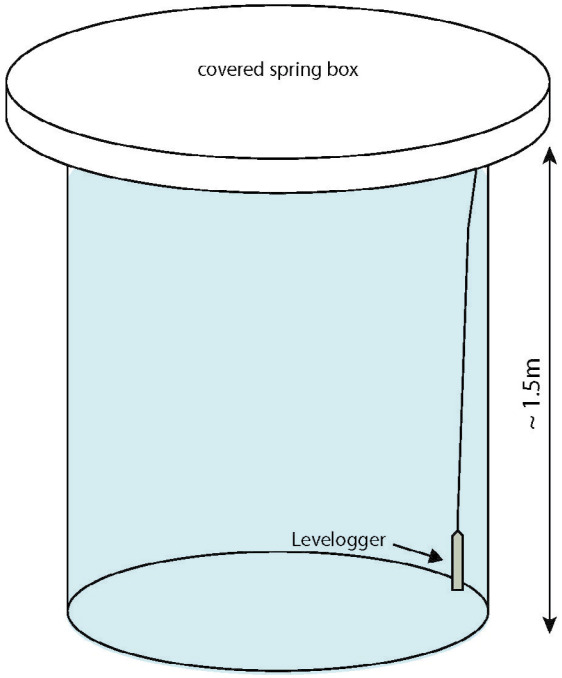

FIGURE 9 A schematic of the spring box in which we placed the Solinst LTC Levelogger Junior. The container is a cylinder buried into the ground with an opening at its base allowing spring fluids to enter and flow to holding and chlorination tanks (Figure 5). The cylinder is covered with a plastic lid and bolted down to prevent park visitors to contaminate the water.

We calculated geothermometry values for the spring based on cation data (Table 5). The Na-K-Ca geothermometer (Karingithi, 2009) is the most applicable geothermometer for our data because the springs are slightly thermal, may not be fully equilibrated with the host rock, and the springs have high silica concentrations (28.8-39.0 mg/L; Table 5). We checked the NaK and NaKCaMg geothermometers, but they were not valid. Because log√Ca/Na was positive, β = 4/3. The cation values were converted from mg/L to molality (mol/kg) in order to calculate correct temperature values (Table 6). The Na-K-Ca geothermometer equation we used from Karingithi (2009) is

$$\theta(°C) = \frac{1647}{\log {}^{Na}/_{K} + \beta \log\left({}^{\sqrt{Ca}}/_{Na}\right) + 2.24} - 273.15$$

$$if\ \log\frac{\sqrt{Ca}}{Na} > 0, \beta = \frac{4}{3}$$

$$if\ \log\frac{\sqrt{Ca}}{Na} < 0, \beta = \frac{1}{3}$$

Equation 3

where θ is the temperature at which the mineral and water phases were last in equilibrium. The values for sodium (Na), potassium (K), and calcium (Ca) are in moles per kilo-

Table 5 Water elemental analysis concentrations in mg/L processed by the Utah State University Analytical Laboratory

Element	Sample 1-2	Sample 2-2	Sample 1-11	Sample 2-11	Detection Limits
(mg/L)					
Cl	68.1	not tested	70.7	not tested	
Al	<0.12	<0.12	<0.12	<0.12	0.12
As	<0.01	<0.01	<0.01	<0.01	0.01
B	0.77	0.66	0.80	0.70	0.02
Ba	<0.001	0.006	<0.001	<0.001	0.001
Ca	1.86	2.35	1.86	2.14	0.08
Cd	<0.001	<0.001	<0.001	<0.001	0.001
Co	<0.005	<0.005	<0.005	<0.005	0.005
Cr	<0.006	<0.006	<0.006	<0.006	0.006
Cu	<0.008	<0.008	<0.008	<0.008	0.008
Fe	<0.003	0.004	<0.003	0.01	0.003
K	1.38	1.18	1.49	1.25	0.46
Mg	0.02	0.06	0.01	0.02	0.007
Mn	<0.001	<0.001	<0.001	0.003	0.001
Mo	<0.15	<0.15	<0.15	<0.15	0.15
Na	96	79.8	102	85.7	0.08
Ni	<0.003	<0.003	<0.003	<0.003	0.003
P	<0.008	<0.008	0.11	<0.008	0.08
Pb	<0.003	<0.003	<0.003	<0.003	0.03
S	19.4	16.1	31.1	16.5	0.07
Se	<0.04	<0.04	<0.04	<0.04	0.04
Si	35.1	28.8	39.0	32.3	0.15
Sr	0.04	0.05	0.04	0.05	0.03
Zn	<0.005	<0.005	<0.005	<0.005	0.005

gram. Water chemistry and seismic events within 10 km of the spring box were compared to determine if there are any relationships between spring behavior and seismicity. Additionally, hypocenter locations can reveal fault geometries.

Table 6 Elemental concentrations in weight per volume and molality

Sample	Na^+ (mg/L)	K^+ (mg/L)	Ca^{2+} (mg/L)	Na^+ (mol/kg)	K^+ (mol/kg)	Ca^{2+} (mol/kg)	θ (°C)
1-2	96	1.38	1.86	0.00418	0.0000353	0.0000464	84.9
2-2	102	1.18	2.35	0.00444	0.0000302	0.0000586	75.4
1-11	79.8	1.49	1.86	0.00347	0.0000381	0.0000464	85.6
2-11	85.7	1.25	2.14	0.00373	0.0000320	0.0000534	77.6

RESULTS

I present results of structurally mapping of the field area on the macro-, meso-, and micro-scales. I then present results of the fluid chemistry data from the springs supplying the recreational pools at Agua Caliente County Park, followed by X-ray diffraction data that characterizes the mineralogy of the host rocks, fault zones, and altered zones, thin section analyses, and the distribution of protolith alteration. Analyses of the location of local seismic events during data collection are also presented.

Macroscale Observations

The transition from the northwestern double-stranded portion to the southeastern single-stranded portion of the Elsinore fault appears to be marked by the presence of cross faults roughly perpendicular to the dominant strike of the major fault system (Plate 1). The cross faults are visible in aerial imagery throughout the Vallecito and the Tierra Blanca Mountains (Plate 1; Figure 3). The cross faults strike N48°E to N53°E within the Tierra Blanca Mountains and form approximately eleven large northeast-trending valleys up to 3 km long and cut the plutonic rock (Figure 10).

In the Tierra Blanca Mountains, the West Salton detachment fault is cut at multiple locations by strike slip faults associated with the Elsinore fault system (Plate 1; Figure 3; Axen, unpublished mapping). The fault trace extends for ~ 2.2 km from 561594 m E 3647949 m N to 561315 m E 3646464 m N and wraps around in the northwestern-most extent of the mountains, dividing the prebatholithic metamorphic rocks from Palm Spring and Canebrake Formations and the La Posta tonalite (Figure 11). The detachment is split between two offset traces along Marsh Canyon; the northern trace is ~ 1.35 km

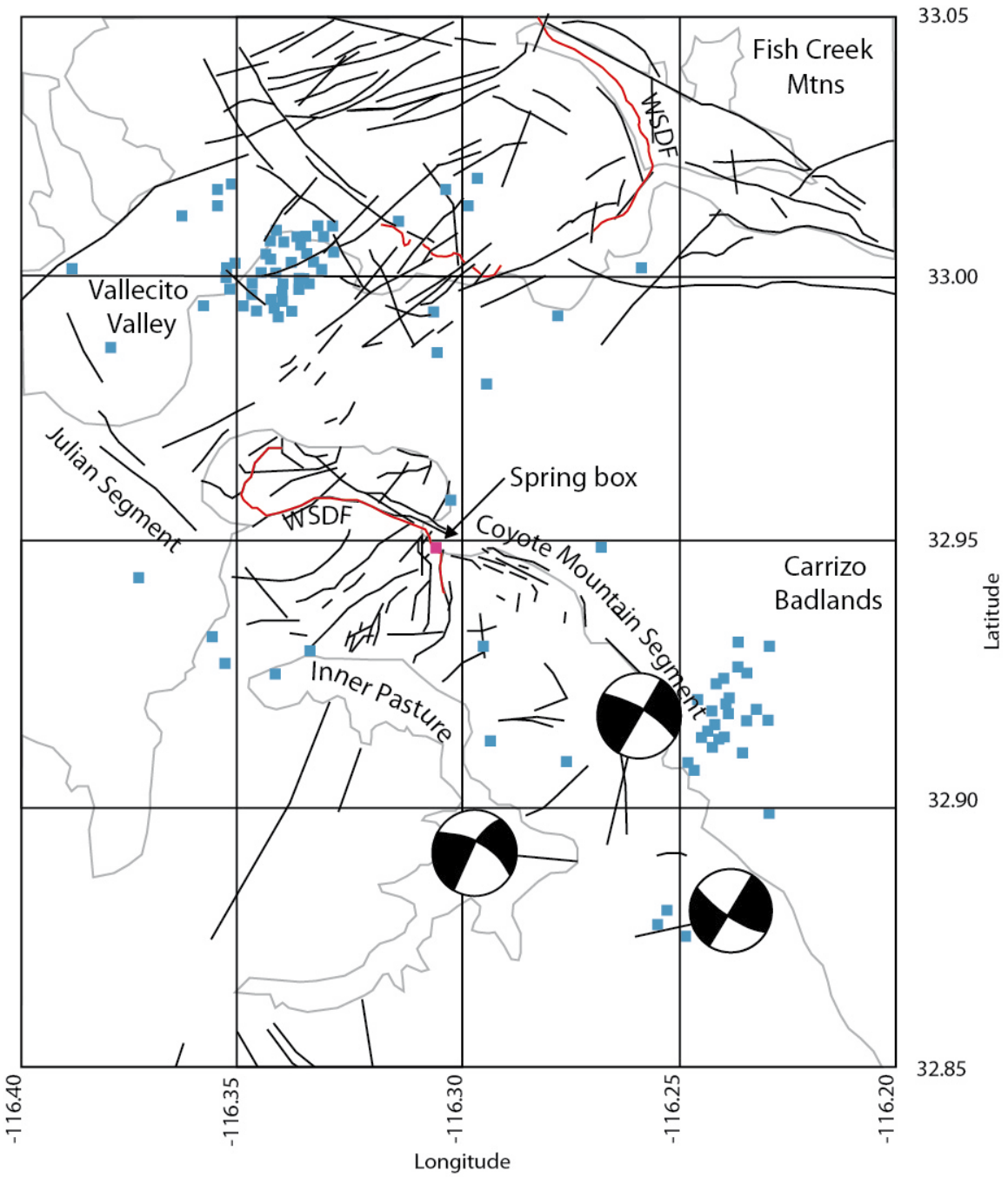

FIGURE 10 Focal mechanisms reported by Allison et al. (1978). Though the Julian segment is concealed through Inner Pasture and in the Tierra Blanca Mountains, slip from the September 13, 1973 M 4.8 earthquake and aftershocks revealed right lateral displacement.

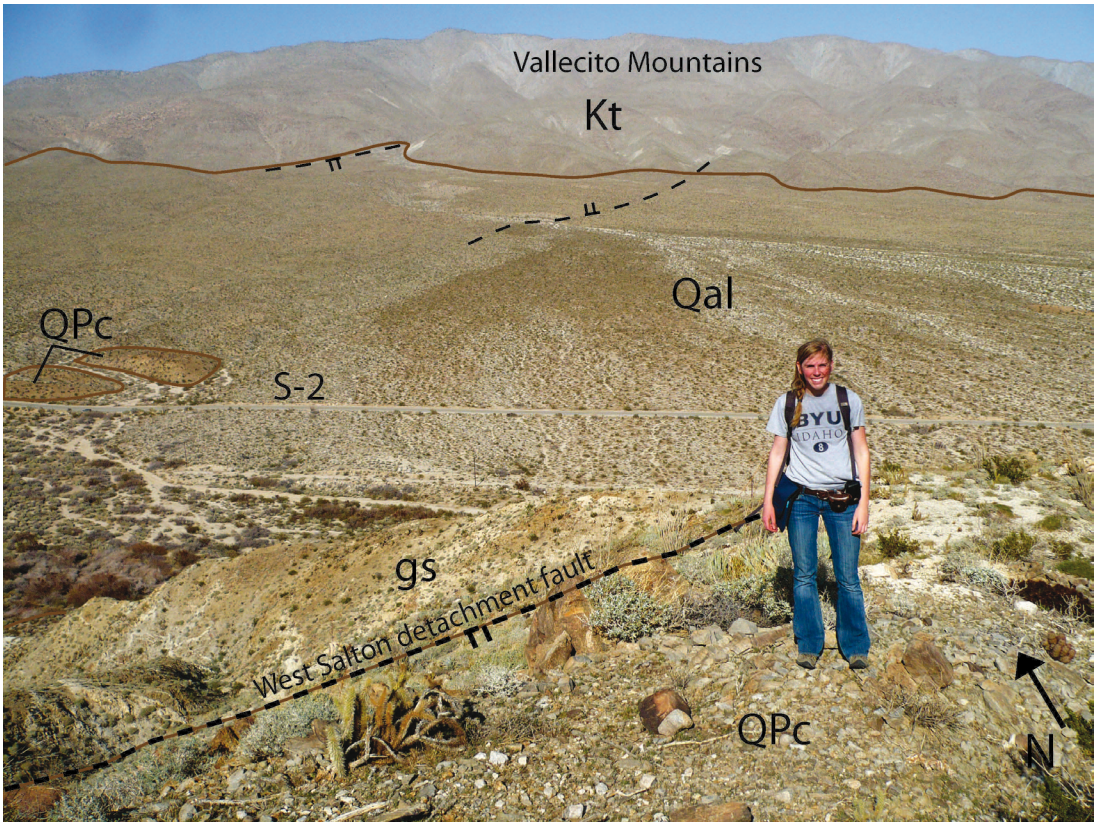

Figure 11 The top-to-the-east West Salton detachment fault separates the Canebrake Conglomerate and Palm Springs Formation (QPc) from the prebatholithic metamorphic rocks (gs) in the northwestern-most section of the Tierra Blanca Mountains. Quaternary alluvium (Qal) fills the Vallecito Valley to the north and lap onto the Vallecito Mountains composed of the Cretaceous La Posta pluton (Kt). The metamorphic rocks are mostly folded micaceous schist and quartzite.

and the southern is ~ 1.7 km long. The detachment fault trace on the western side of the county park and along Moonlight Canyon is ~ 3.25 km long and exhibits top-the-east-slip based on the presence of Quaternary sediments in the hanging wall east of the Triassic metasedimentary footwall in the northwestern portion of the mountains (Figure 11) and east-dipping field measurements of the fault surface. The La Posta tonalite and Canebrake Formation conceal the fault traces north of the county park. The detachment fault wraps around into Moonlight Canyon and disappears upon reaching Inner Pasture (Figure 3).

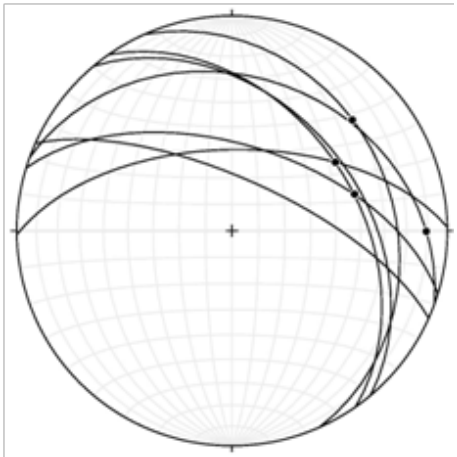

Figure 12 Faults and slip indicators (trending 19-90°) associated with the Coyote Mountain segment damage zone.

Dip angles vary along the detachment fault. For example, along the mountain front by the county park the dip varies from 29°-70° within ~ 100 m, a result most likely from later slip on Elsinore-related faults or the fault may be corrugated.

Variations in lithology cause color changes in a treated Landsat image of the study region (Figure 3). The Cretaceous La Posta tonalitic pluton is pink, purple, and blue, and the prebatholithic metamorphic rocks in the northwestern corner of the Tierra Blanca Mountains are expressed as green, yellow, purple, and light pink (Figure 3). The lithologies for the Canebrake Conglomerate and Palm Spring Formation are conglomerates and gray sandstones that appear as red, brown, green, and purple (Figure 3). Quaternary alluvium filling the valleys is peach, yellow, and light green (Figure 3). The sedimentary units in Carrizo Valley have variable colors. The bleaching and staining at Agua Caliente County Park (Figure 8) is also distinguishable on aerial imagery and appears white to light pink with a gradual contact between the bleached and unaltered rocks (Figure 3). The image does not have sufficient resolution to display the stained outcrops.

The Coyote Mountain segment of the Elsinore fault, located on the northeastern flank of the Tierra Blanca Mountains southeast of Agua Caliente County Park, also referred to as the Tierra Blanca fault (Kairouz, 2005), exhibits oblique-dextral slip along the eastern mountain front with slip indicators ranging from 19-90° along faults paralleling the Coyote Mountain segment (Figure 12). Several faults that are parallel to the mountain

front dip approximately 65-70° toward the main trace although some faults dip steeply into the mountain like the fault found at Coyote Canyon which dips 80° southwest.

In aerial imagery, several subsidiary faults paralleling the mountain front south of the county park are present over ~ 450 m into the mountains to the west (Plate 1). Northwest of the Tierra Blanca Mountains in Vallecito Valley (S.8, 9, 15, and 16 T.14 S., R.6 E.), the Julian segment, identified by ~ 2.72 km of aligned vegetation, exhibits a minor subsidiary fault ~ 1.29 km long and ~ 0.30 km northeast of the former segment (Fig 3).

The surface trace of the Coyote Mountain segment of the Elsinore fault trace in the northernmost section of the Tierra Blanca Mountains, north of the county park, is continuous and has a well developed scarp along its trace but becomes increasingly complex to the southeast where it is parallel to County Highway S-2 and the Tierra Blanca Mountains flank (Plate 1). The complexity of the Coyote Mountain segment arises with numerous steeply dipping subsidiary faults visible along the mountain front while the main fault is buried beneath Quaternary alluvium (Figure 13; Plate 1).

Mesoscale Observations

Mapped units in the study area include the Cretaceous La Posta tonalite, the Pliocene-Pleistocene Canebrake conglomerate and Palm Spring Formation, Quaternary alluvium, metamorphic gneiss and schist, and unnamed altered rocks along the faults and within the Tierra Blanca Mountain range.

The Cretaceous La Post tonalite (Kt) is a white tonalite composed of euhedral and subhedral quartz, plagioclase, and biotite booklets. A few scattered pegmatites are scattered throughout the mountains. The plutonic unit is the predominant lithology in the

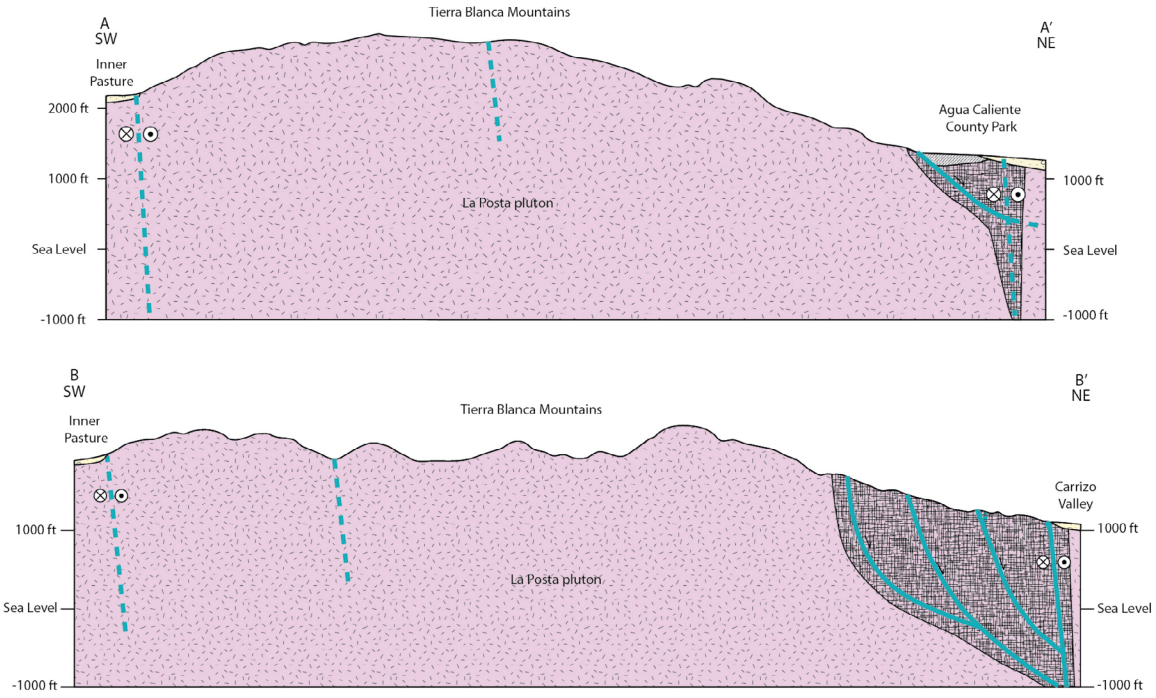

Figure 13 Cross sections across the Tierra Blanca Mountains. A-A' is a SW-NE cross section from Inner Pasture to Agua Caliente County Park. The mountains are composed of the La Posta tonalitic pluton. On the northeastern side the Coyote Mountain segment of the Elsinore fault strikes parallel with the mountain range and the faults moving inward may form a tulip structure along the concealed main trace. Lithologies at the surface are Quaternary alluvium and the bleached protolith which forms a sharp contact with the West Salton detachment fault. B-B' is also a SE-NE cross section just farther south than A-A' and extends from Inner Pasture to Carrizo Valley. The slip motion along the Coyote Mountain segment is right-lateral strike slip, but the subsidiary faults have an oblique component. The hatched damage zone encompasses all of the subsidiary faults.

mountain range. The tonalite weathers on the surface around the grains and breaks into large subrounded boulders that mantle the mountain slopes.

The Pliocene-Pleistocene Canebrake Conglomerate and Palm Spring Formation (QPc) are located in the northernmost section of the Tierra Blanca Mountains (Figure 14). The sedimentary deposits are composed of weakly-lithified pebbly sandstone and gray conglomerate derived from prebatholithic metamorphic rocks and tonalite cobbles, and a light gray to tan sandstone with interbeds of light red clay (Dibblee, 1996). Together, the

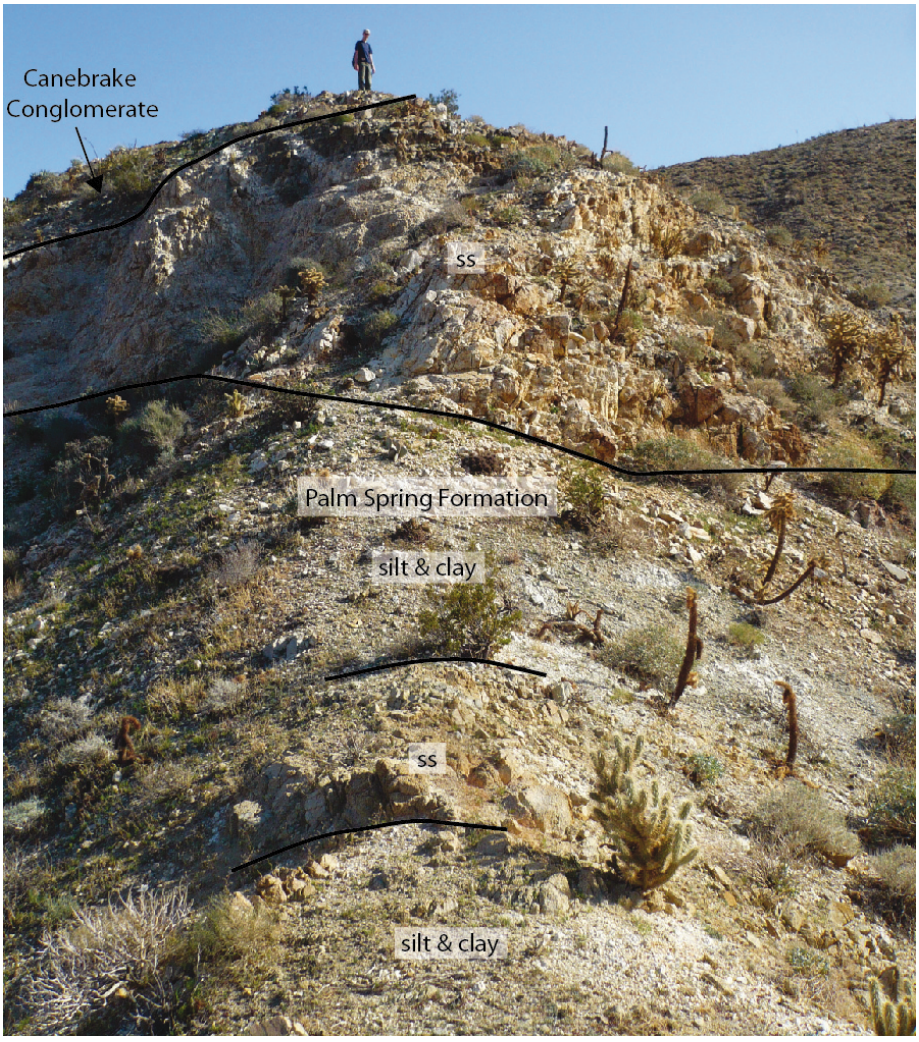

FIGURE 14 Photo of the Canebrake Conglomerate and Palm Spring Formation on the northernmost slope of the Tierra Blanca Mountains looking southeast. The Canebrake Conglomerate is composed of cobbles derived from the plutonic rock and prebatholithic metamorphic rocks. The Palm Spring Formation in this area is composed of siltstone, claystone, and sandstone. The sandstone crops out as blocky cliffs.

Canebrake Conglomerate and Palm Spring Formation form slopes and small ledges on the northern flank of the mountains.

Pre-intrusion metasedimentary gneisses and schists (gs) are located on the north-eastern part of the Tierra Blanca Mountains (Figure 11). The metasedimentary rocks form slopes and display variable colors. The metamorphic rock-derived units are intermixed

with cobbles, clasts, and fragments of the granitic pluton. Quaternary alluvium (Qal) fills arroyos and the large valleys adjacent to the Tierra Blanca Mountains as well as lows within the range. The alluvium is derived from weathered plutonic rock, the Canebrake and Palm Spring Formations, and the pre-plutonic metasedimentary units. The alluvial outwash forms fans that spread valley-ward. Alteration includes areas of orange and red stained fault gouge, white bleached fault gouge, and heavily grusified granite. The bleached tonalite forms slopes with erosional channels as little-to-no vegetation grows in the altered areas to stabilize the unit.

Most of the Tierra Blanca Mountain Range is composed of undeformed and unaltered La Posta tonalite defined by large quartz, plagioclase, and biotite grains, its cohesion between grains, and widely-spaced joints and fractures and the rocks weather in red and tan blocks (Figure 15). Todd (1977, 2004) mapped scattered, discontinuous northeast-striking faults through the Tierra Blanca Mountains that are typically concealed by grus and alluvium. Cobbles and boulders in the washes commonly exhibit coatings of epidote and chlorite mineralization and slickenlines (e.g. Site 8 discussed below). Some faults also are associated with linear bands of red-orange alteration (e.g. Site 6 discussed below). The rocks exposed in the arroyos entering west of the Carrizo Badlands on the eastern side of the Tierra Blanca Mountains are severely fractured at the mouths of the canyons (Figures 16 and 17), and the plutonic rock is increasingly cohesive farther into the mountains and away from the Coyote segment of the Elsinore fault system (Figure 18). Fault-slip related damage located around the mouths of the canyons is brittle, and the fragments of tonalite are cemented together with friable fine-grained powder derived from the tonalite.

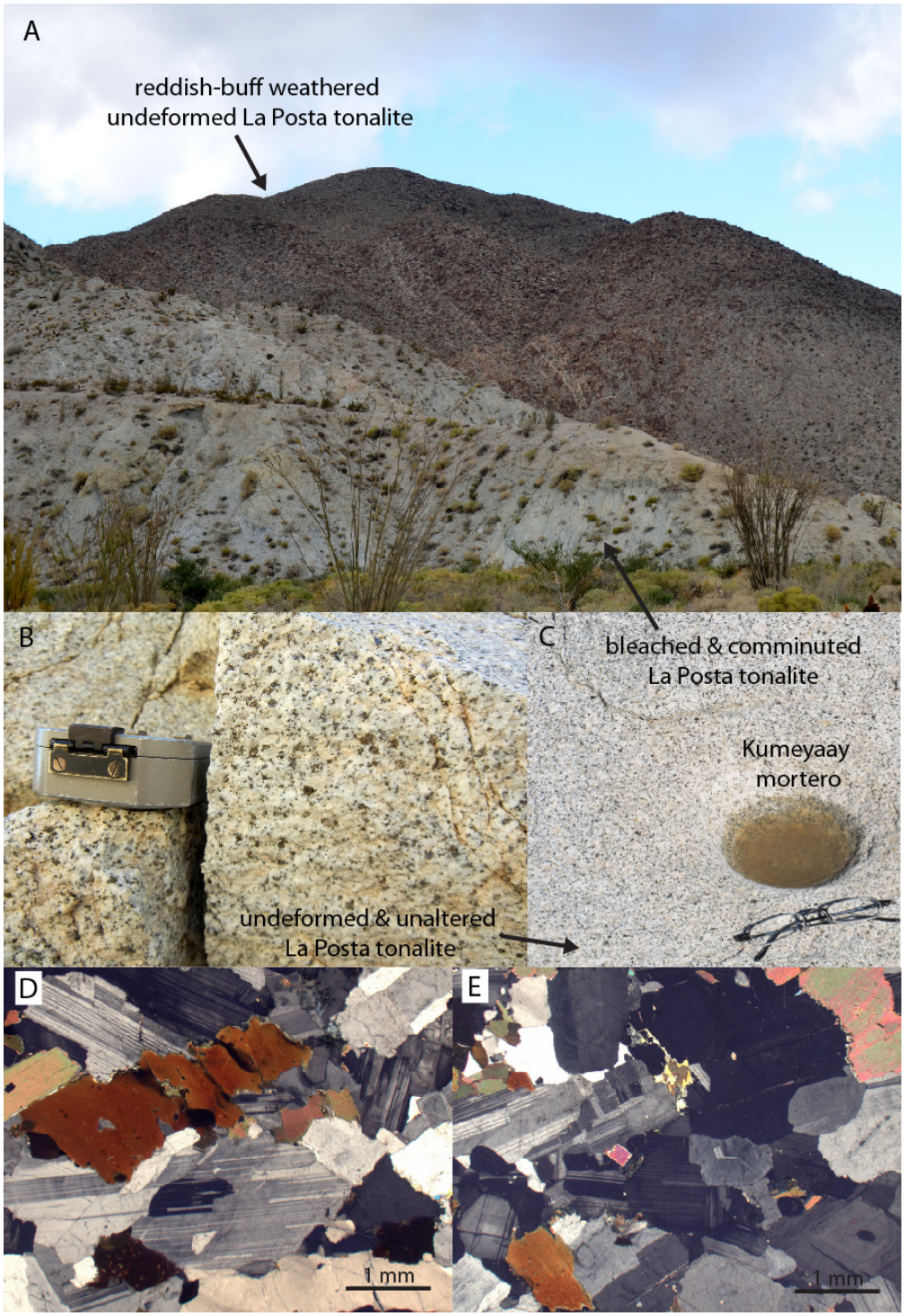

FIGURE 15 Undeformed La Posta tonalite throughout the Tierra Blanca Mountains. A—Tonalite weathers reddish-buff when not affected by faulting or fluid flow. B—Pristine La Posta tonalite, undeformed and unaltered, contains large crystals of quartz, plagioclase, and biotite. C—Unaltered and undeformed protolith. D-E—Thin sections of unaltered and undeformed La Posta tonalite (2.5x XPL).

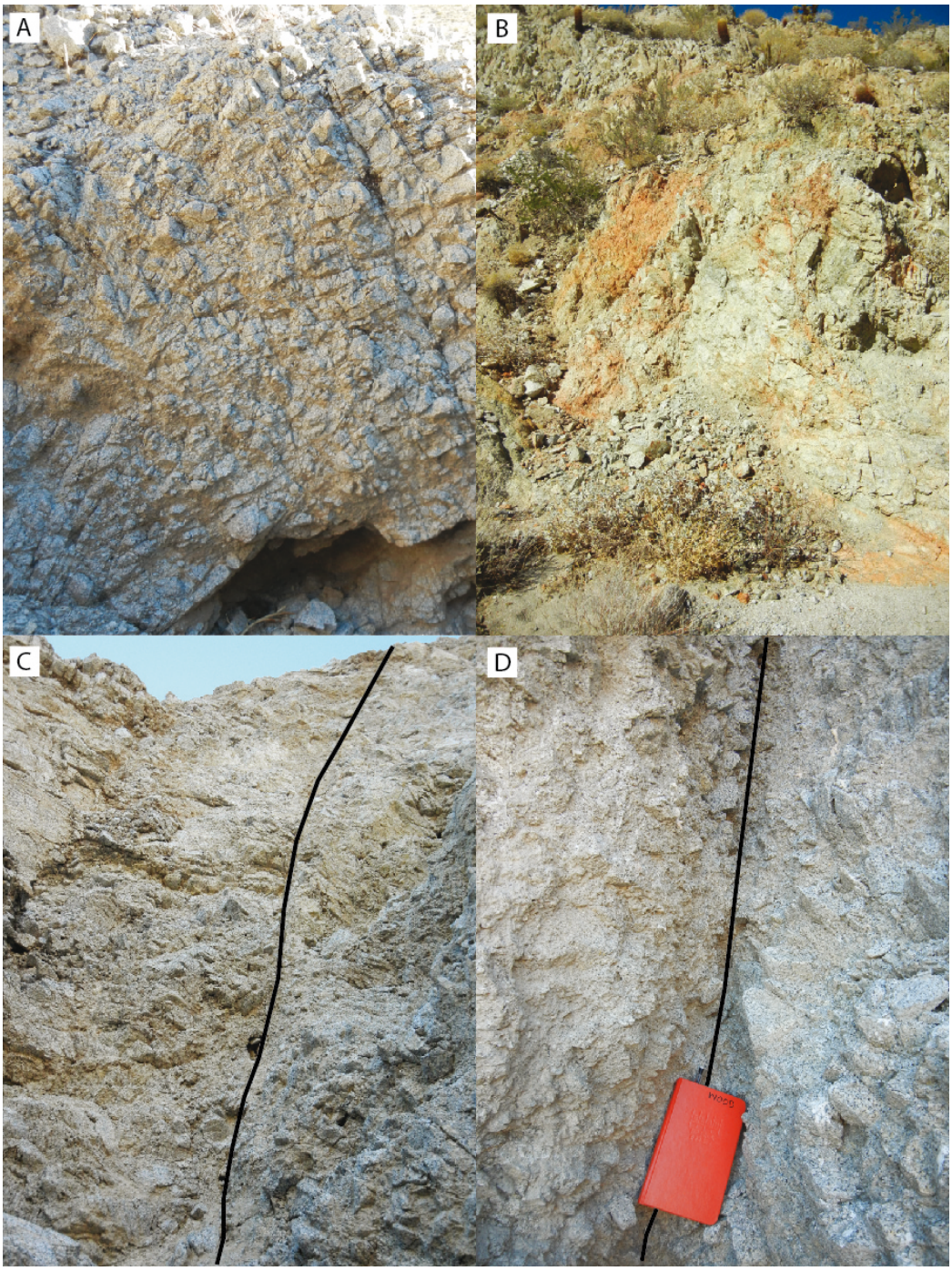

Figure 16 Examples of dense fractures near the mouths of the canyons along the northeastern flank of the Tierra Blanca Mountains associated with the Coyote Mountain segment of the Elsinore fault. A—Intense fracturing and grusification within the La Posta pluton. B—The tonalite experienced grain comminution, bleaching, and red staining. C—A small fault within severely fractured tonalite. The walls are jagged from the angular rocks created from fracturing. D—Close-up of the small fault and angular tonalite chunks in C with a notebook for scale.

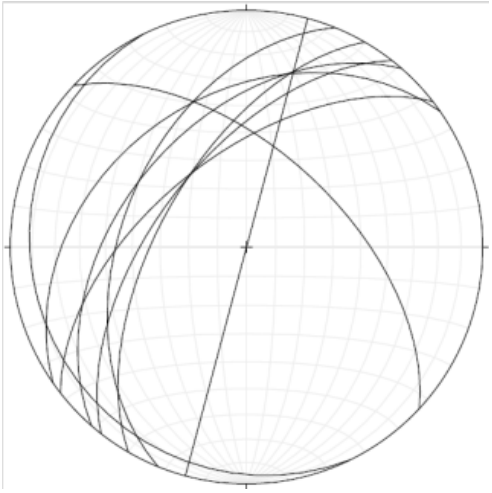

Figure 17 Stereonet showing the orientation of fractures from an outcrop located at 566149 m E 3645481 m N in an arroyo close to the Carrizo Valley.

I examined the plutonic rocks at thirteen locations for mesoscale observations mostly in the altered and damaged zones and along the fault networks in the Tierra Blanca Mountains (Figure 19). These sites were chosen for their proximity to and distribution along the Elsinore fault zone and the West Salton detachment fault and some localities for the presence of alteration. Additionally, three sites hosted scanline investigations (Figure 19) to examine damage and fracture orientations within or along the faults in the study area. Small faults discussed in this section are typically less than 150 m long in outcrop length and were located using aerial imagery and then visited in the field, where fault and fracture orientation measurements, geometry, and rock character observations were recorded. In the field, the faults are typically expressed by chlorite veins and exposed fault surfaces. General features of the small faults include steeply dipping fault planes, few preserved sense-of-slip indicators, and irregular clay-rich gouge coatings. The faults are associated with damage zone fractures within a larger fault zone, and all contain anastomosing chlorite veins paralleling the fault surface or within the fault core itself (Figure 20). Most of these short, laterally discontinuous faults are on the northeastern side of the Tierra Blanca Mountains, parallel or roughly perpendicular to the mountain front and the Coyote Mountain segment of the Elsinore fault. I present data from thirteen mesoscale study sites, mostly along the small faults, starting with the northwestern part of the study area to the southeastern sections of the Tierra

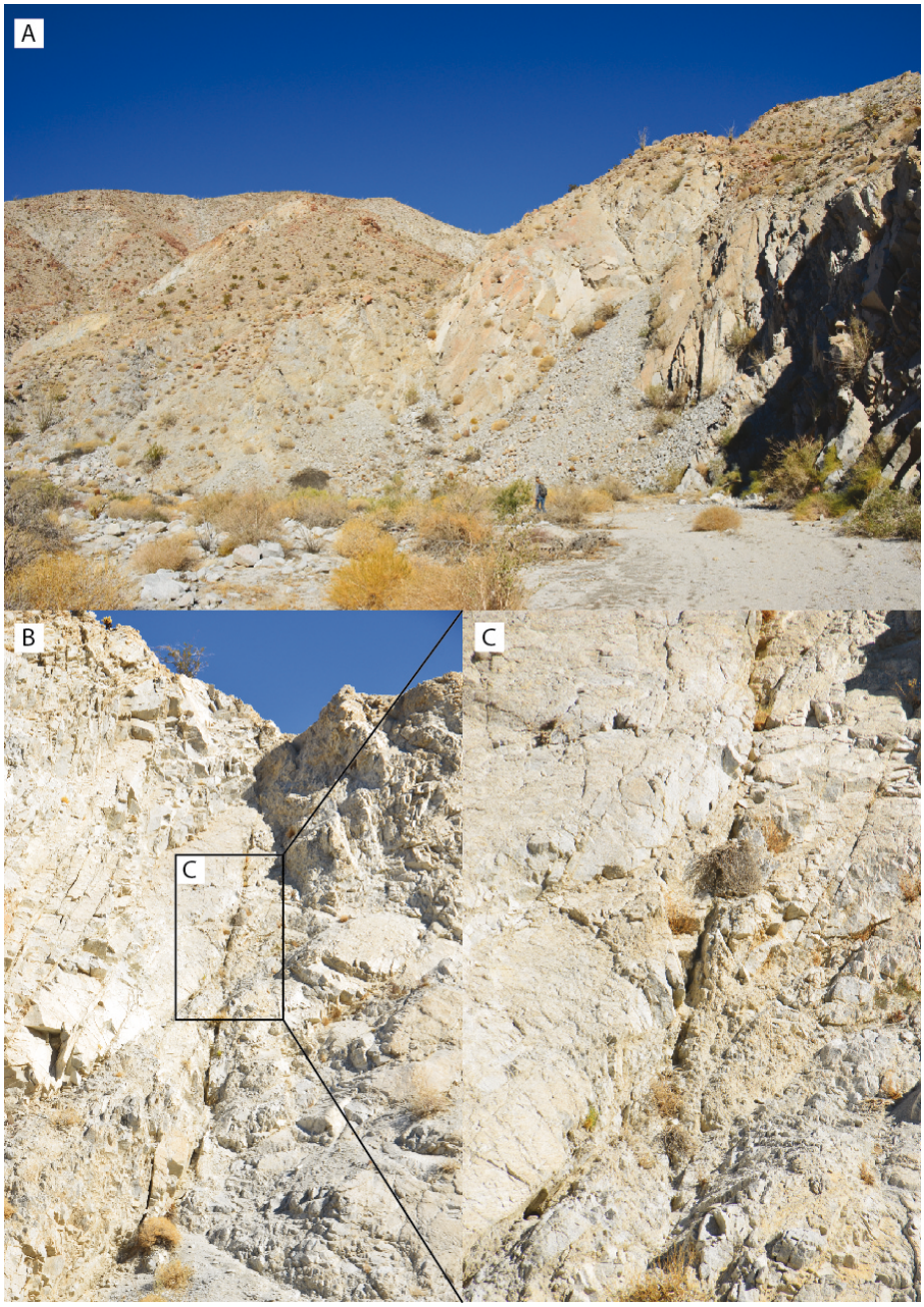

FIGURE 18 Photos of the La Posta pluton unaltered from fluid flow along the Coyote Mountain fault zone. In this location (567383 m E 3643697 m N) the tonalite exhibits large through-going fractures rather than the heavier, closely-spaced fracturing seen in the canyons to the north closer to the Coyote Mountain segment of the Elsinore fault (Figure 15). A—Looking west at well-exposed smooth fracture faces. The tonalite faces are coated in a red-brown varnish commonly seen within the Tierra Blanca Mountains away from the bleaching and alteration in adjacent to the faults. B—Nearly vertical open fractures within the La Posta pluton away from the Coyote Mountain segment of the Elsinore fault. C—A zoomed-in view of an open fracture.

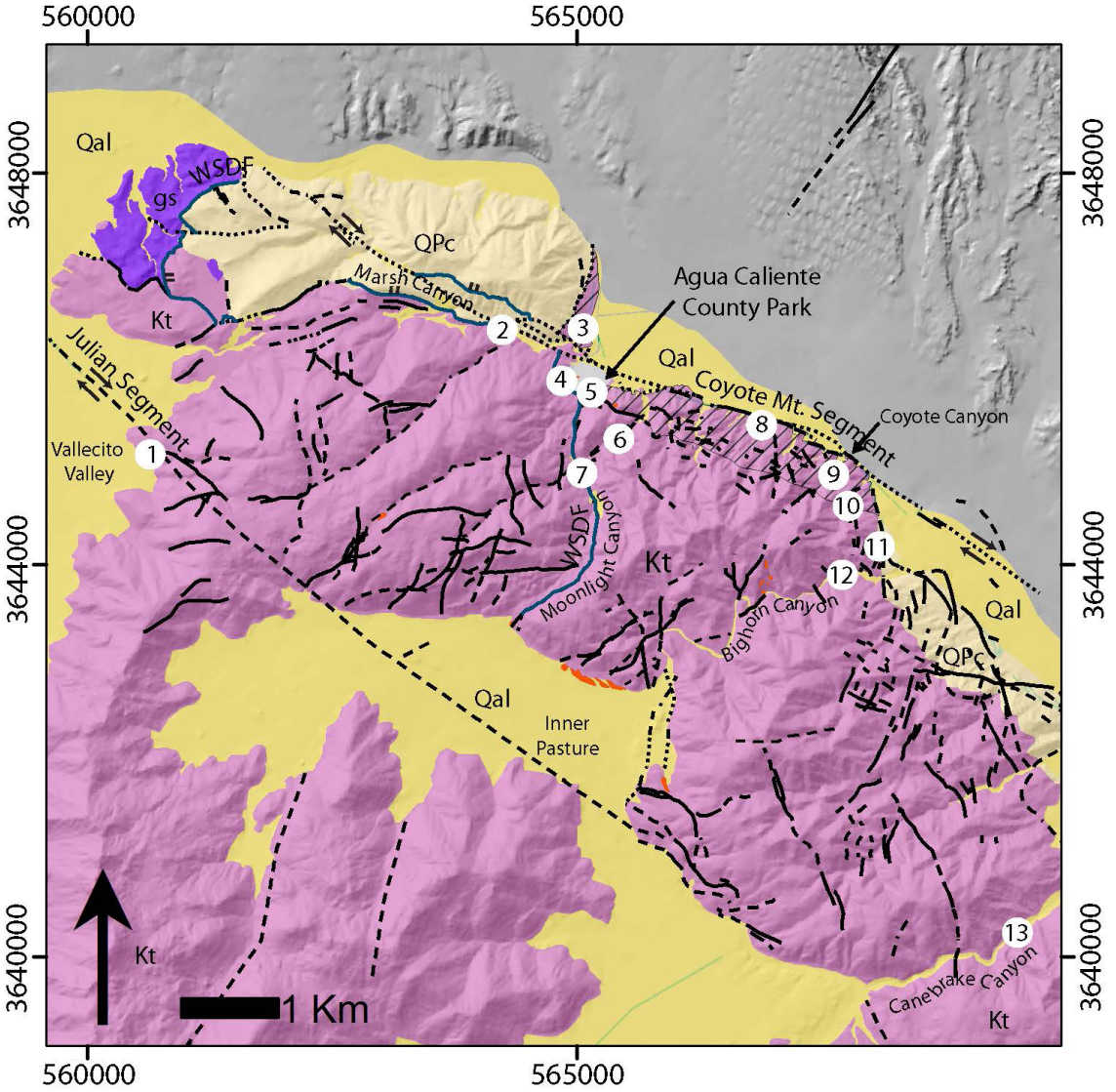

Figure 19 An index map for the mesoscale studies discussed in the text. The white markers are locations of mesoscale studies discussed in the text. All of the mesoscale studies are within the La Posta tonalite. Scanline locations were at Sites 2, 6, and 9.

Blanca Mountains in order to document observed features along faults and within the La Posta pluton.

Site 1 is in the northwest corner of the mountains on the edge of Vallecito Valley, where a concealed strike-slip fault (Figure 20A) enters the Tierra Blanca Mountains from Vallecito Valley striking 79° and the assumed dip is approximately vertical (Figure

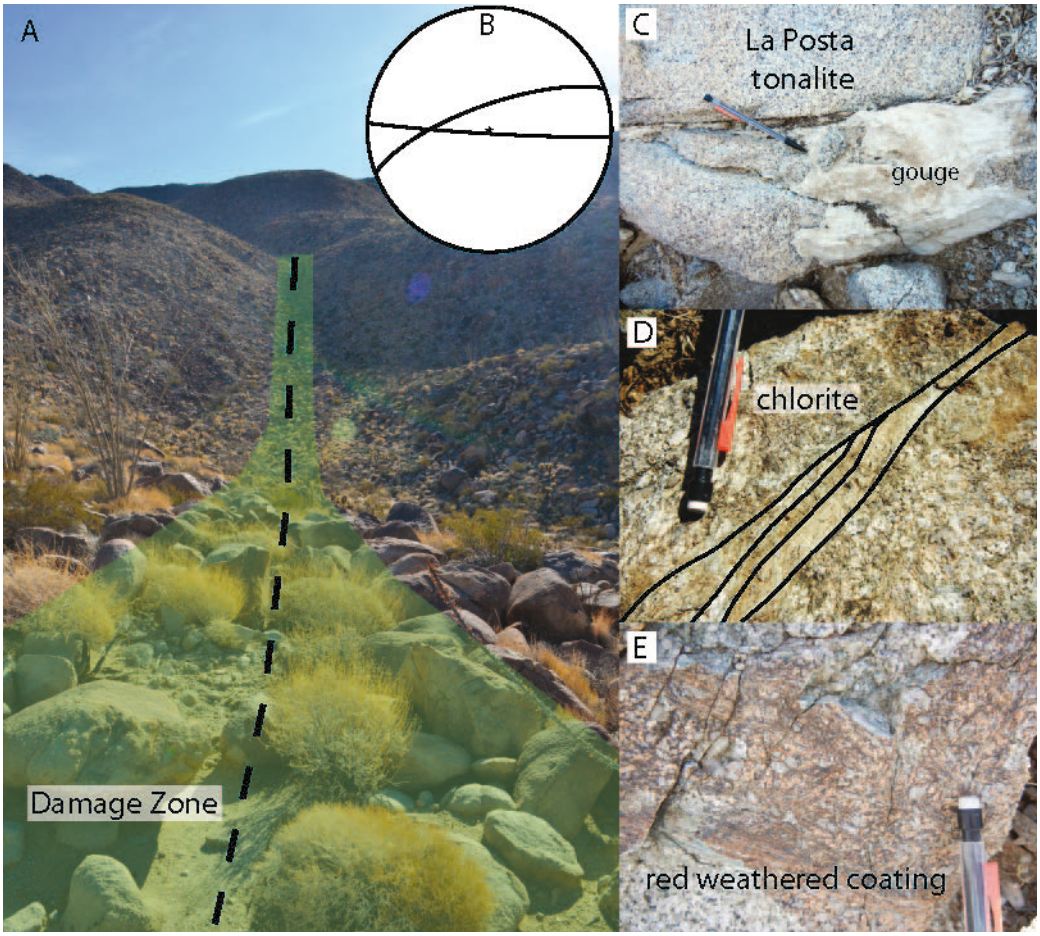

Figure 20 A view to the east of a concealed strike-slip fault at Site 1 (A) entering the Tierra Blanca Mountains from Vallecito Valley and striking east-west and the assumed dip is approximately vertical (B). An adjacent damage zone (green) is defined by gouge-filled fractures (C) and chlorite veins (D). Boulders and grus cover the fault trace. Many of the tonalite outcrops have a red weathered coating (E).

20B) though it is covered by tonalite boulders. An adjacent damage zone ~ 3 m wide is defined by gouge-filled fractures approximately ~ 2 cm wide (Figure 20C) and chlorite veins (Figure 20D). The gouge (Figure 20C) contains small clasts of quartz and plagioclase. Rocks along the fault contain green foliations that dip 88° and some samples have a red weathered coating (Figure 20E), but the red samples are intact, not powdered like the samples found around the county park. No grain size reduction was noticed along this

fault at this site.

Site 2 is east of the fault in Site 1 and has an exposed fault in the informally named Marsh Canyon (after Marsh Trail that leads partway through the canyon) at 564230 m E 3646419 m N (Figure 21). The canyon appears to mark a fault contact that divides the Quaternary Palm Spring Formation and Canebrake Conglomerate on the north form the La Posta pluton on the south. The outcrop is fractured in numerous orientations (Figure 21A) and is affected by both the detachment and the strike-slip fault. The fault plane is coated in a fine white gouge and preserves near-horizontal slickenlines on the tonalite (Figure 21B), evidence that the most recent movement was strike-slip. Grain sizes in the tonalite reach several millimeters. The chlorite veins interweave but the overall orientation is northwest-southeast (Figure 21C). On the southwest side of the veins, the protolith is intact, and the tonalite on the northeast is crumbly (Figure 21C). Slickenlines in the outcrop trend from 65 to 344° and plunges range from 6 to 59° (Figure 21D; ID 99 in Appendix A).

Directly north of the county park behind the Agua Caliente Springs General Store at Site 3 (565065 m E 3646440 m N; Figure 22), the tonalite of the La Posta pluton has a different character than the undeformed protolith (Figure 15) or the fractured tonalite south of the county park (Figure 16). Here, the tonalite is locally mylonitized and contains a fine-grained, chloritized protolith, and grus (Figure 22). A small fault striking 339° and dipping 59° east offsets the mylonite ~ 22 cm. Mylonite layers contain preserved tonalite bounded by the finer grained and chloritized protolith.

Agua Caliente County Park is centered at the highest concentration of alteration and intersecting faults in the study area (Plate 1). The West Salton detachment fault at

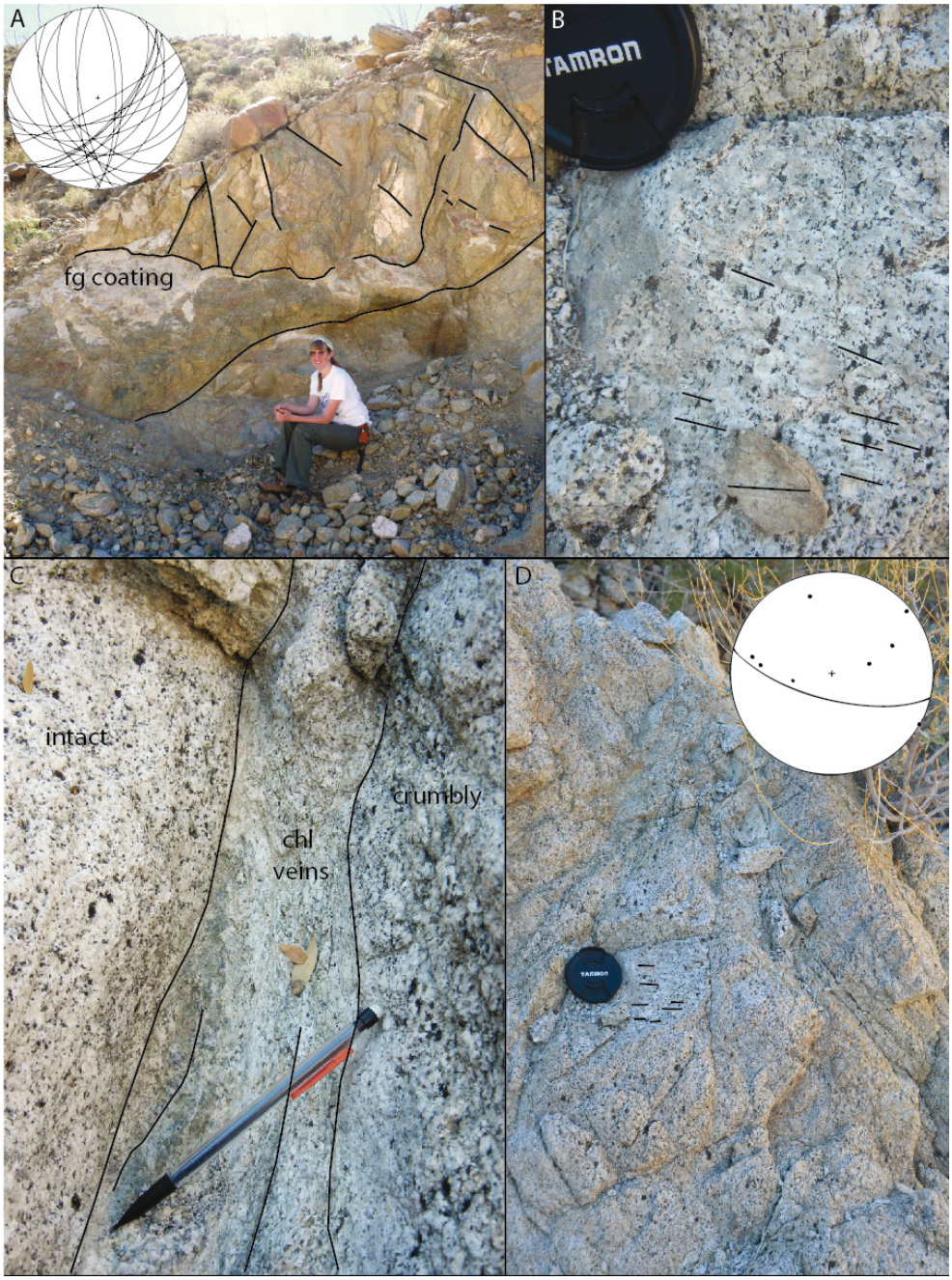

FIGURE 21 An outcrop located at Site 2 in Marsh Canyon. A—Outcrop of tonalite located at 564230 m E 3646419 m N. The scanline in Figure 12 was taken at this outcrop along the fault. The outcrop is very fractured and in numerous orientations. The visible fault plane is coated in a fine white gouge. B—Lateral slickenlines on the tonalite indicating the last preserved slip was strike-slip motion. C—Chlorite vein mesh adjacent to intact protolith on the southwest (left of veins) and crumbly granite to the northeast (right of veins). Pencil for scale. The chlorite veins interweave but the overall orientation is north-west-southeast. D—Fractured, friable tonalite with near-horizontal slickenlines. Grain sizes in the tonalite reach several millimeters.

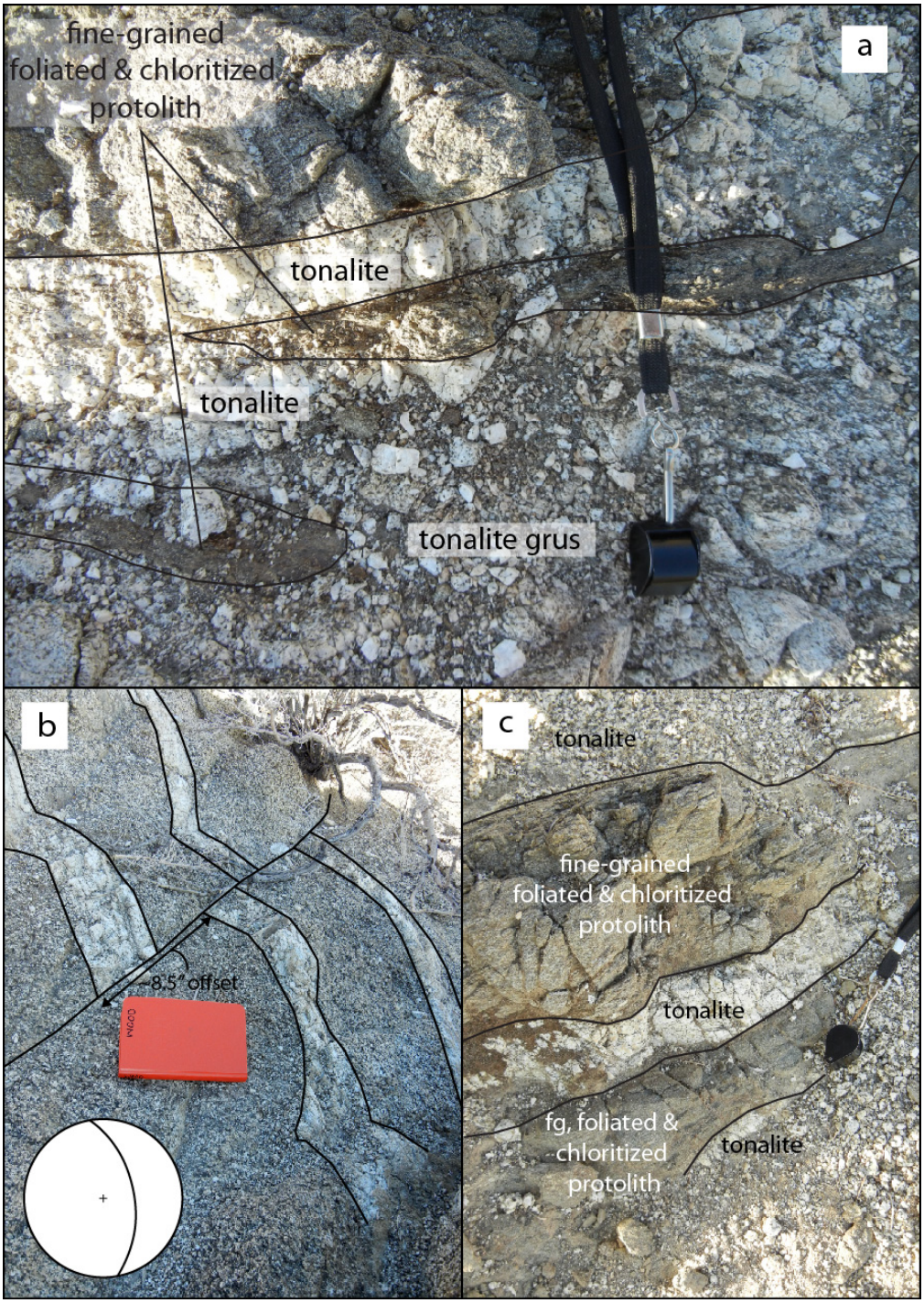

FIGURE 22 A fault damage collage at Site 3 within the Coyote Mountain segment damage zone. A—Mylonitized and chloritized protolith with tonalite and grus. Hand lens for scale. B—8.5 inch (21.59 cm) offset of preserved tonalite layers surrounded by the fine-grained and chloritized protolith. The fault strikes 339° and dips 59° east. Field notebook for scale. C—Additional view of the inter-layered tonalite and fine-grained foliated and chloritized protolith with hand lens for scale.

Site 4 is on the western side of the county park and for a short distance bounds the eastern flank of the Tierra Blanca Mountains (Figure 5). The fault at this location exhibits textural variations over a ~ 2 m area that represents different zones away from the principal slip surface. The fault plane has a red-brown foliated zone ~ 45 cm wide on the footwall side of the fault surface (564883 m E 3645837 m N). At this location the fault strikes 294° and dips 70°NE, which is very steep for a detachment fault. Eighty meters north of this fault surface is a corresponding plane that strikes 340° and dips 30°NE (Figure 23). The fault surface at this station (564843 m E 3645896 m N) was identified by its 0.6-2.5 cm fine-grained white gouge coating along the surface. The gouge contained small (~ 0.2 cm) clasts derived from the protolith and the gouge effervesced with dilute hydrochloric acid suggesting the presence of calcite (Figure 24). The contact between altered and comminuted bleached and stained granite and the fault gouge is sharp (Figure 24A). The white fault gouge coating the detachment fault surface is adjacent to a dark, foliated layer (Figure 24B-C). Beneath the foliated layer is a foliated fault gouge that is a fine-grained matrix that interweaves

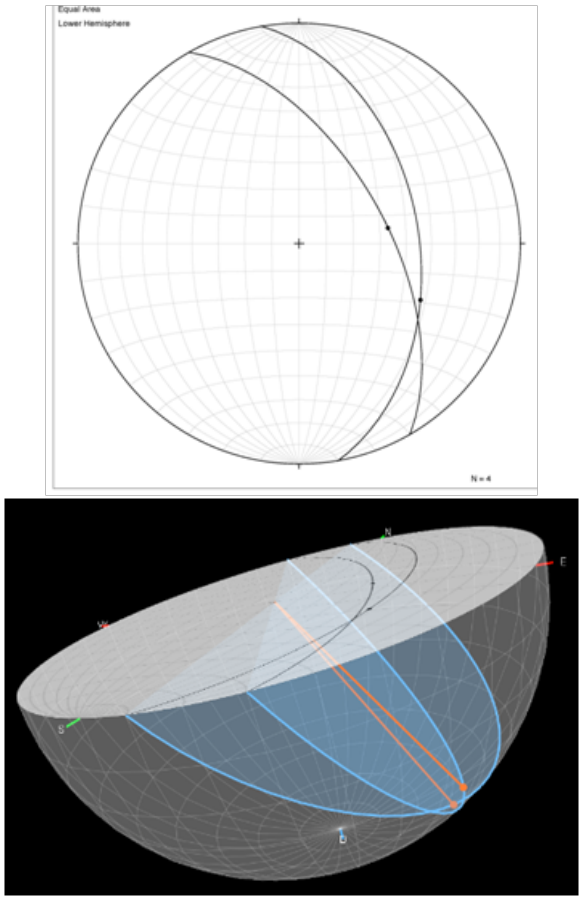

FIGURE 23 (Upper) Stereonet of the West Salton detachment fault surface located at 564854 m E 3645907 m N and at 565067 m E 3644898 m N. Recent slip indicator shows eastern and southeastern slip. (Lower) 3-Dimensional view of the fault planes and slip indicators.

around rounded clasts of the preserved tonalite (Figure 24D). The bleaching in the hanging wall of this fault is the most intense in the area (Figure 5), but the bleaching gradually diminishes intensity eastward and the protolith is concealed beneath Quaternary alluvium deposits.

On the southern edge of the park by the shuffleboards (565135 m E 3645779 m N), a prominent fault in outcrop at Site 5 strikes 287° and dips 27° (Figure 25). Slickenlines on the fault trend 30° and plunge 36° (Figure 25A). The fault strikes roughly parallel with the northeastern flank of the Tierra Blanca Mountains. Southeast of the fault exposure in Figure 25B foreground is a hill between the park and Moonlight Canyon that exposes orange and red staining in the heads of drainage channels toward the top of the hill (Figure 25B background). The fine-grained coating on the fault scarp is ~ 5-7 mm thick and the intact scarp varies from a few to >30 cm of scarp (Figure 25C). The alteration diagnostic to the county park is visible in the downthrown side of the West Salton detachment fault (Figure 25D). The fault exhibits dip slip (Figure 25A). The rocks in the hanging wall (east side) of the fault are chalky, fine-grained, bleached, occasionally stained, and friable. The footwall (west side) of the fault the rock is bleached, but not as friable and there are networks of chlorite veins and offset dikes. The dikes are 10-15 cm wide and are composed of plagioclase and quartz (Figure 25E). The host rock is recognizable La Posta tonalite though their numerous surfaces are coated in green chlorite and there are many chlorite vein networks. A ~ 11 cm sinistral offset of a dike segment within the La Posta tonalite in the up thrown side of the fault strikes. The chlorite veins in the small fault core anastomose in Figure 25F-G but the general strike is 309°. The anastomosing vein network encompasses granules and pebbles of the protolith.

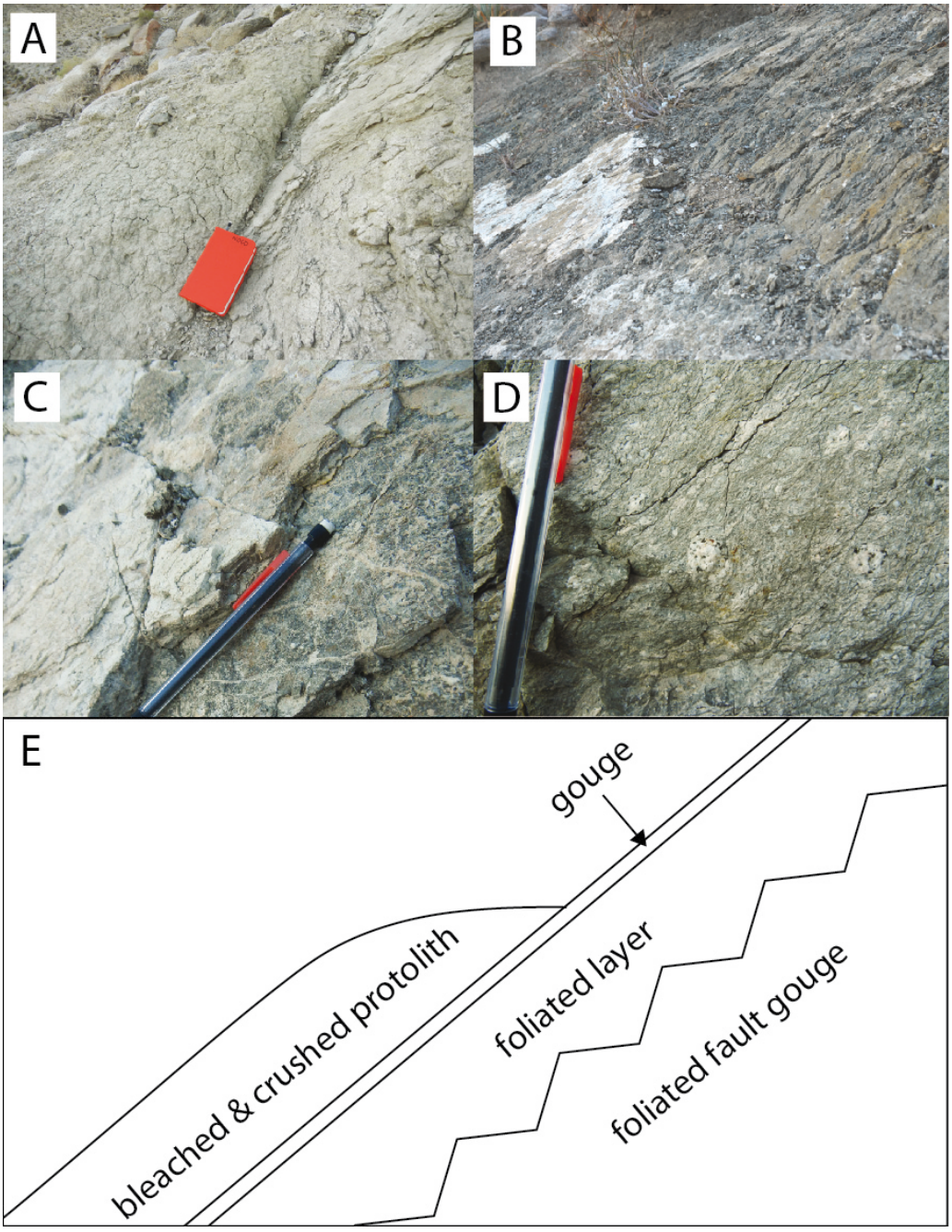

Figure 24 Photos from the West Salton detachment fault plane found on the western side of the county park at Site 4. A—The contact between altered and comminuted bleached and stained granite and the fault gouge is sharp. B—The white fault gouge coating the detachment fault surface is adjacent to a dark, foliated layer. C—Close up of contact between the fault gouge and the foliated layer. D—Beneath the foliated layer is a foliated fault gouge that is a fine-grained matrix which interweaves around rounded clasts of the preserved tonalite. E—A diagram of the fault facies.

The form of alteration in Moonlight Canyon is primarily bright orange to deep red staining rather than bleaching. The staining in Site 6 occurs in sections adjacent to faults where the protolith is intensely fractured (Figure 26A). The northern portions of the canyon are closest to the intersection of the Coyote Mountain segment and the West Salton detachment fault, so this area has experienced more fault-related movement than elsewhere in the range. Increased fault movement likely enabled iron-rich fluids to accumulate long enough to develop ankerite, ferrocolumbite, and various zeolites (Appendix D). A few outcrops throughout Moonlight Canyon have exposed slip faces, but a single face does not define these outcrops. Rather, they contain several surfaces at many orientations that preserve slickenlines on lightly polished faces with chlorite coatings and veins (Figure 26B). The red staining is concentrated in the finer grained remnants of the

Figure 25 (Following page) A small fault visible in the southern edge of the county park at Site 5. A—DOQQ and mapped faults at Agua Caliente County Park. The northwest-striking fault with the accompanying stereonet dips to the northeast and down-dip to slightly right-lateral slickenlines. Axen also observed down-dip slickenlines on this section of the detachment fault (blue line). The fault is parallel to the strike of the Tierra Blanca Mountains (unpublished, with permission). B—Close-up view of the dip-slip-oblique fault in A. The rocks on the northeast side of the fault (left of the fault trace) are chalky, fine-grained, bleached, occasionally stained, and friable. On the southwest side of the fault (right of the fault trace) the rock is still bleached, but not as visibly friable. There are networks of chlorite veins and offset dikes. C—Close-up of the fault in B. The fine-grained coating on the fault scarp is ~ 5-7 mm thick and the intact scarp varies from a few to >30 cm of scarp. D—Looking west at the fault scarp of the fault in C (green). The northeast side of the fault (right of fault) is chalky, bleached, and stained. In the distance, the alteration diagnostic to the county park is visible in the downthrown side of the West Salton detachment fault. E—Offset dikes in the upthrown side of the fault in C. The dikes are 10-15 cm wide and are composed of plagioclase and quartz and no biotite. The host rock is recognizable La Posta tonalite though there numerous surfaces are coated in green chlorite and there are many chlorite vein networks. F—An ~ 11 cm sinistral offset of a dike segment within the La Posta tonalite in the upthrown side of the fault in C. G—Close-up of anastomosing vein network in the upthrown side of the fault in C that strikes ~ 309° and encompasses granules and pebbles of the protolith.

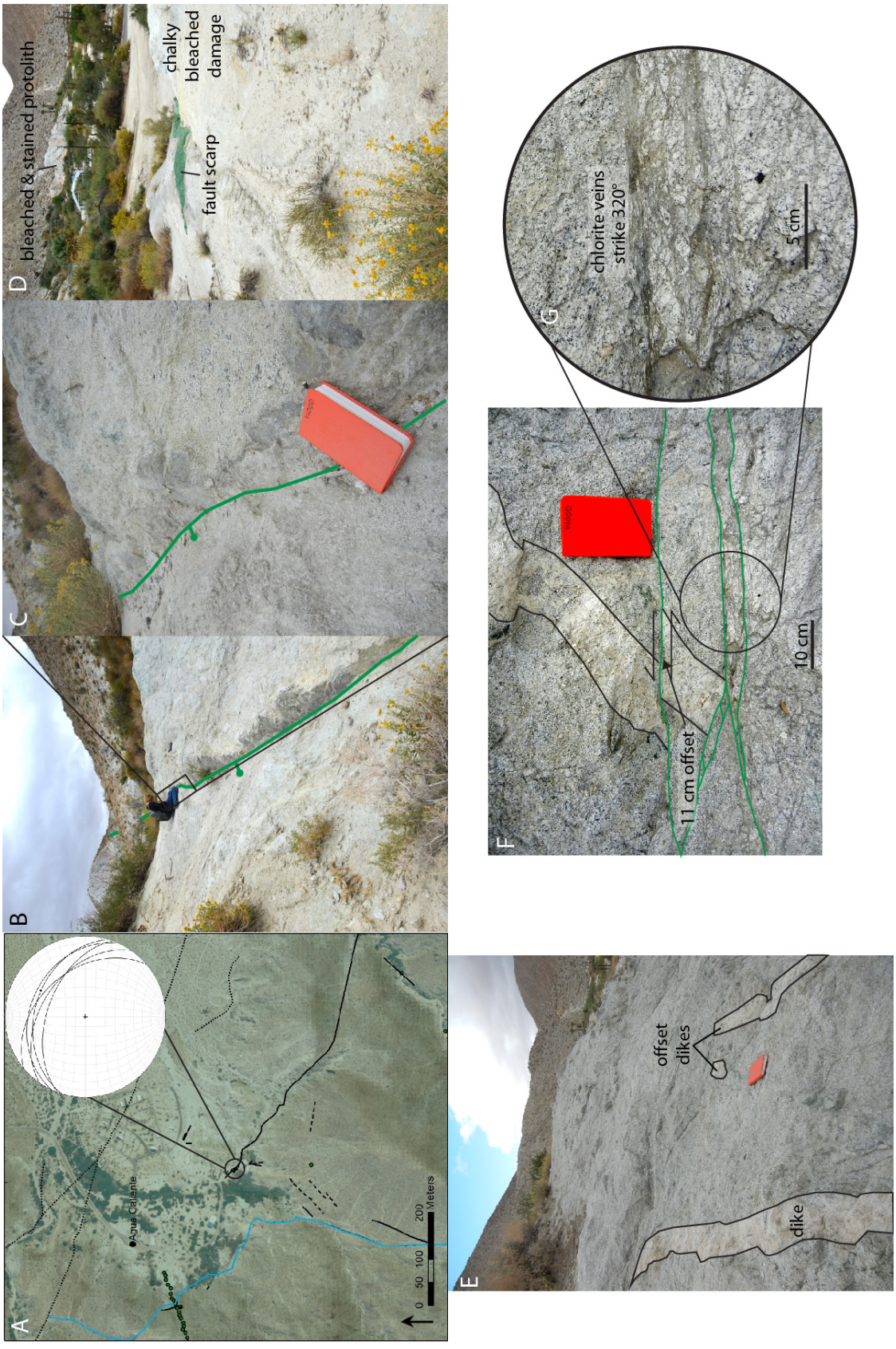
A
Agua Caliente
0 50 100 200 Meters
B
C
D
bleached & stained protolith
chalky bleached damage
fault scarp
E
offset dikes
dike
F
11 cm offset
10 cm
G
chlorite veins strike 320°
5 cm

comminuted tonalitic protolith and leaves larger feldspar crystals and quartz aggregates unstained (Figure 26C). The staining is most pronounced along the many fractures in the outcrops and the red and orange fade with distance from the fractures. The protolith is weakly lithified, plagioclase grains are powdery, and biotite grain sizes are reduced in comparison to the pristine booklets and sheets found to the south in Canebrake Canyon and the informally named Bighorn Canyon. All of the fractures observed in the stained outcrops are filled with a very fine-grained white powder derived from the ground protolith or dark green veins of chlorite (Figure 26B, D), and the fractures dip east to northeast. Most of the faces on the outcrop host slip indicators that vary from horizontal to vertical (Figure 26E). Farther south along the canyon at Site 7 is a small fault trace (A) with anastomosing fault strands (Figure 27B). The fault network is several meters wide defined by the width of the anastomosing strands (Figure 27B). Each strand has an accompanying fault core with widths up to 10 cm. The core is defined by very fine-grained fragments of protolith interspersed with chunks of plagioclase and quartz (Figure 27C). In some instances the cores contain calcite and sheared biotite veins (Figure 27D).

The most prominent fault trace in Moonlight Canyon strikes north-south (Figure 27). The most recent slip motion based on slickenline orientations is right-lateral oblique-normal or left-lateral oblique-thrust (Figure 27A). The fault zone is comprised of numerous anastomosing fault cores each ~ 9 cm wide (Figure 27B-C). The fault located at 565162 m E 3645044 m N exhibits down dip lineations and strikes 239° and the outcrop-scale slip surfaces dip 55°, 67°, and 78° N. A mesh of red and orange veins, some reaching several centimeters wide, characterizes this small fault in Moonlight Canyon. The veins are chloritic but not consolidated in one thin layer, and the orange to red alteration

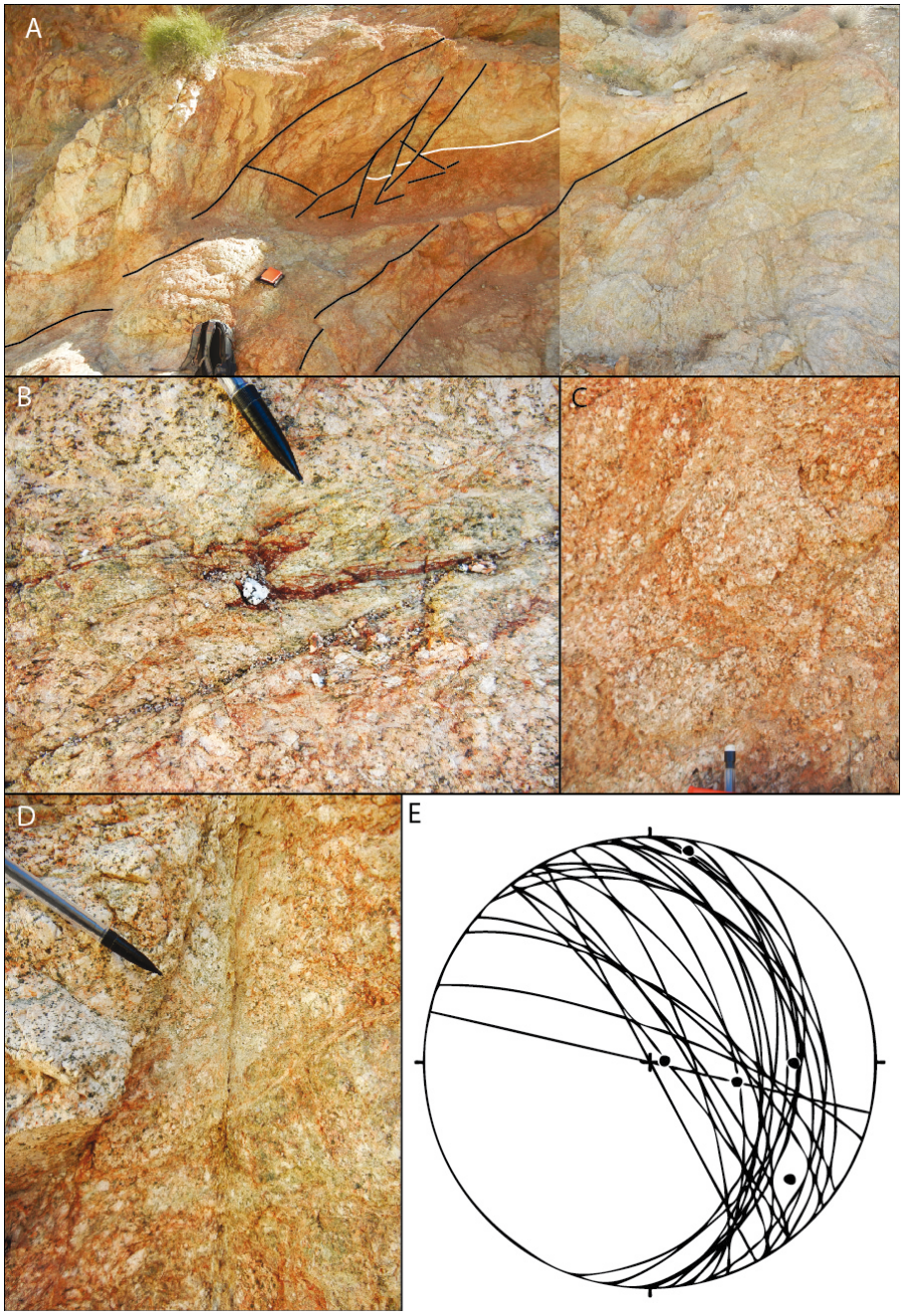

FIGURE 26 Faults and fault-related alteration at Site 6 in Moonlight Canyon at the outcrop selected for the Moonlight Canyon scanline (565423 m E 3645312 m N). A—Panoramic of the outcrop for Scanline 2 (Figure 12). The outcrop is fractured and stained red. B—Close-up photo of the damaged and stained protolith. Consolidated zones of chlorite display evidence of shearing. The protolith still retains original the tonalite coarse grained texture, but the plagioclase crystals are powdery and the quartz crystals are fractured. C—The orange and red staining is in the fine-grained matrix surrounding larger plagioclase and quartz crystals. D—Filled fractures in the stained outcrop. E—Stereonet of predominately north-south striking east dipping fractures and slip surfaces in the stained outcrop.

and staining form a halo or envelope around and along the chloritic zone. These stained chlorite veins are in some places ~ 16 cm thick while others are only ~ 1 cm thick. The immediate damage enclosing the mesh is 1.55-1.68 m wide. The bounds of the damage were determined visually based from the contact between the external veins and the more cohesive protolith. The damage zone of the fault along Moonlight Canyon is ~ 7 meters wide before the fault enters Inner Pasture and is lost beneath valley fill. The zone is made of red-orange powder and the rock is significantly broken and ground into powder. The area is altered and heavily fractured. The fault strikes 35° and dips ~ 50° southeast upon its reaching Inner Pasture ~ 2.5 km south of the county park.

Site 8 hosts a small cross fault system visible for ~ 7 to 8 meters (Figure 28A-B) near the mouth of a canyon entering the Carrizo Valley. The tonalite is crushed throughout the wash, but the grain sizes are not visibly reduced compared to the outcrops closer to the park (Figure 28C-D). The cross fault has slickenlines with a corrugated chlorite surface (Figure 28E), a chlorite gouge zone ~ 1.2 meters wide (Figure 28F-G), numerous planes cutting the outcrop, and slip indicators trending ~ 240° and plunging ~ 20°.

In Coyote Canyon (Site 9), a fault (Figure 29A) strikes 129° and dips 86° southwest (Figure 29B), and the exposed surface is coated in a rough, amorphous mud-like gouge that did not preserve visible slip indicators (Figure 29C). In the next canyon south, at Site 10 (Figure 30A), two faults intersect (Figure 30A inset). The fault striking 72° and dipping 46° S has near horizontal lineations, parallel to the canyon. Beside the fault is another fault striking 8° and dipping 62° E (Figure 30B-C). The surrounding rocks are fractured and have associated dull to earthy red staining (Figure 30D). These faults are associated with the cross faults linking the Coyote Mountain and Julian segments, and the

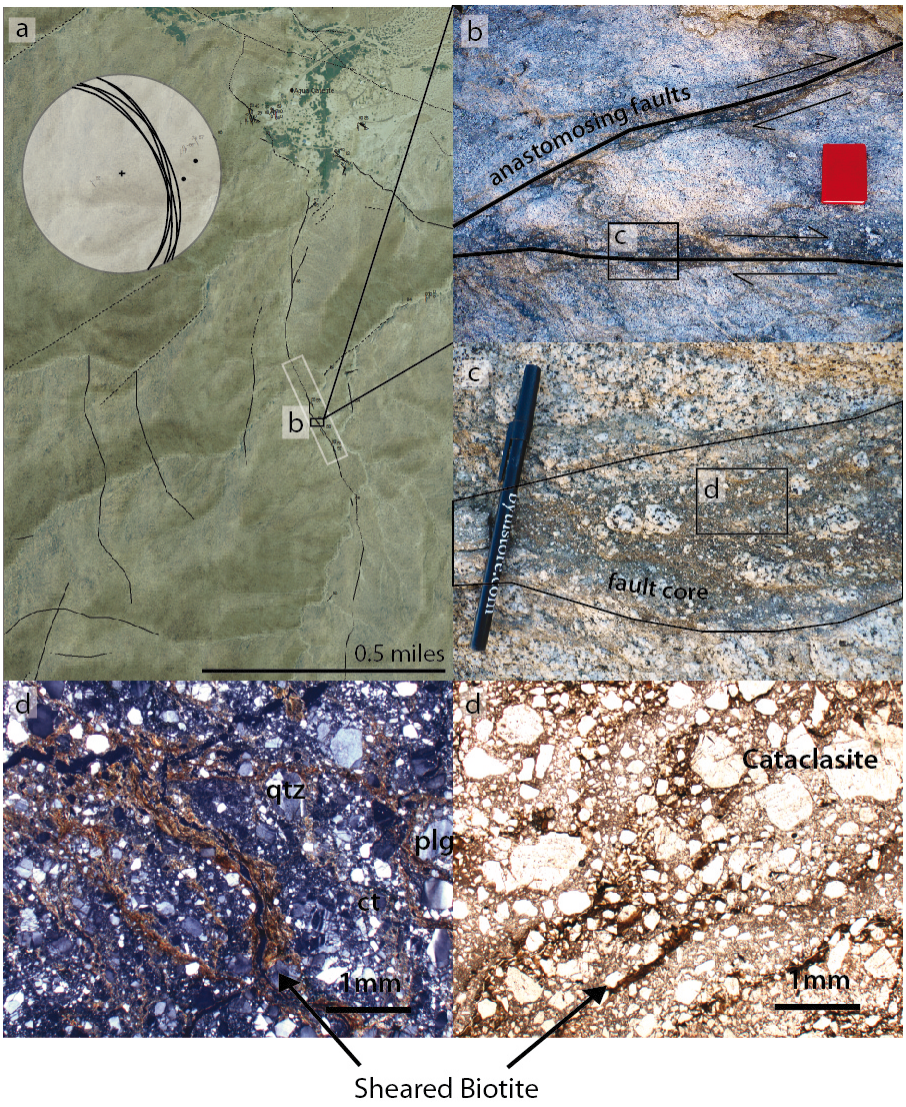

FIGURE 27 A fault along Moonlight Canyon south of Agua Caliente County Park at Site 7. A—Map view of a section in the Tierra Blanca Mountains. The boxed area corresponds with the inset stereonet and orientations of the fault. The orientation of the fault changes slightly along the boxed area of the fault and five measurements plotted are 330° 58° NE, 335° 59° NE, 333° 50°NE , 345° 52° NE, 345° 55° NE. B—Slip zones anastomose along the main strike of the fault and trend and plunge data support right-handed slip though this area has been mapped as the trace of the West Salton detachment fault. The shear zones transition to the protolith and fault offshoots, like the one pictured, create mesoscale lenses along the trace. C—Close up of the cataclasite shear zone with chunks of identifiable host rock caught in the crushing. D—(Right) Thin section from a fault core composed of cataclasite and shear zones. The matrix appears foliated between dark red to light gray though the clasts caught in the matrix do not exhibit composition divisions. PPL 10x. (Left) Sheared biotites within cataclasite. Comminuted quartz and plagioclase crystals remain intact enough to identify and there are small zones of calcite precipitation. XPL 10x.

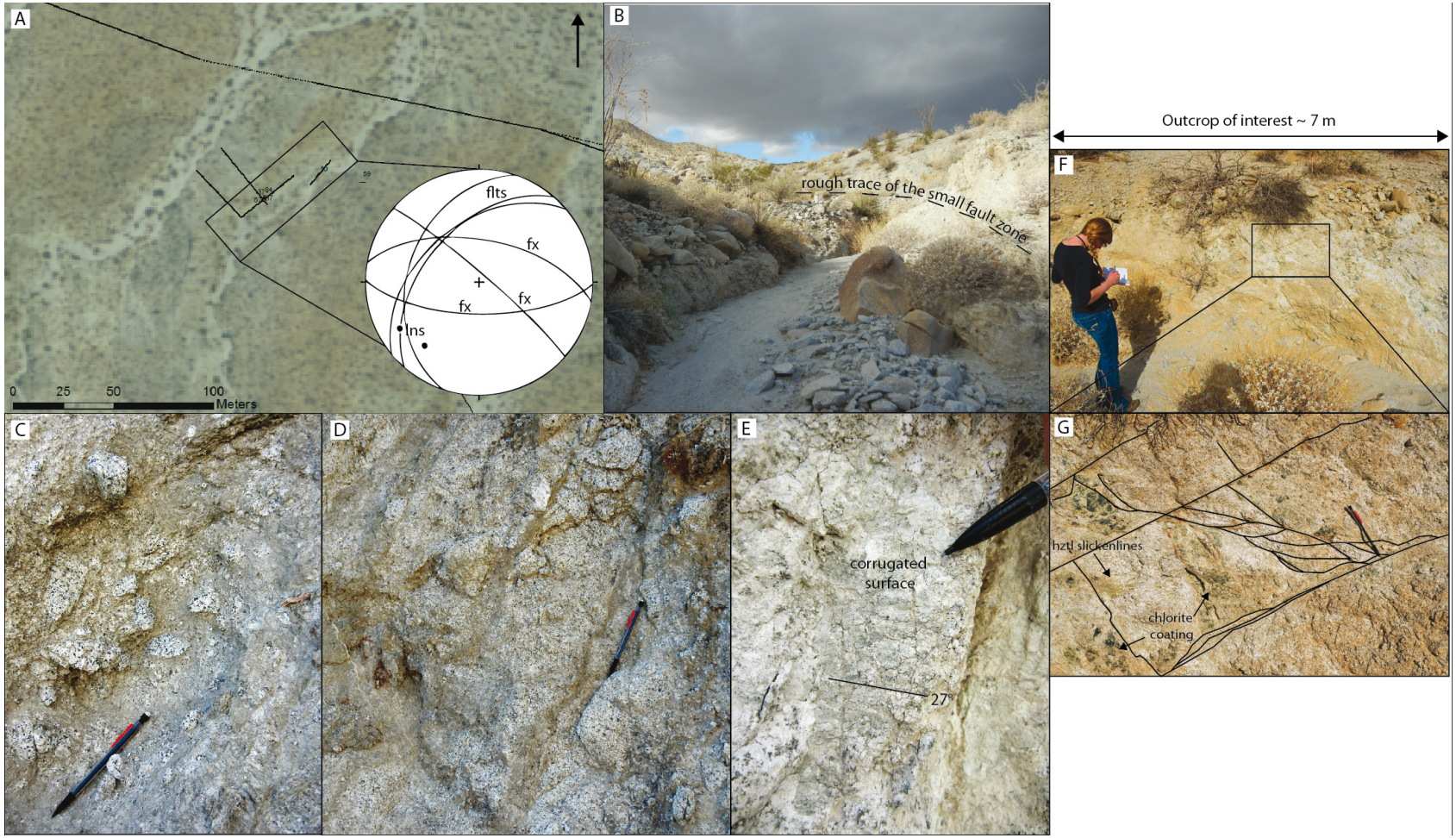

FIGURE 28 Outcrop photos of a cross fault. A—A northeast-striking cross fault located at 566956 m E 3645445 m N is found in an arroyo adjacent to the Carrizo Valley. B—The fault is approximately on strike with the arroyo. C and D—Damage along the fault. E—Nearly horizontal slickenlines on a corrugated slip surface. F—The fault zone contains sections of anastomosing chlorite veins. G—Zoomed view of the anastomosing chlorite veins and chlorite-coated host rock.

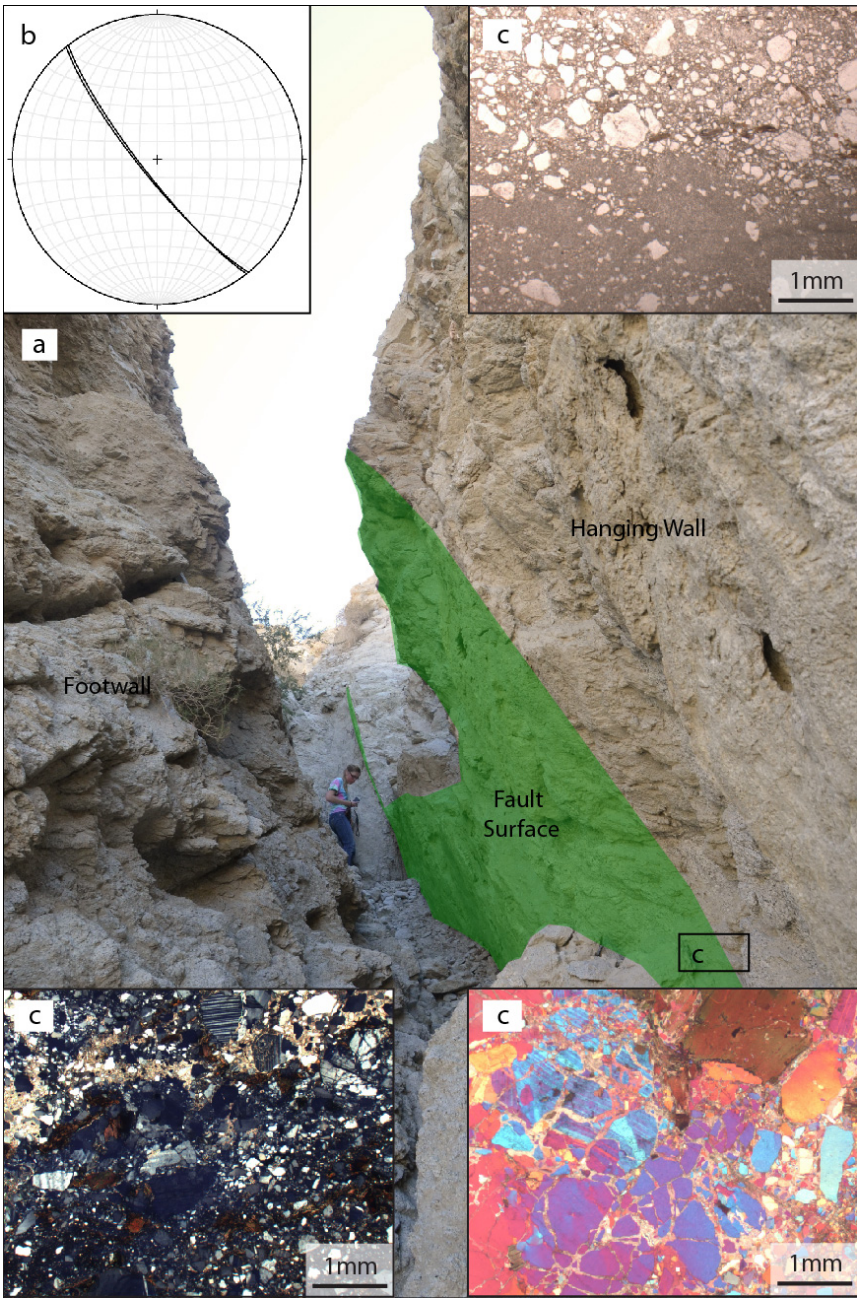

FIGURE 29 Fault exposed at Site 9 striking 141° and dipping 80° SW. A—Fault surface (green) is coated in an amorphous muddy layer preserving no visible slip indicators. B—The fault strikes northwest-southeast, paralleling the Tierra Blanca Mountains, and dips steeply to the southwest. C—A thin section from sample containing the muddy gouge and the hanging wall rock. The gouge is fine-grained calcite precipitated around the comminuted wall rock composed of quartz, plagioclase, and biotite pieces. Some of the biotite is sheared parallel to the fault surface. Two large fractured crystals of quartz and plagioclase crystal have most of the pieces close with calcite filling the openings. The upper right thin section photo is PPL 10x and the two lower sections are XPL 10x.

slip vector supports the hypothesis of lateral movement along linkage faults.

In a rare scarp visible within alluvium along the mountain front at Site 11, north of the informally-named Bighorn Canyon, the fault surface strikes 21° and dips 52° east (Figure 31). The surface is coated in an off-white fine-grained calcite gouge (Figure 31) surrounding cobbles of the Quaternary Palm Springs and Canebrake Formations. The exposed scarp extends for ~ 20 m across the mountain front and reaches more than 0.5 m wide. In aerial imagery the scarp is a white streak across the mountain front and corresponds with a normal fault surface mapped by Todd (1977) and Dorsey et al. (2012). No slip indicators were seen on this scarp.

At Site 12 in the informally named Bighorn Canyon, the protolith is hard and intact, grain sizes increase and there are clear, euhedral hexagonal biotite booklets (Figure 32). Very large and continuous fractures form cliff faces through the canyon, and there are some small faults located in a south-facing cliff (Figure 32A). One fault dips to the west (Figure 32A), and the other is vertical. The immediate damage zone for the west-dipping fault is asymmetric. The east side of the fault in Figure 32B exhibits damage consisting of very friable tonalite while the protolith on the west side of the fault is intact. The fault core is composed of numerous foliated anastomosing chlorite veins, and no slip indicators were observed (Figure 32B-C). Overall, rocks in this canyon are much less altered than northwest toward the county park. The tonalite is indurated and coarse-grained with subhedral to euhedral grains of quartz, plagioclase, and biotite.

Canebrake Canyon is ~ 7 km southeast of Agua Caliente County Park (Site 13; Figure 33) and trends nearly perpendicular to the trace of the Elsinore fault. The La Posta tonalite within the canyon is fractured, but the fractures have a lower density than frac-

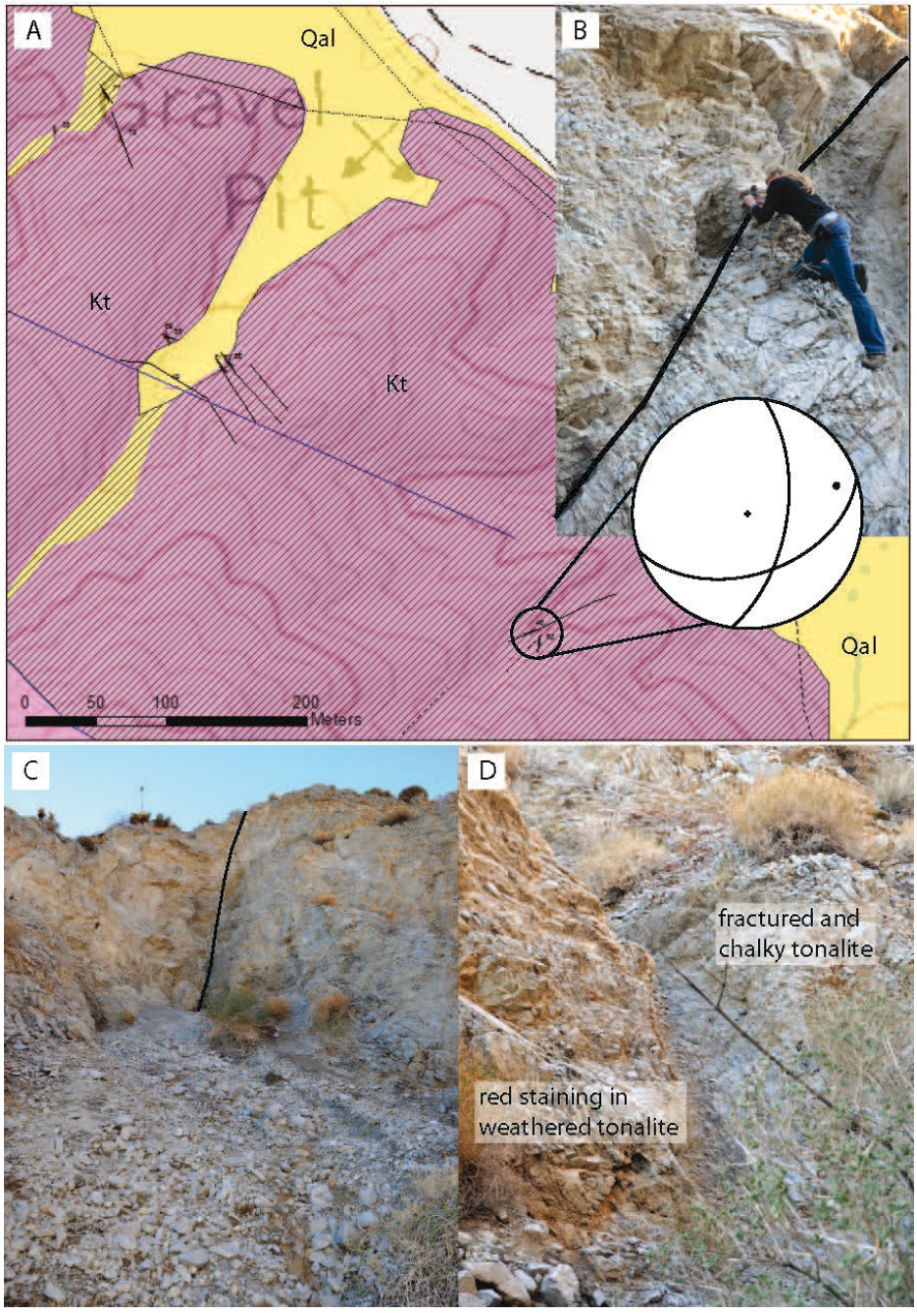

FIGURE 30 A—Portion of the map (Plate 1) covering the area at Site 10. A small fault strikes east-northeast. B—Field photo from the circled faults in A. Both sides of this fault are fractured and weathered, and the fault strikes 72° and dips 46° SE and has slickenlines plunging 20°. C—View to the south from the canyon at a fault striking 8° and dipping 62° E. D—Red staining and bleaching in the damage zone of a fault in A.

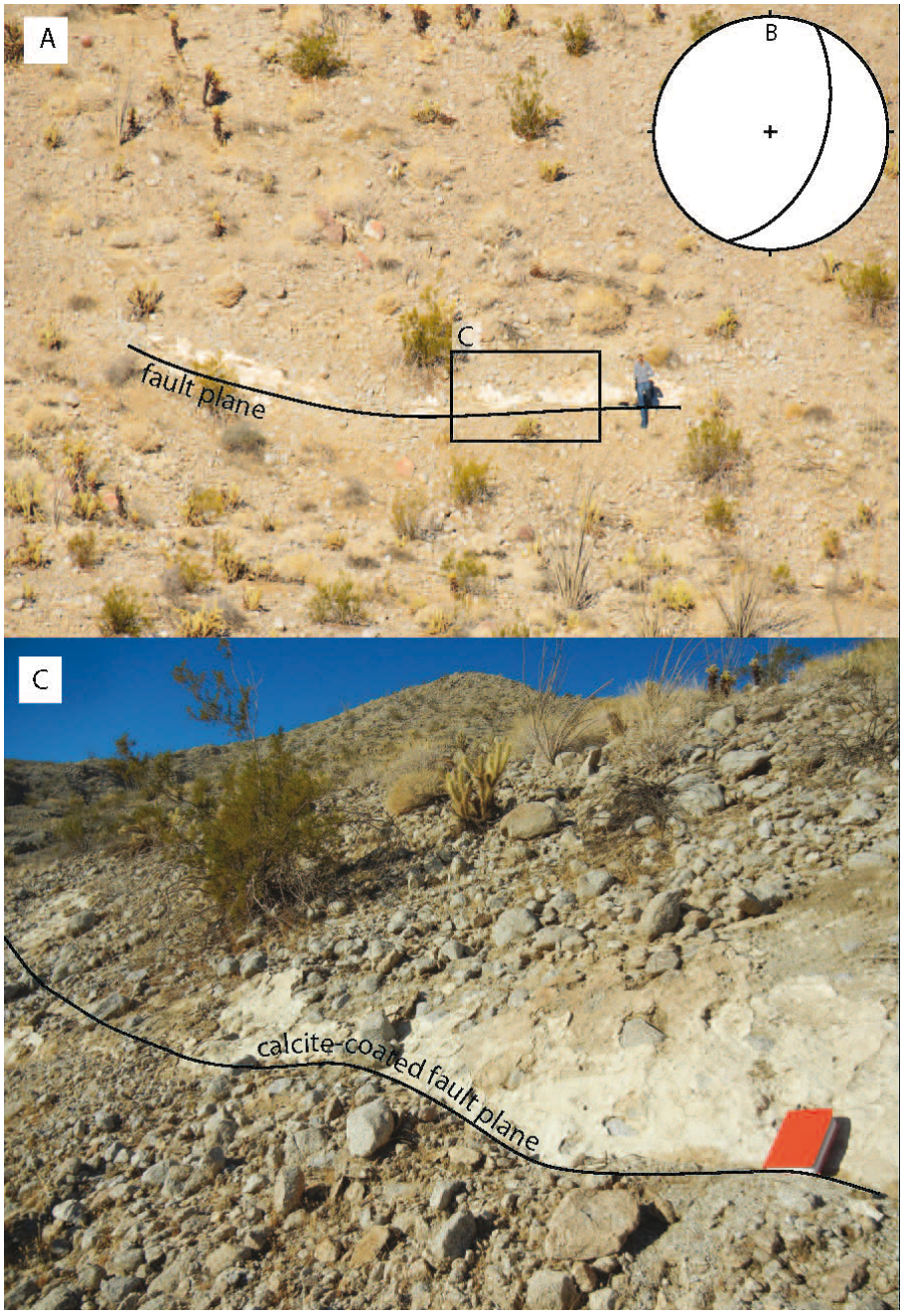

FIGURE 31 A mountain front fault located at Site 11. A—The fault plane is a white planar surface paralleling the mountain front. B—The fault strikes 10° and dips 52° east. C—Close-up photo of the fault. The fault scarp is coated in calcite.

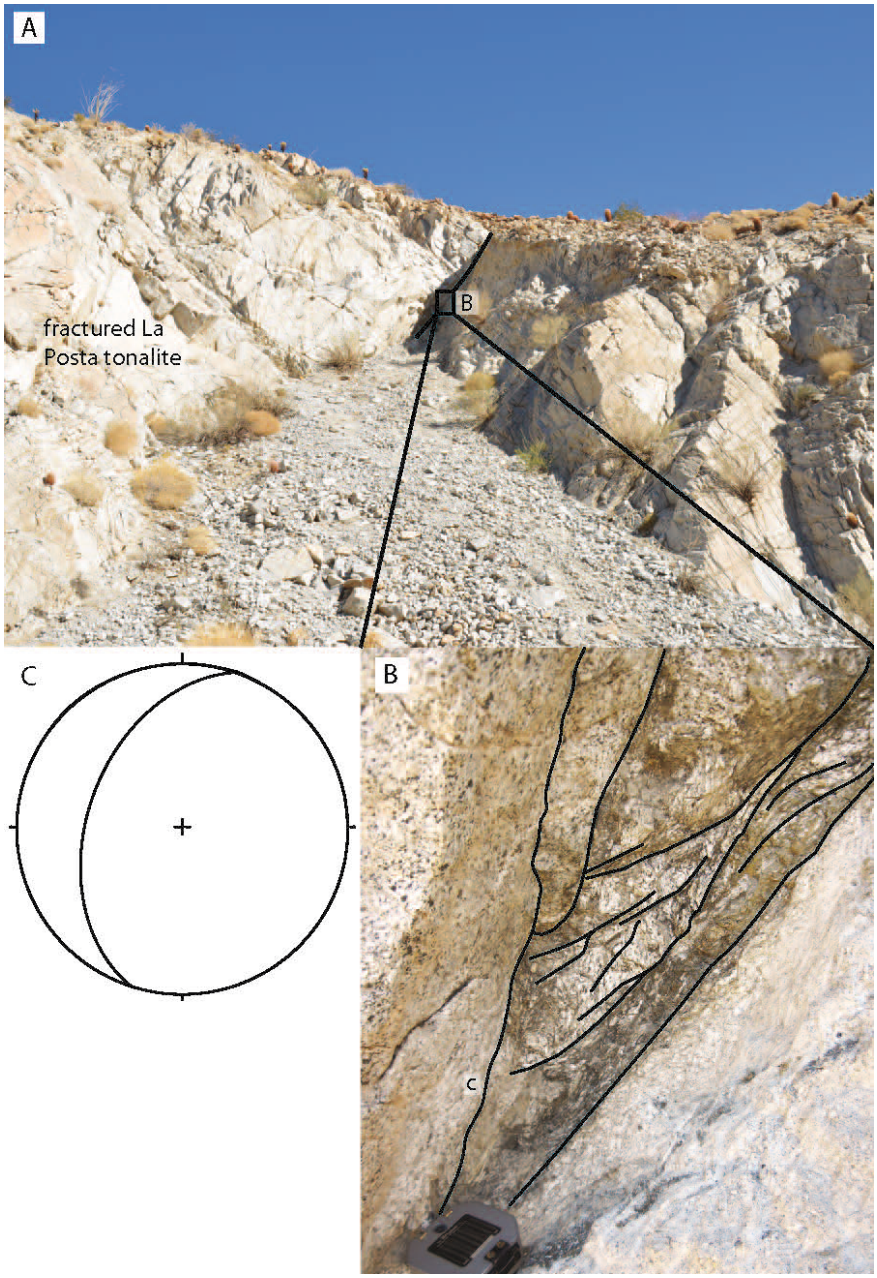

FIGURE 32 A fault from Site 12. A—A dip-slip fault in fractured La Posta tonalite. B—Close up of fault pictured in A. A mesh of crushed protolith and interwoven chlorite veins compose the core of this fault. The footwall (right of the chlorite veins) of the fault is damaged while the hanging wall (left of chlorite veins) is seemingly unaffected. Brunton for scale. C—The fault strikes north-northeast and dips to the west. No slip indicators were observed.

tures along the mountain front to the north and northwest (Compare Figure 33 and 16). At the mesoscale, the rock is unaltered and grain sizes are large (1-6 mm), and we consider the protolith here as the most pristine tonalite within the Tierra Blanca Mountains.

I inventoried the density of fractures and faults associated with deformation in the region with three scanlines (Table 7) which were from the northeastern side of the mountains; the distance between the northern and southernmost lines is ~ 3.6 km. One line was collected north of the park in Marsh Canyon (Figure 34), a second in Moonlight Canyon (Figure 35), and a third along the Coyote Mountain segment in Coyote Canyon (Figure 36). Fracture densities in Table 7 were calculated from Savage and Brodsky's (2011) equation, which is the number of fractures per meter. The faults and fractures in scanline 1 have several orientations, but three orientation groups could be distinguished: northeast-striking southeast-dipping fractures, north-striking west-dipping fractures, and north-striking east-dipping fractures (Table 8). Lineations at the outcrop were approximately horizontal (Figure 21B).

Scanline 2 was taken in Moonlight Canyon, ~ 0.5 km south of the county park (Figure 35). The orientations of fractures and faults encountered in this scanline are very similar, almost entirely north-northwest-striking and east-northeast-dipping (Table 8). The scanline is along a northeast-striking strike-slip fault. Data collected along scanline 3 show two groups of faults and fractures with one striking northwest and dipping steeply southwest and the second group striking northeast and dipping southeast (Table 8; Figure 36). The scanline is ~ 36 m northeast from the fault located at 567611 m E 3644945 m N and ~ 215 m southwest of the mountain front.

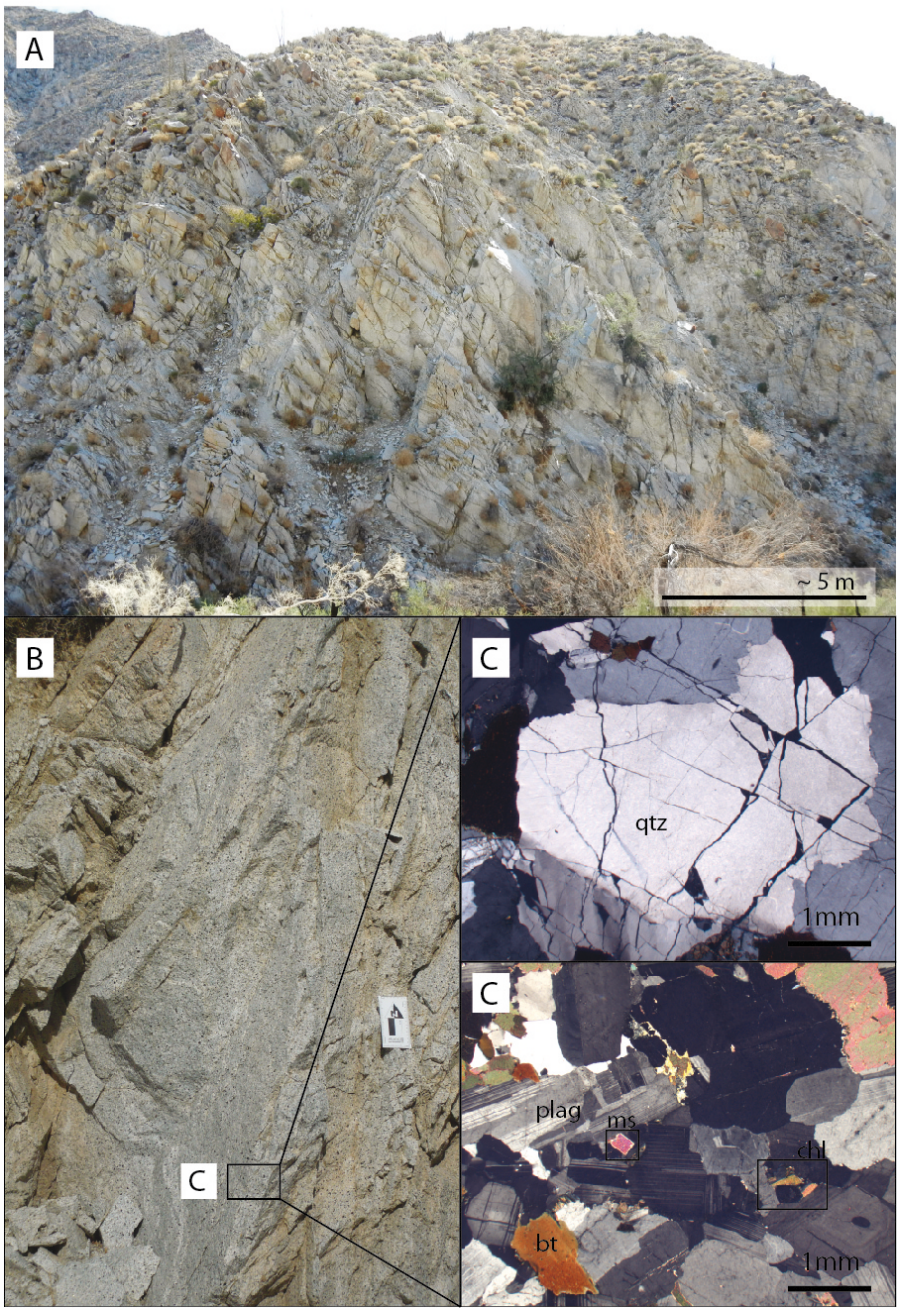

FIGURE 33 Pictures and a thin section (xpl 10x) from Canebrake Canyon, in the southeastern part of the Tierra Blanca Mountains at Site 13. A—The canyon is composed of fractured Cretaceous La Posta tonalite pluton. The fractures have a lower density than fractures along the mountain front to the north and northwest. B—The rock is unaltered and grain sizes are large (1-6 mm). C—In thin section, quartz grains are commonly fractured, but there is very little alteration. There are occasional biotite plates altering to chlorite, hornblende fragments, and an occasional, very small muscovite flake. Plagioclase crystals are zoned and experience some fracturing and sericitization. This locality is 7 km southeast of Agua Caliente County Park.

Microscale Observations

The 38 thin sections analyzed provide a microscopic view of the undeformed La Posta pluton, damage zone rocks, fault-related rocks, fault surfaces, and altered protolith within the Tierra Blanca Mountains. I summarize key observations here, while detailed descriptions are provided in Appendix A. General features frequently observed in these samples include Berlin Blue chlorite pseudomorphing after biotite (Figure 37A), biotite entrainments (Figure 37B), sericitized plagioclase in altered regions (Figure 37C), intense fracturing within quartz and plagioclase (Figure 37D), precipitated calcite (Figure 37D, F), and zones of cataclasite (Figure 37E).

The La Posta tonalite within Canebrake Canyon (Figure 33) is the most pristine protolith in the study area and contains numerous large biotite sheets, twinned plagioclase, and quartz crystals. Plagioclase crystals often exhibit clear zonings, and quartz crystals are composed of subgrains. Scattered chlorite pseudomorphs biotite. Other minerals identified include minor amounts of allanite, muscovite, and epidote.

In the footwall of the West Salton detachment fault, ~ 37 m from the fault plane, the rock exhibits brittle deformation and is a foliated cataclasite with biotite stringers defines foliation. The biotite entrainments are in some cases connected to larger clusters of biotite (Figure 38). Thin sections from Moonlight Canyon along the detachment fault exhibit evidence of mineralization. A sample ~ 20 m from a mapped fault trace has no bleaching or staining and is foliated cataclasite. Another sample collected within 1.5 m of a fault in Moonlight Canyon in a stained and altered region exhibits cataclasite within cataclasite as transported and suspended grains indicate a previous cataclasis event (Figure 39A-B). Quartz grains are plastically deformed and have bulging grain boundaries

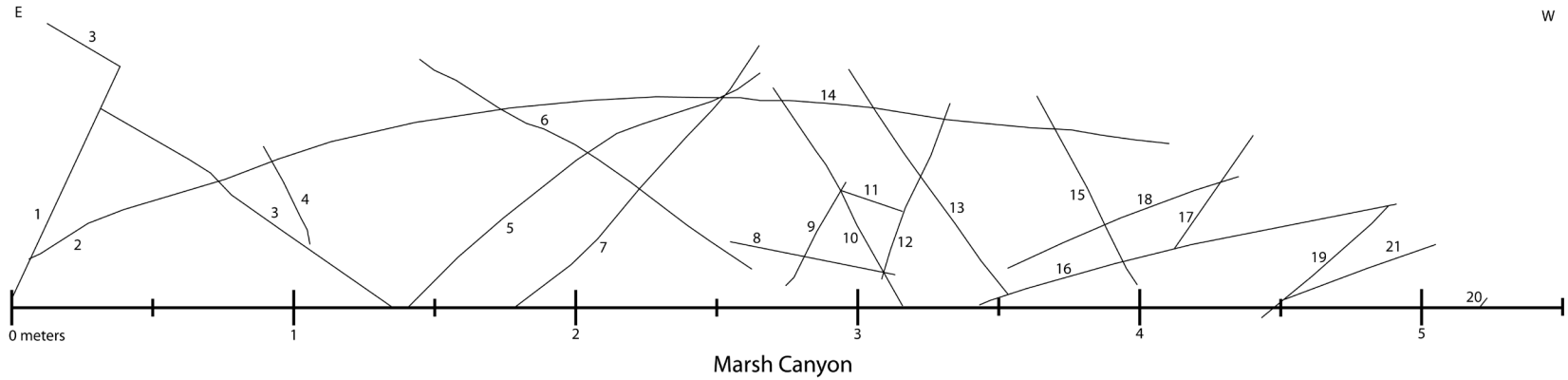

FIGURE 34 Scanline from an outcrop (564230 m E 3646419 m N) located along a strike-slip fault south of a segment of the West Salton detachment fault. Marsh Trail follows the canyon and provides the informal name Marsh Canyon. The outcrop is the fractured La Posta tonalite. Slip indicators on faults along the scanline indicate lateral dominated movement (Figure 20). Fractures encountered in the scanline have multiple orientations (Table 8). Most strike northeast and dip southeast. Two fractures were north-south striking and east dipping. The remaining fractures measured have orientations ranging from northeast-striking west-dipping to east-west-striking south-dipping.

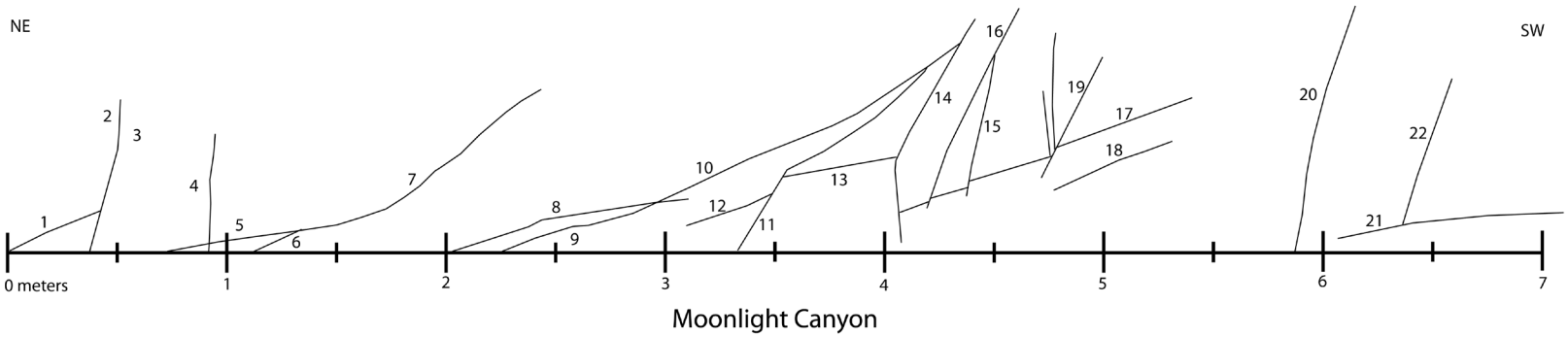

FIGURE 35 Scanline in an outcrop in Moonlight Canyon located at 565423 m E 3645312 m N along a small fault that intersects the West Salton detachment fault ~ 0.5 km to the southwest and a small oblique fault striking northwest-southeast ~ 0.3 km to the northeast. The outcrop is completely stained red-orange and is faulted and fractured. Slickenlines are visible on most of the smooth surfaces and orientations range from horizontal to vertical, but most are nearly horizontal (Figure 25). The fractures strike consistently northwest-southeast and dip northeast though the dip angles vary from 24° to vertical (Table 8).

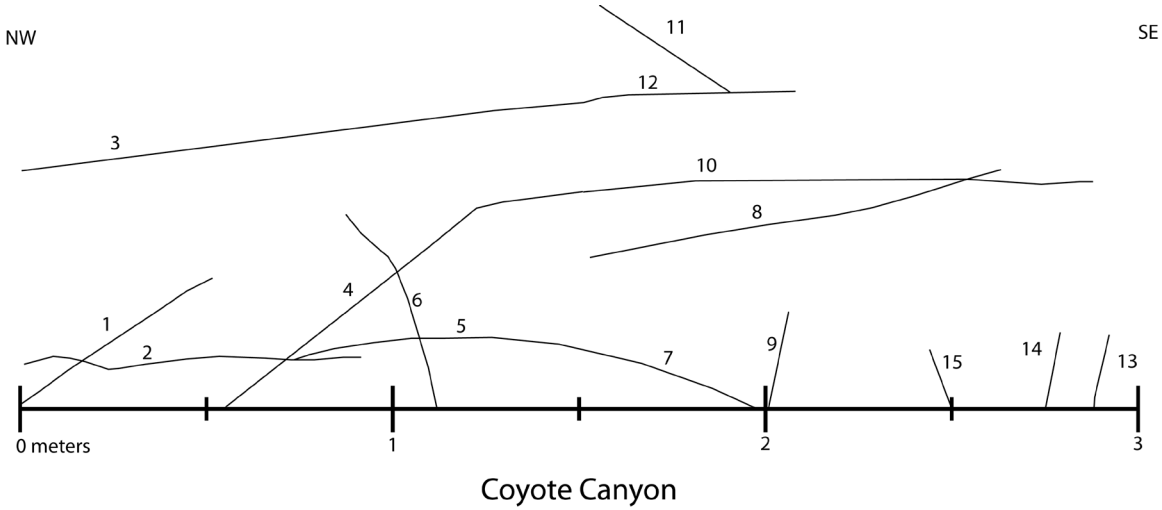

FIGURE 36 Scanline in an outcrop in a canyon informally called Coyote Canyon at 567630 m E 3644979 m N. This scanline is entirely within the Coyote Mountain segment damage zone. The fractures strike consistently northeast-southwest and dip ~ 55° southeast though some fractures strike northwest-southeast and dip steeply southwest. A few fractures strike almost east-west and dip ~ 60° to the south (Table 8).

suggesting high temperature, ~ 280-400°C (Figure 39C-D; Stipp et al., 2002). The grains that survived cataclasis are predominately quartz and some plagioclase (Figure 39E). The angular fragments look like they may have flowed within the stained matrix (Figure 39F).

One of the most interesting microstructures is from a fault that is parallel to, and ~ 240 m southwest of, the Coyote Mountain segment of the Elsinore fault in the informally named Coyote Canyon at Site 9. Examination of the fault surface in thin section reveals fractured quartz and plagioclase crystals infilled with precipitated calcite (Figure 37E) and a steady increase in grain size from the amorphous gouge along the slip surface to comminuted fault rocks (Figure 40). The clasts along the fault zone in Figure 40 are restricted to single minerals as opposed to cataclasite along the detachment fault to the north, where the clasts are clusters of minerals (Figure 39). One fractured quartz crystal in the fault surface dilated ~ 3.1 mm in length and 1.4 mm in width. Fractures in this section are 30-230 μm wide. Thin sections show partial chloritization of scattered biotite crystals, though there is not as much chlorite present here as in other areas in the mountains. Biotite crystals are frequently aligned into veins, sometimes bordering channels of calcite. The calcite is very fine grained and fills voids around and within the host rock grains. Quartz and plagioclase grains have variable sizes, and many grains have been comminuted to 0.02-1 mm. The gouge is fine-grained calcite precipitated around the comminuted wall rock composed of quartz, plagioclase, and biotite pieces. Some of the

TABLE 7 A summary of scanline data

Scanline	Length (m)	Fracture Density (fx/m)	Location	Distance and direction from park
1	5.5	3.82	Marsh Canyon	~ 1 km northwest
2	7	3.14	Moonlight Canyon	~ 0.5 km south
3	3	5	Coyote Canyon	~ 2.5 km southeast

TABLE 8 Scanline data for the three scanlines in the Tierra Blanca Mountains

Marsh Canyon Scanline			
Plane	Strike	Dip	Direction
1	60	84	SE
2	78	68	SE
3	165	40	SW
4	178	72	W
5	25	31	SE
6	160	60	SW
7	32	61	SE
8	146	47	SW
9	40	56	SE
10	2	68	SW
11	137	60	SW
12	40	68	E
13	0	74	E
14	105	39	S
15	170	74	SW
16	67	71	SE
17	45	65	SE
18	75	54	SE
19	43	45	SE
20	40	66	SE
21	85	36	S
0 meters: 32.9541992, -116.3127908			
5 meters: 32.9541994, -116.3128658			

Moonlight Canyon Scanline			
Plane	Strike	Dip	Direction
1	350	51	E
2	290	78	N
3	322	85	NE
4	103	90	VERT
5	346	24	NE
6	315	30	NE
7	330	60	NE
8	20	35	E
9	355	49	E
10	351	46	E
11	310	68	NE
12	10	44	E
13	2	34	E
14	328	78	NE
15	332	90	VERT
16	305	66	NE
17	0	39	E
18	0	35	E
19	340	75	NE
20	345	60	NE
21	324	32	NE
22	322	76	NE
0 meters: 32.9441522, -116.3001061			
7 meters: 32.9441256, -116.3001492			

Coyote Canyon Scanline			
Plane	Strike	Dip	Direction
1	17	34	SE
2	36	53	SE
3	39	46	SE
4	8	52	E
5	37	56	SE
6	148	77	SW
7	60	60	SE
8	30	54	SE
9	138	85	S
10	34	53	E
11	80	56	S
12	30	55	SE
13	150	84	SW
14	85	62	S
15	130	83	SW
0 meters: 32.9410053, -116.2765219			
3 meters: 32.9409961, -116.2765111			

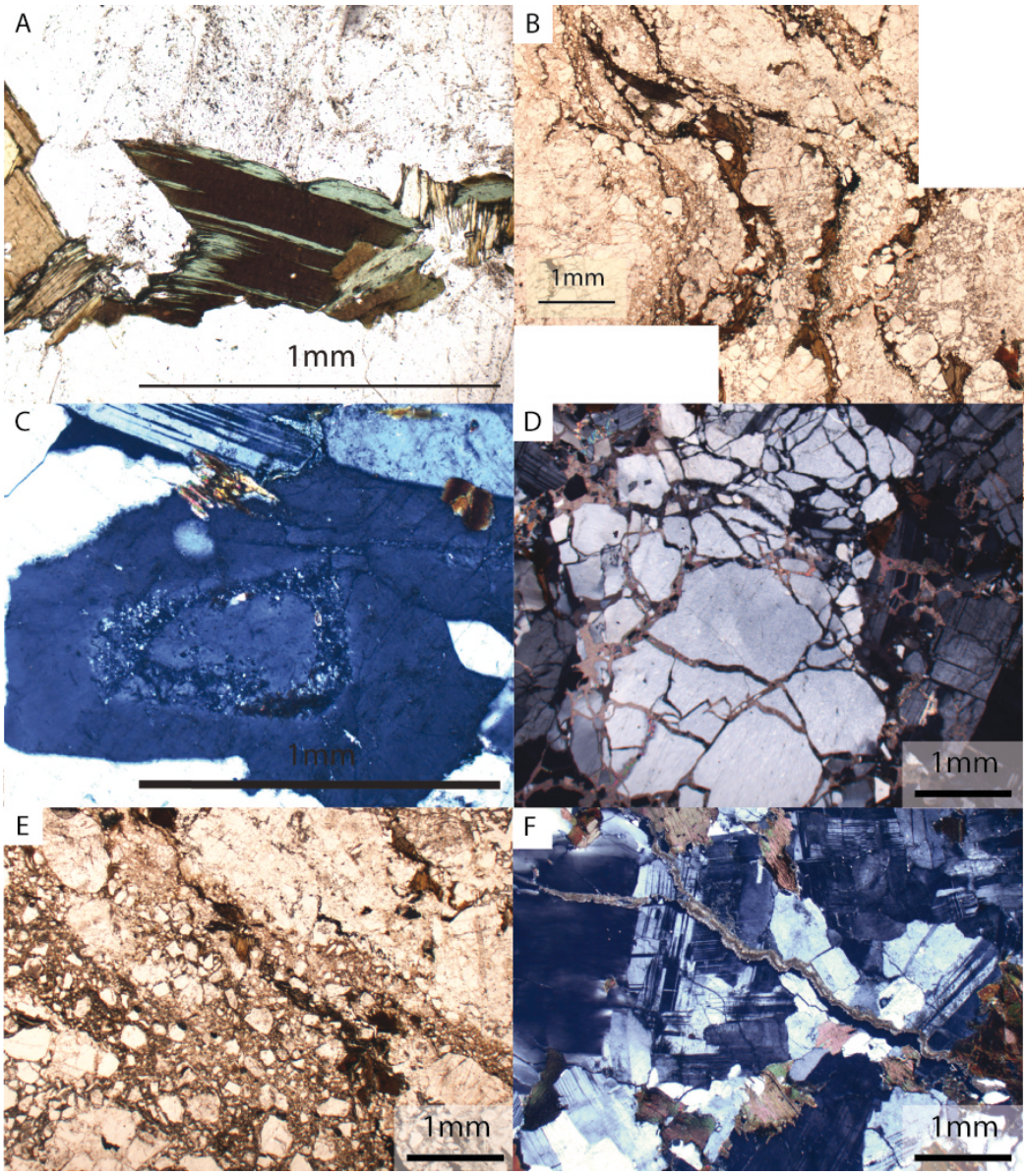

FIGURE 37 A—Chlorite pseudomorphing biotite (10x PPL). B—Biotite shear bands (2.5x PPL). C—Sericitized plagioclase (10x XPL). D—Fractured quartz crystal with calcite fill (2.5x XPL). E—Cataclasite (2.5x XPL). F—Precipitated calcite (2.5x XPL).

biotite is sheared parallel to the fault surface. Most of the fractures in quartz and plagioclase crystals are infilled with calcite.

Thin sections from the stained regions of the study area exhibit red fine-grained groundmass encompassing angular fragments of plagioclase and quartz (Figure 39). No

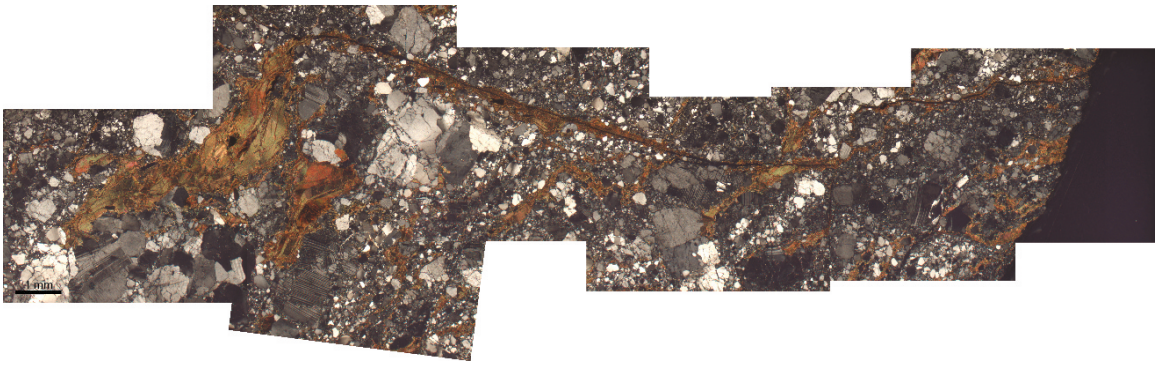

FIGURE 38 Sample 10a from 564841 m E 3645903 m N contains an entrained biotite within the West Salton detachment fault zone.

biotite or hornblende appears to have survived the events that caused the cataclasis and staining. The angular fragments greatly range in size, and zones are not segregated by grain size like in other unstained locations (e.g. Figure 40). Full descriptions of thin sections are recorded in Appendix C.

FLUID CHEMISTRY

In this section I present results from chemical and isotopic analyses of the water from the spring box at Agua Caliente County Park. These data include pH, alkalinity, stable isotope measurements ($\delta^{13}C$ of dissolved inorganic carbon, and δD and $\delta^{18}O$ of water), spring water temperature, conductivity, water level, and major elemental concentrations. I recorded temperature, water level, and conductivity measurements using the Levelogger data logger. Elemental data (Table 5) were used to calculate geothermometry ranges for the fluids. All of these data are integral in determining the potential source and alteration potential of the springs.

The pH of the county park spring in November 2011 was 9.55 using an Omega PHH-5012 Meter at 29.1°C. The county park measures pH sporadically, and typical val-

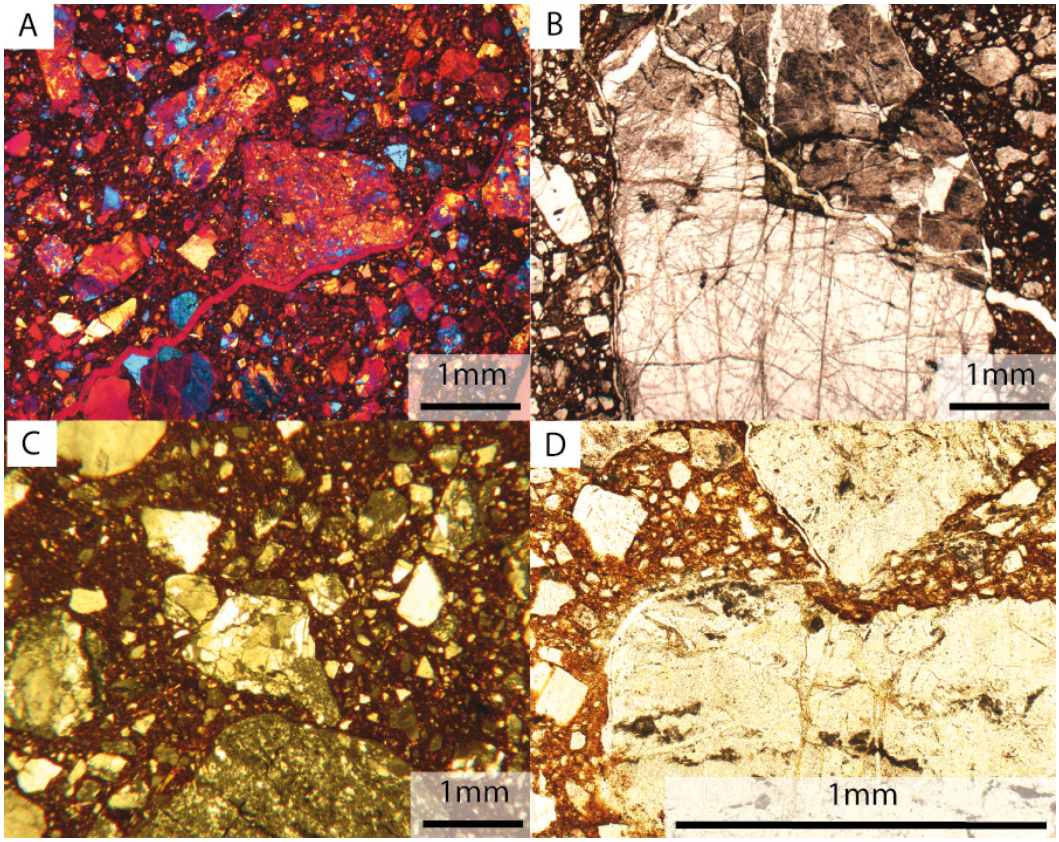

FIGURE 39 Thin section photos from sample 84 collected at 565115 m E 3644819 m N in Moonlight Canyon within in a meter of a fault. A—Cataclasis (XPL with gypsum plate, 2.5x). B—Fractured subgrained quartz within cataclasite (XPL with gypsum plate, 2.5x). C—Cataclasite containing clasts of altered and fractured quartz and plagioclase (XPL, 2.5x). D—Zoomed in view of cataclasite. Angular clasts of quartz and plagioclase are suspended within the stained matrix (PPL, 10x).

ues are in the 8-9 range (Mark Stockdale, personal communication). November's spring alkalinity was 180 mg/L $CaCO_3$, or 109.8 mg/L HCO_3. The fluids fall within the $NaHCO_3$ water type (Figure 41). Spring temperatures from logging during the summer range from 30.7-31.1°C. The maximum temperature values calculated using the N-K-Ca geother-mometer range from 75-86°C (see the previous section for the methods and Table 6 for input values).

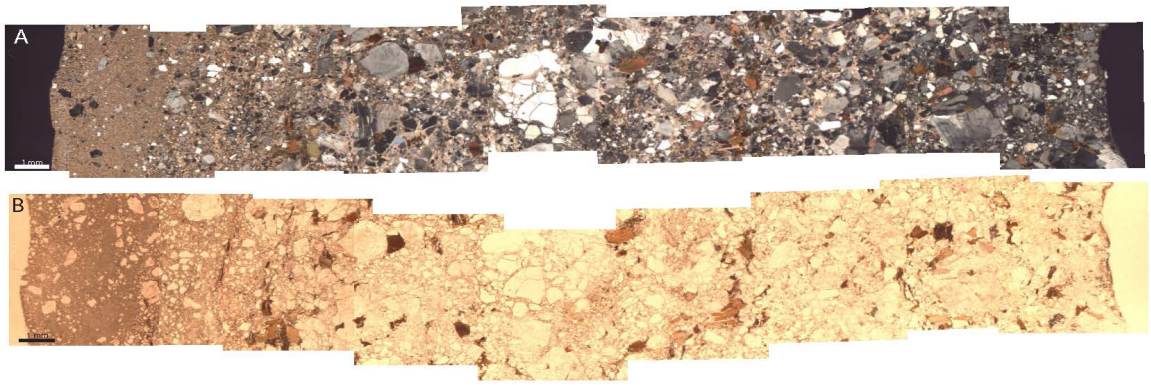

FIGURE 40 Cross sections of a subsidiary fault to the Coyote Mountain segment at Site 9 in Coyote Canyon. The left edge is the fault surface composed of fine-grained crystals and calcite. Grain sizes increase farther from the fault surface and calcite content decreases. A—XPL. B—PPL.

The $\delta^{13}C$ (PDB) value of the spring was -17.5‰ (Appendix B). The $\delta^{13}C$ values vary in many materials, but in this area, it is most likely from organically derived carbon in the soil (Figure 42; Brownlow, 1996). Two water samples collected in November 2011 were analyzed for δ18O values, and their values were -10.1 and -10.3 ± 0.2 ‰ (SMOW; Table 10). The δD values were -70 and -71 ‰. Comparisons of δD and $\delta^{18}O$ determine the type of source water (Figure 43; Sheppard, 1986). The water falls on the meteoric water line, which suggests the springs are sourced from precipitation.

Data recorded using the Levelogger are time series measurements of temperature, water level, and conductivity were taken every 15 minutes for a week (Figure 44) to several months (Figure 45). The logging periods are during the winter and summer to evaluate seasonal variations. Conductivity measured (Figure 45) over summer 2011 shows three discernible expressions, though as a whole, a daily signature is readily apparent which may be a result of tidal or atmospheric influences. In a period from June 9-July 10, conductivity is highly variable with rapid jumps between 379.8 µS/cm to 638.85 µS/

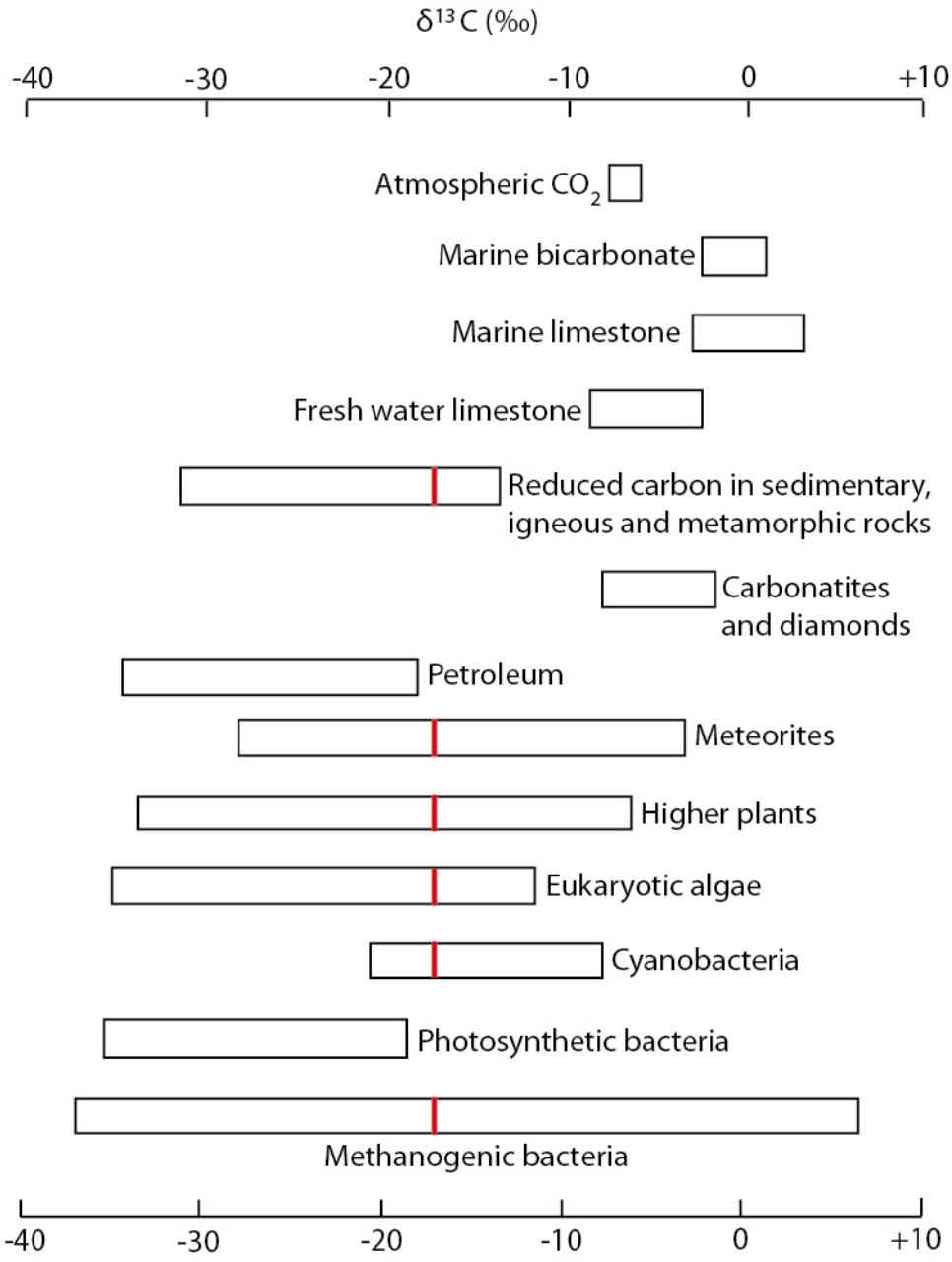

FIGURE 41 $\delta^{13}C$ (‰) (PDB) ranges for several sources modified from Brownlow (1996). The red line at -17.5‰ is the value from the spring sampled at Agua Caliente County Park. This value overlaps the reduced carbon in sedimentary, igneous, and metamorphic rocks, $\delta^{13}C$ found in meteorite, higher plants, eukaryotic algae, cyanobacteria, and methogenic bacteria. The most likely source for the $\delta^{13}C$ in the study area is CO_2 sourced from the soil and dissolved into the groundwater.

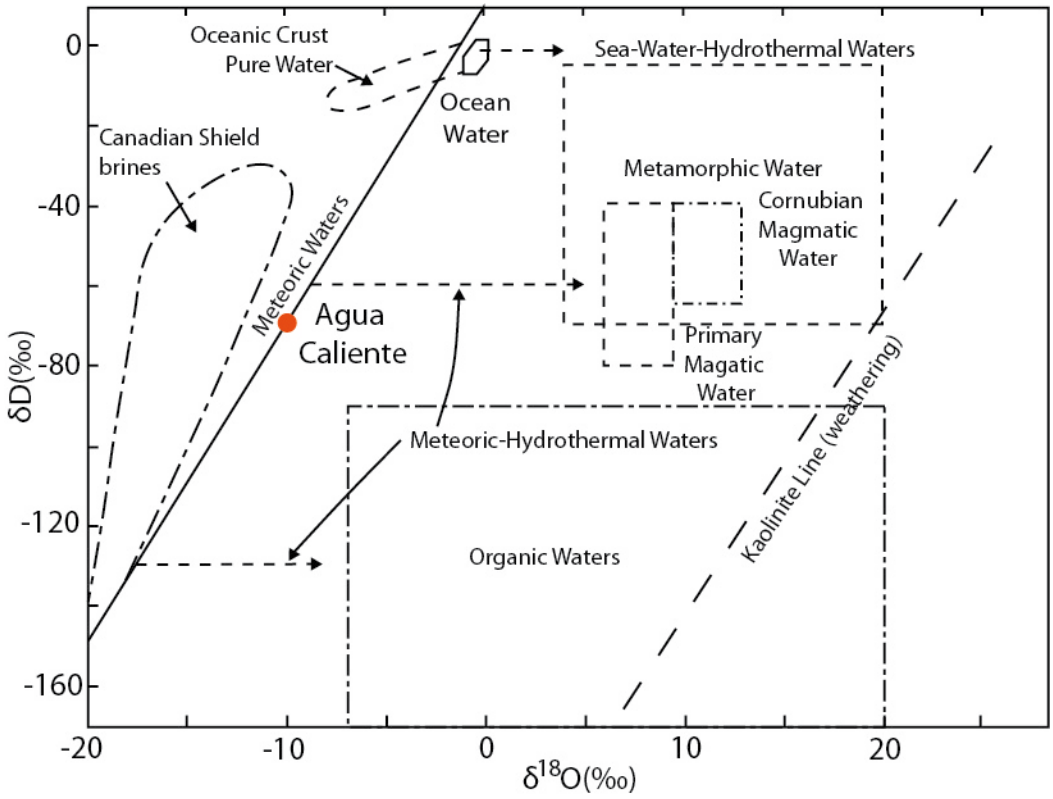

FIGURE 42 Water types based on δD and $\delta^{18}O$ trends. The isotopic value from the spring at Agua Caliente County Park is signified by the orange circle and label. The spring fluid plots directly on the meteoric water line. Figure modified from Sheppard, 1986.

cm. From July 10-August 1 there are 12 conductivity peaks and troughs that range from 479.15-677.18 µS/cm. The final period from August 1-22 exhibits small variations between the peaks and troughs between 591.67-658.01 µS/cm and diminishes to the end when the logger quit working. Over the June-August logging periods the general trend of the data is positive with periodic spikes. A rough measure of total dissolved solids from conductivity ranges from ~ 190-340 during the summer.

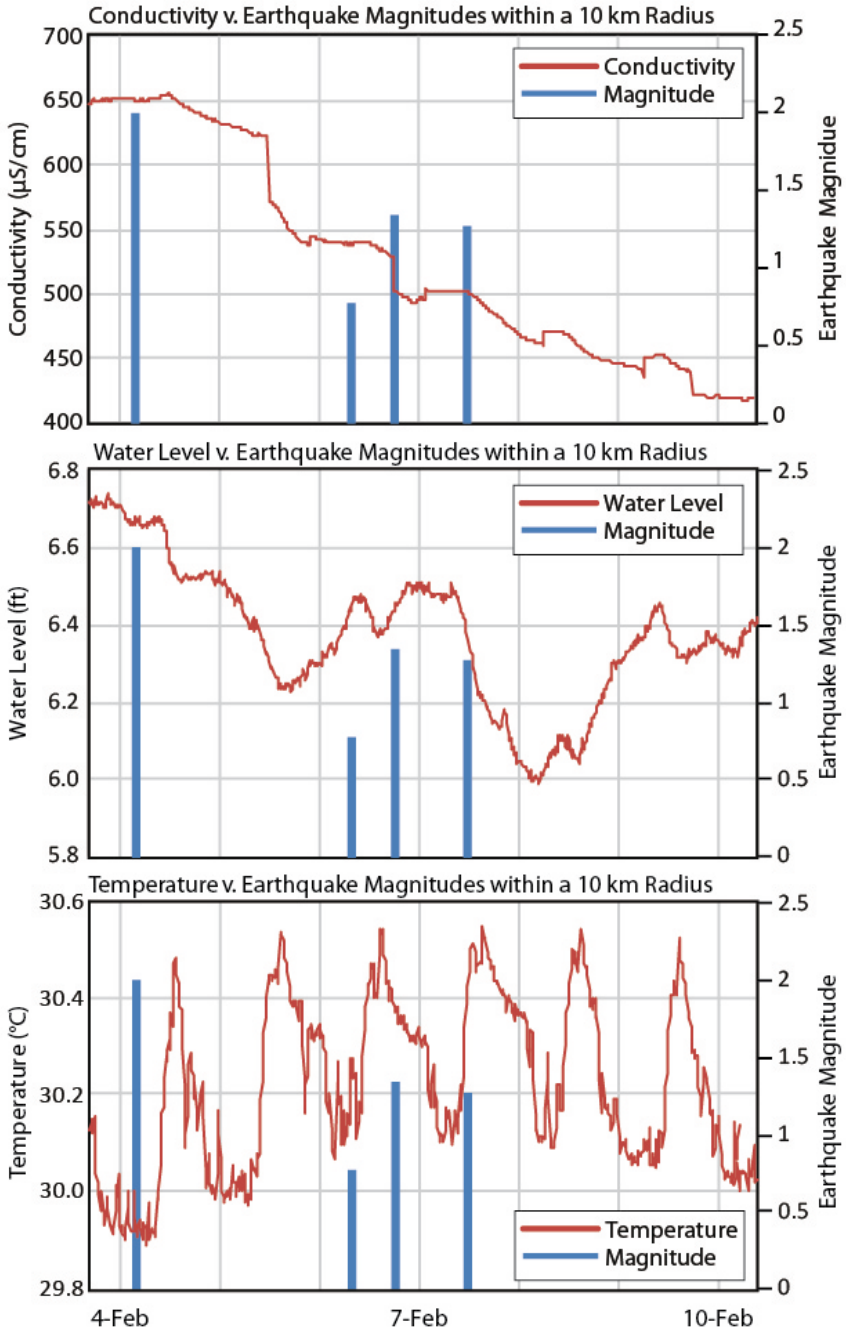

Figure 43 Magnitudes for four seismic events that occurred during February 3-10, 2011 during logging. Events are paired with conductivity, water level, and temperature.

Figure 44 (following pages) In order, spring temperature, water level, conductivity, barometric pressure, air temperature, Vallecito Valley earthquake magnitudes, and Carrizo Valley earthquake magnitudes within 10 km of the spring box during June 9-August 22, 2011.

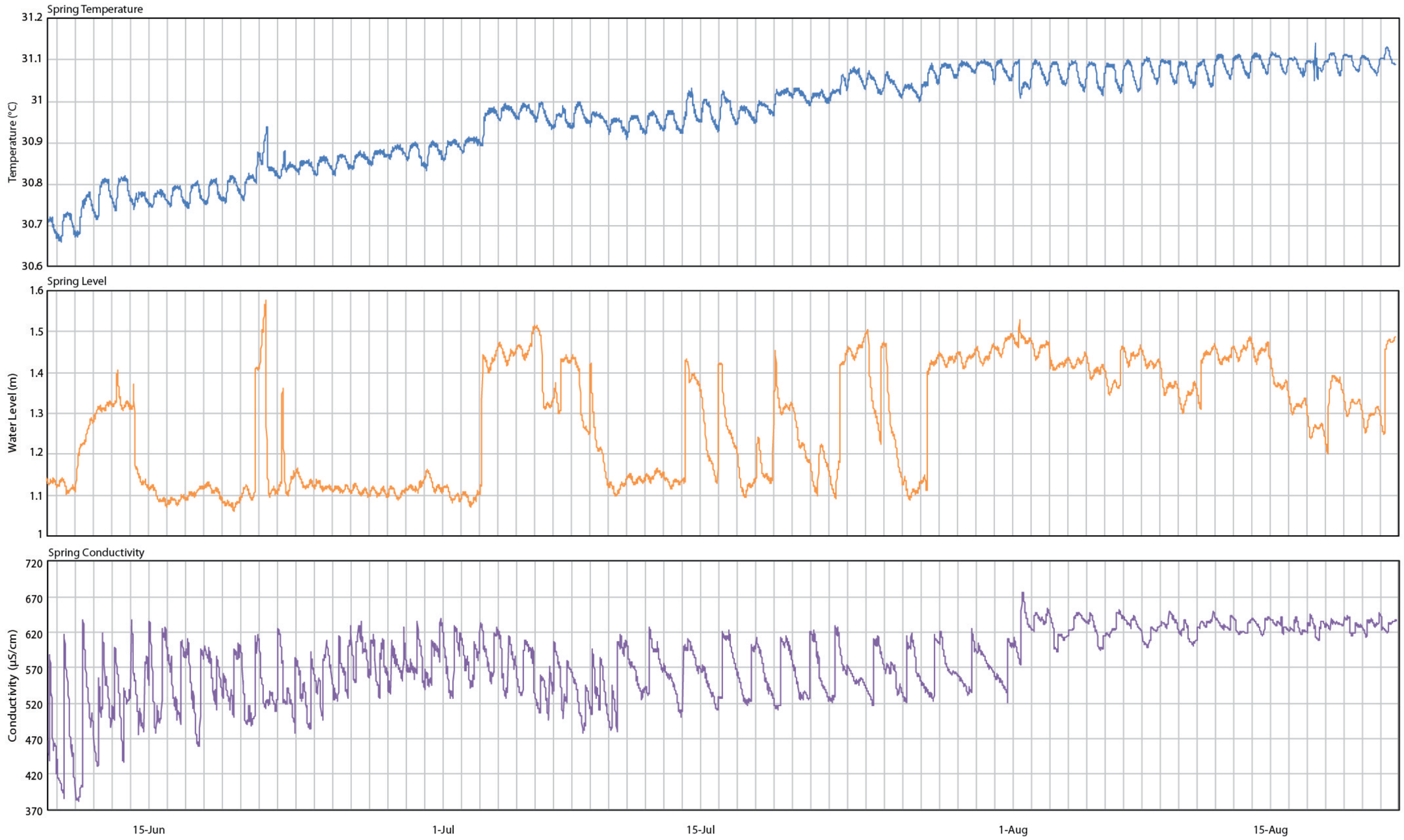
Spring Temperature
Temperature (°C)
31.2
31.1
31
30.9
30.8
30.7
30.6
Spring Level
Water Level (m)
1.6
1.5
1.4
1.3
1.2
1.1
1
Spring Conductivity
Conductivity (µS/cm)
720
670
620
570
520
470
420
370
15-Jun
1-Jul
15-Jul
1-Aug
15-Aug

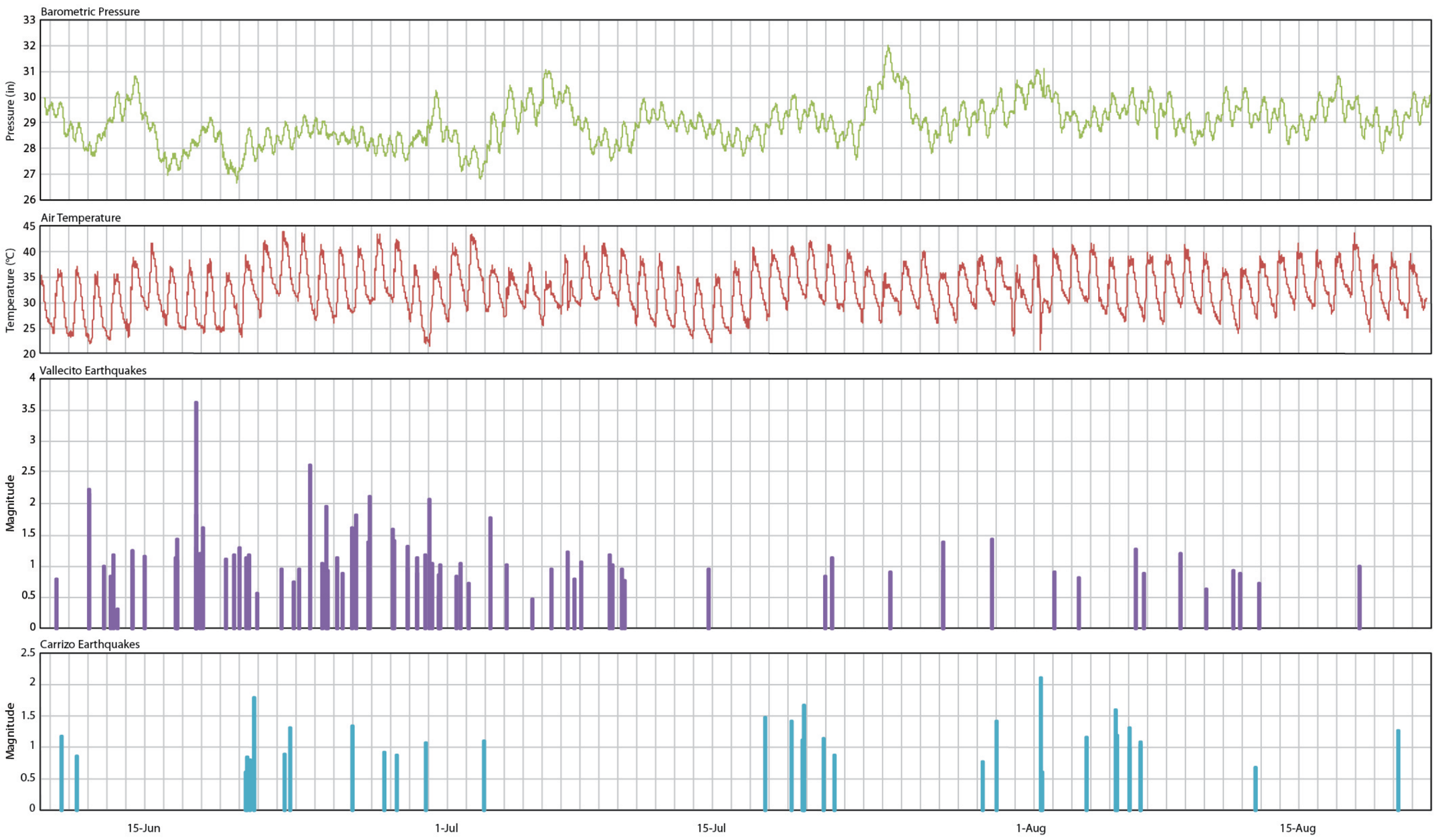
Barometric Pressure
Pressure (in)
33
32
31
30
29
28
27
26
Air Temperature
Temperature (°C)
45
40
35
30
25
20
Vallecito Earthquakes
Magnitude
4
3.5
3
2.5
2
1.5
1
0.5
0
Carrizo Earthquakes
Magnitude
2.5
2
1.5
1
0.5
0
15-Jun
1-Jul
15-Jul
1-Aug
15-Aug

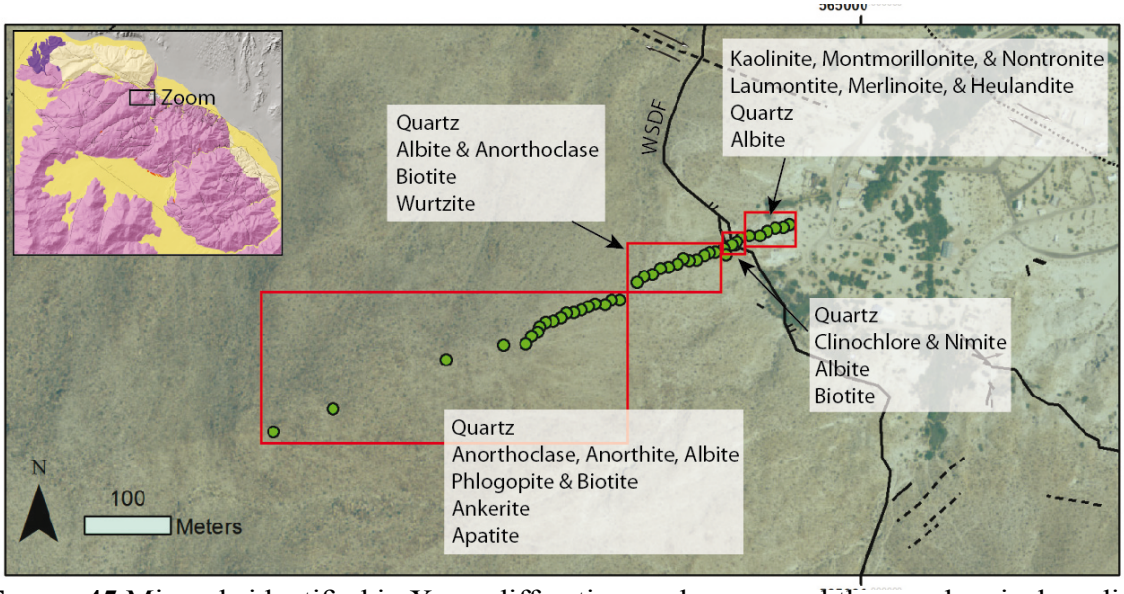

FIGURE 45 Minerals identified in X-ray diffraction analyses reveal the geochemical gradient from the heavily altered fault rocks at the valley floor into the unaltered protolith of the Tierra Blanca Mountains. The altered zones in the hanging wall of the detachment fault are rich in kaolinte and related clay minerals with quartz and albite remants. In hand sample, biotite flakes are still identifiable. The fault plane is predominately the minerals contained within the tonalite but with a heavy concentration of chlorite. Farther into the mountain the lithology fades into consistent signatures of quartz, albite, and biotite with occasional other minerals. This composition is consistent throughout the range.

LOCAL SEISMICITY

Local seismic events (mostly < M_w 3.0) occurring during logging of spring temperature, level, and conductivity are plotted with the logger data presented in Figure 45, and all are recorded in Appendix E. Four earthquakes occurred within 10 km of the spring box while the Levelogger logged in February 3-10, 2011 (Figure 47). Their magnitudes ranged from M_w 0.79-2.02 and depths were 6.4-10.7 km. Two of the events occurred northwest of the spring at the southwest base of the Vallecito Mountains, and the remaining two occurred southeast of the Tierra Blanca Mountains. The first seismic event (M_w 2.02) preceded a 0.58°C water temperature jump that fits with daily patterns. The next three events clustered within 28 hours and do not appear to cause perceptible anomalies

in temperature, water level, or conductivity signatures during this logging interval. The water level trace is the most erratic of the three properties as it does not follow a diurnal cycle. Conductivity and water temperature generally display a consistent rise and fall within the 24-hour period. During spring logging from June 9-August 22, 2011, eight earthquakes occurred within a 5 km radius of the spring box (Figure 48) and 126 events occurred within 10 km radius (Figure 49). The wider radius reveals two clusters of seismicity in the northern Vallecito Valley and the southwestern Carrizo Badlands near the small community of Canebrake (Figure 10). A polygon of earthquakes along the Elsinore fault zone during the summer period of logging in Figure 50 shows a nearly vertical alignment of hypocenters. Coordinates for the polygon were 1: 32.696, -116.28; 2: 33.57, -117.4; 3: 33.618, -117.007; 4: 32.696, -115.789.

Eighty-two earthquakes occurred within 10 km of the spring box during period one, 24 events occurred during period two, and 20 occurred during period three. Water level fluctuations from June 9-July 3 average 1.14 m deep with a 20 cm dip on June 14 (Figure 45). Since June 9 to the time of the dip, seven small events occurred in the Vallecito region north of the county park, and two earthquakes took place during the sharp fall in water level. On July 3 the level rapidly jumps to 1.43 m and remains above 1.40 m until July 6 and levels return to ~ 1.10 m by July 10. Levels sporadically jump until July 27 and then levels rapidly rise above 1.40 m and remain high throughout the logging period and average 1.47 m. On July 3 an M_w 1.77 earthquake appears to correspond with the rapid jump in water level from 1.09-1.43 m though the rise in fluid levels slightly precedes the seismic event. Diurnal temperatures exhibit a steady increase as the summer progresses with a couple of uncharacteristic events (Figure 45). From July 27-August 22

the average temperature is 31.08°C. A temperature jump on July 3 corresponds with the observed jump in water level. Water levels do not exhibit cyclicity like conductivity and temperature.

I defined conductivity cycle length as the amount of time between peaks and troughs, and the data vary throughout the logging period. In June the cycles from peak to trough were ~ 18-19 hours and the rise from trough to peak took anywhere from 45 minutes to just over 6 hours. In mid July peak to trough times ranged from 28 hours 30 minutes to 41 hours 45 minutes with trough to peak rises from 8 hours 45 minutes to 10 hours 15 minutes. In early August peak to trough cycles ranged from 28 hours to 46 hours 15 minutes, and trough to peak times were 23 hours 45 minutes to 29 hours 30 minutes. Generally the rise from trough to peak is much shorter than the peak to trough descent. Conductivity peaks do not mimic daily temperatures as the peaks occur at any time of the day or night. Agua Caliente County Park does not change pumping schedules or water use during the summer months.

Protolith Alteration and Distribution

The La Posta pluton exhibits color variations that are most easily seen in aerial photographs, satellite imagery, or in the field from afar (Figure 14). In aerial photography, the protolith on the western portion of the mountains is reddish-buff while the eastern side is lighter tan to off-white. On the Landsat image (Figure 3), the transition between the darker west side and the lighter east side of the mountains is fairly abrupt. In the field, this color change is noticeable from the valley floor. The damaged areas along the faults and along the flank of the mountains are light colored while farther into the mountains,

the tonalite is dark red and brown.

The damage zone west of the concealed main trace of the Coyote Mountain segment on the northeastern flank of the mountains is bleached from pink-buff to white and intensely fractured. Fracture orientations range widely, but the dominant strike is roughly parallel with the mountain front. The damage zone directly west of the park is a foliated, intact plane that is not encompassed by bleached protolith unlike the damage zone to the south (Figure 18). The two predominant alteration types observed in the protolith composing the Tierra Blanca Mountains are the white bleaching and the red-orange staining. Bleaching is the dominant style of alteration at the county park though linear red-orange stains aligned approximately east-west form wide (up to 2 m) bands and streaks through the bleached zone (Figure 5). The most intense staining found in the mountain range is in Moonlight Canyon (Figure 26). Red staining is almost always adjacent to faults, but in some areas, for example, halfway through Bighorn Canyon, there are no mapped faults by the staining, but they may simply be concealed or eroded. Based on the observed alteration patterns, the protolith experienced significant grain size reduction and argillic alteration prior to iron staining associated with propylitic alteration, which may have been the cause of heated fluids circulating the fault damage zone during or after fault slip.

Generally, the transition from fault damage zones to the protolith is gradual. Damage zones are composed of bleached chalky protolith, comminuted grains (especially biotite and hornblende), red-orange iron staining, anastomosing chlorite veins, and an abundance of closely spaced fractures. Fracture intensities are highest adjacent to the fault cores, and intensity decreases toward the protolith.

I differentiated three mineral assemblages from the minerals proposed from X-ray

diffraction results (Table 9). Assemblage 1 includes minerals within the unaltered La Posta protolith, predominately albite, biotite, and quartz, with rare hornblende crystals identified in thin sections. The inner portion of the Tierra Blanca Mountains is composed chiefly of assemblage 1. Mineral assemblage 2 comprises minerals from the bleached regions around Agua Caliente County Park. This assemblage contains kaolinite, montmorillonite, zeolites (e.g. merlinoite), laumontite, heulandite, nontronite, nimite and clinochlore (chlorites), and fluorannite. The third assemblage is from the stained regions and is composed of saponite, zeolites, ankerite, ferrocolumbite, nontronite, and clinochlore in addition to quartz, Ca-albite, and biotite remaining from the tonalite protolith.

Twenty-seven samples collected during February 2011 were part of the geochemistry and mineralogy transect from the bleached protolith at the county park, up the mountain slope, and across the detachment fault plane (Figure 46). The samples in the hanging wall of the detachment fault and also within the bleached zone are composed of albite, anorthite, anorthoclase, biotite, clinochlore, fluorannite, kaolinite, laumontite, nimite, nontronite, orthoclase, and quartz based from minerals that satisfied peaks and scored 30 or higher in X'Pert Highscore (chalcopyrite, fraipontite, franklinite, heulandite, marcasite, montmorillonite, pitiglianoite, pyrochroite, zeolites scored lower than 30). The fault plane has quartz, albite, anorthoclase, (possibly marcasite and ferrierite as well). Samples from the footwall are composed of quartz, albite, biotite, anorthoclase, phlogopite, anorthite, microcline, and apatite (possibly wurtzite).

Two samples collected along the northwestern strand of the detachment were analyzed using X-ray diffraction and contain quartz, albite, stilbite, Fe-phlogopite, clinochlore, anorthoclase, laumontite, microcline, and zeolites. Minerals identified in thin

Table 9 XRD interpreted minerals

Sample	Minerals Possibly in Sample Determined Via X-Ray Diffraction (Italicized minerals scored below 30)
1-2	Ca-Albite, Kaolinite, *Anorthoclase*, Quartz, *Biotite*, *Pyrochroite*, *Montmorillonite*, *Pitiglianoite*
2-2	Quartz, Laumontite, Albite, *Zeolite*, *Nontronite*
3-2	Quartz, Ca-Albite, Anorthoclase, *Marcasite*, *Merlinoite*, *Heulandite*, *Anorthite*, *Zeolite*
4-2	Quartz, Ca-Albite, Anorthoclase, *Marcasite*, *K-Na-Al-Silicate*, *Anorthite*
5-2	Quartz, Ca-Albite, *Kaolinite*, Anorthoclase, Fluorannite, Anorthite, *Montmorillonite*, *Chalcopyrite*
6-2	Albite, Quartz, Laumontite, Orthoclase, Fe-Clinochlore
7-2	Quartz, Ca-Albite, *Fraipontite*, *Heulandite*
8-2	Quartz, Ca-Albite, Laumontite, Nimite, *Anorthoclase*, *Montmorillonite*, Clinochlore, *Franklinite*
9-2	Quartz, Ca-Albite, Anorthoclase, *Marcasite*, *Ferrierite*
10-2	Quartz, Ca-Albite, *Biotite*, *Na-Anorthite*
11-2	Quartz, Ca-Albite, *Biotite*, *Wurtzite*
12-2	Quartz, Ca-Albite, *Biotite*, *Wurtzite*
13-2	Quartz, Ca-Albite, *Biotite*, *Wurtzite*
14A-2	Quartz, Ca-Albite, *Biotite*
15-2	Quartz, Ca-Albite, *Biotite*, *Wurtzite*
16-2	Quartz, Ca-Albite, *Biotite*
17-2	Quartz, Ca-Albite, *Biotite*
18-2	Quartz, Ca-Albite, *Biotite*, *Wurtzite*
19-2	Quartz, Ca-Albite, *Biotite*
20	Quartz, Ca-Albite, *Biotite*
21	Quartz, Ca-Albite, *Biotite*, Anorthoclase
22	Quartz, Ca-Albite, *Biotite*, *Anorthoclase*
23	Quartz, Ca-Albite, *Biotite*
24	Quartz, Ca-Albite, *Biotite*, *Anorthoclase*
25	Ca-Albite, Quartz, Fe-Phlogopite, Na-Anorthite
26	Quartz, Ca-Albite, *Fe-Phlogopite*, *Ankerite*, Anorthoclase, Anorthite
36	Quartz, Ca-Albite, Biotite, *Microcline*, Strontium Apatite, *Anorthite*
43	Quartz, Ca-Albite, *Fe-Phlogopite*, *Saponite*, *Zeolites*
44	Ca-Albite, Quartz, *Ankerite*, Anorthoclase, Orthoclase, *Phlogopite*, Nontronite, *Ferrocolumbite*
46	Quartz, Ca-Albite, Clinochlore, *Ankerite*, *Biotite*, Anorthoclase, *Muscovite*
50	Albite, Quartz, Kaolinite, Clinochlore, *Montmorillonite*, *Illite*, *Biotite*, Ferripyrophyllite, *Sanidine*
58	Albite, Quartz, *Fe-Phlogopite*, Anorthoclase, Orthoclase, Na-Anorthite, *Biotite*
61	Ca-Albite, Quartz, *Fraipontite*, AlPO4, *Zeolite*, *Pitiglianoite*, Anorthite, Nontronite
62	Ca-Albite, Quartz, Anorthoclase, Biotite, Anorthite, *Phlogopite*
65	Quartz, Laumontite, Ca-Albite, *Aerinite*, *Anorthoclase*, Nontronite, Na-Al-S-Si Hydrate, *Pachnolite*
67	Quartz, Ca-Albite, Stilbite, *Fe-Phlogopite*, *Clinochlore*, *Anorthoclase*, *Laumontite*
69	Quartz, Ca-Albite, Laumontite, Microcline, Zeolite, Albite
77	Quartz, Ca-Albite, *Biotite*, Anorthoclase, Anorthite, *Zeolite*
78	Quartz, Ca-Albite, *Biotite*, Anorthoclase, *Merlinoite*, *Talc*, *Monofluorphosphate* Apatite, Anorthite
83	Quartz, Ca-Albite, *Phlogopite*, Anorthoclase, *Orthoclase*, Merlinoite, Biotite, *$AlPO_3$ Hydrate*, *Zeolite*
84	Quartz, Laumontite, *Heulandite*, Ca-Albite, *Zeolite*, *K-Ba-Al Silicate*

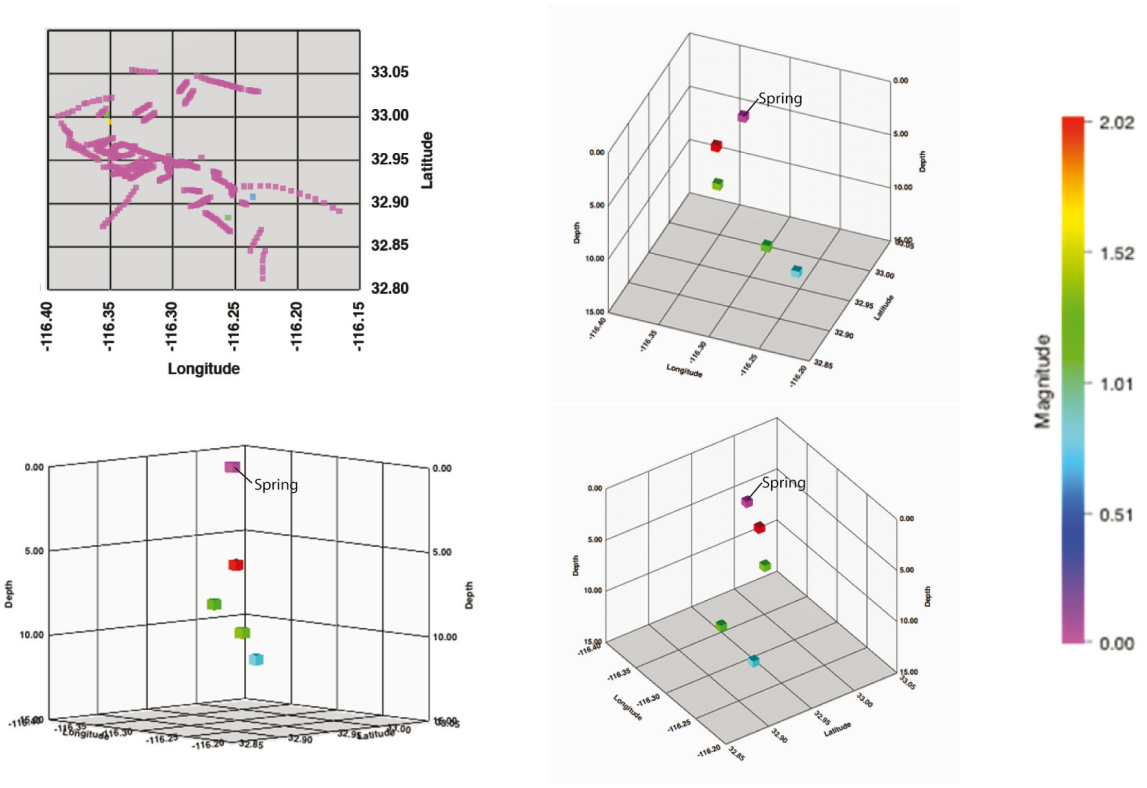

FIGURE 46 Earthquakes 10 km in radius from the spring box during February 3-10, 2011. The upper left image is a map view of faults depicted using pink markers.

section analysis include plagioclase, quartz, biotite, chlorite, epidote, allanite, calcite, sericite, muscovite, and hornblende (Appendix C). These findings are consistent with older mineralogical studies of the La Posta pluton (e.g. Todd, 1977; Clinkenbeard, 1987), and with water-rock alteration assemblages (Schwenzer and Kring, 2009).

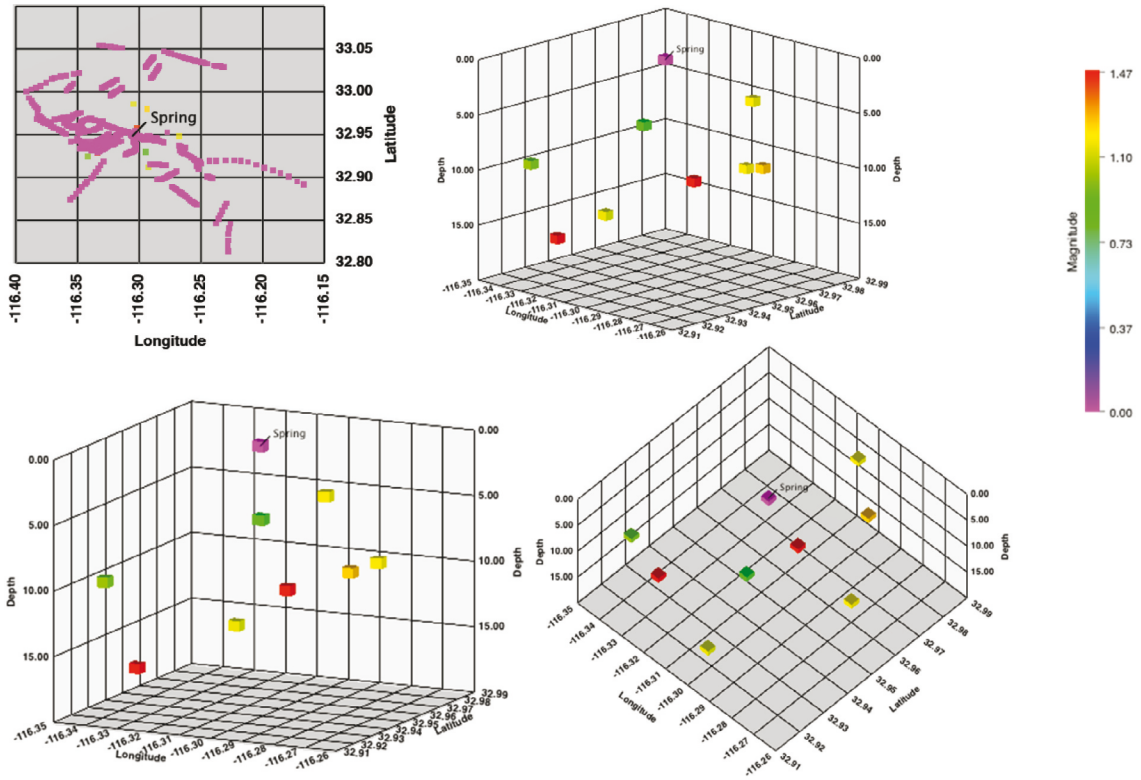

FIGURE 47 Earthquakes 5 km in radius from the spring box during June 9-August 22, 2011. The upper left image is a map view of faults depicted using pink markers.

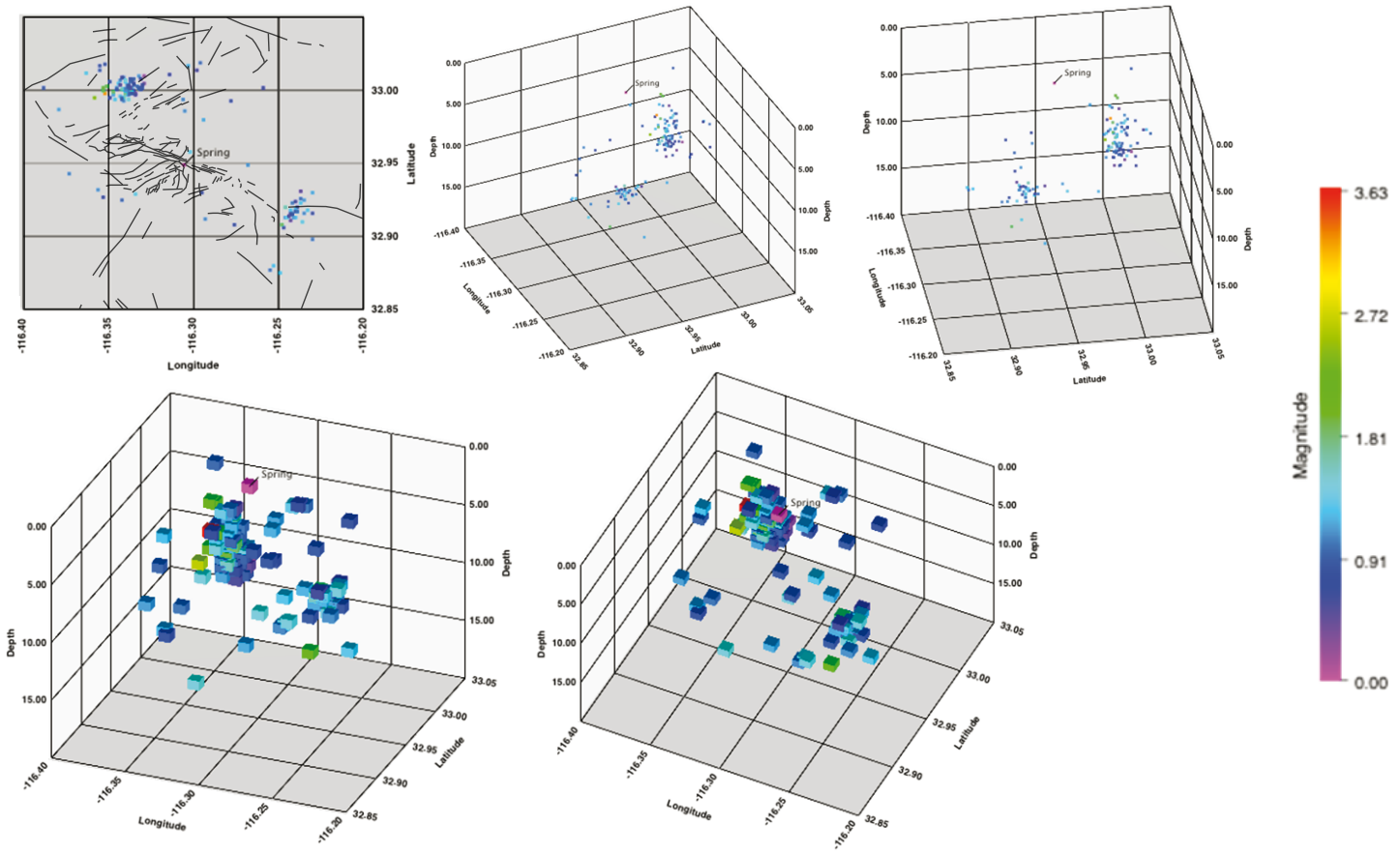

FIGURE 48 Earthquakes 10 km in radius from the spring box during June 9-August 22, 2011. The upper left image is a map view of faults depicted using pink markers.

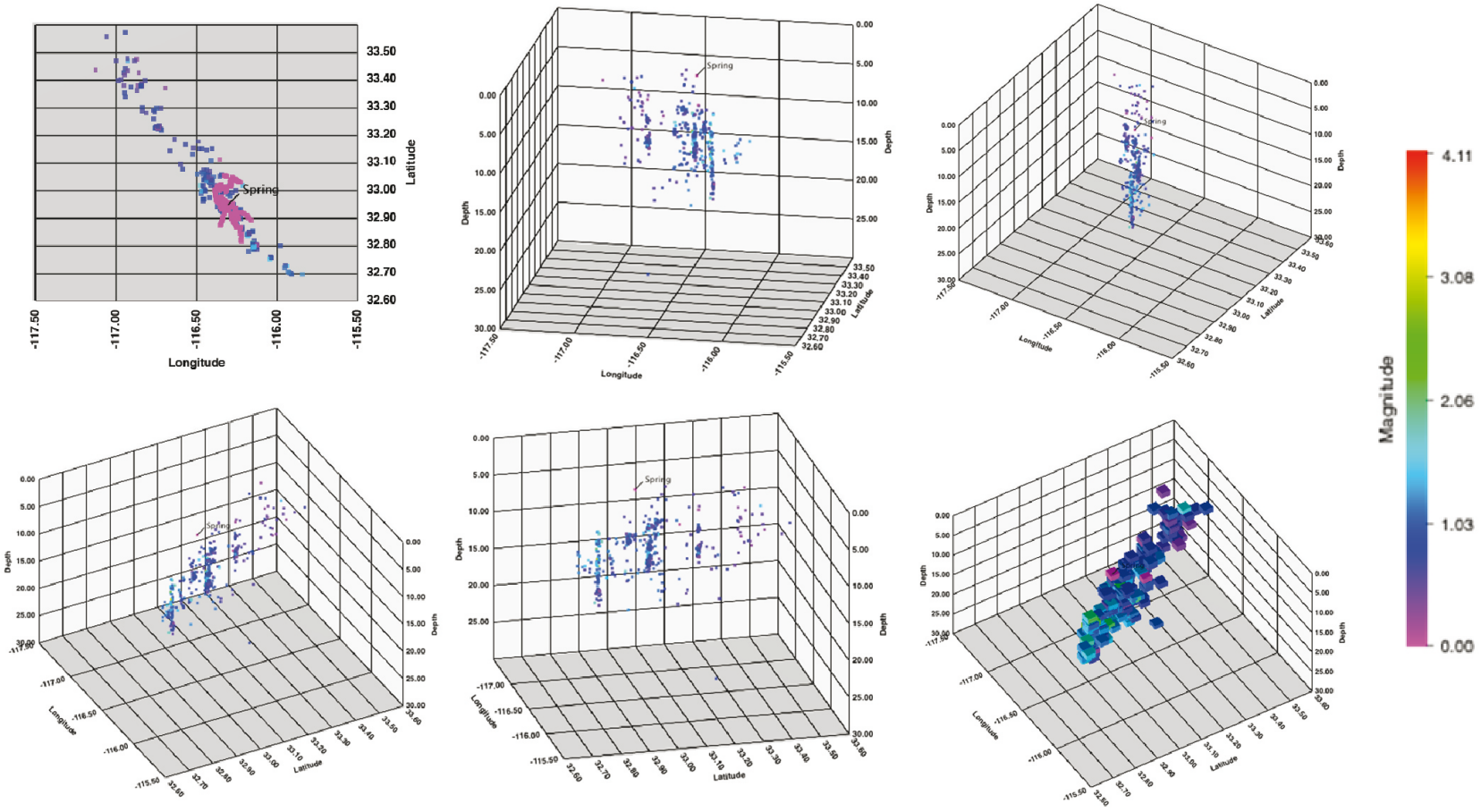

FIGURE 49 Two-dimensional and three-dimensional plots of seismic events within the polygon (32.696, -116.28; 33.57, -117.4; 33.618, -117.007; 32.696, -115.789) from June 9 to August 22, 2011. The spring box where the Levelogger LTC recorded data is labeled "spring." Seismic event magnitudes ranged from Mw 0.07-4.11. Depth is in kilometers. The pink data points are points along faults seen at the surface.

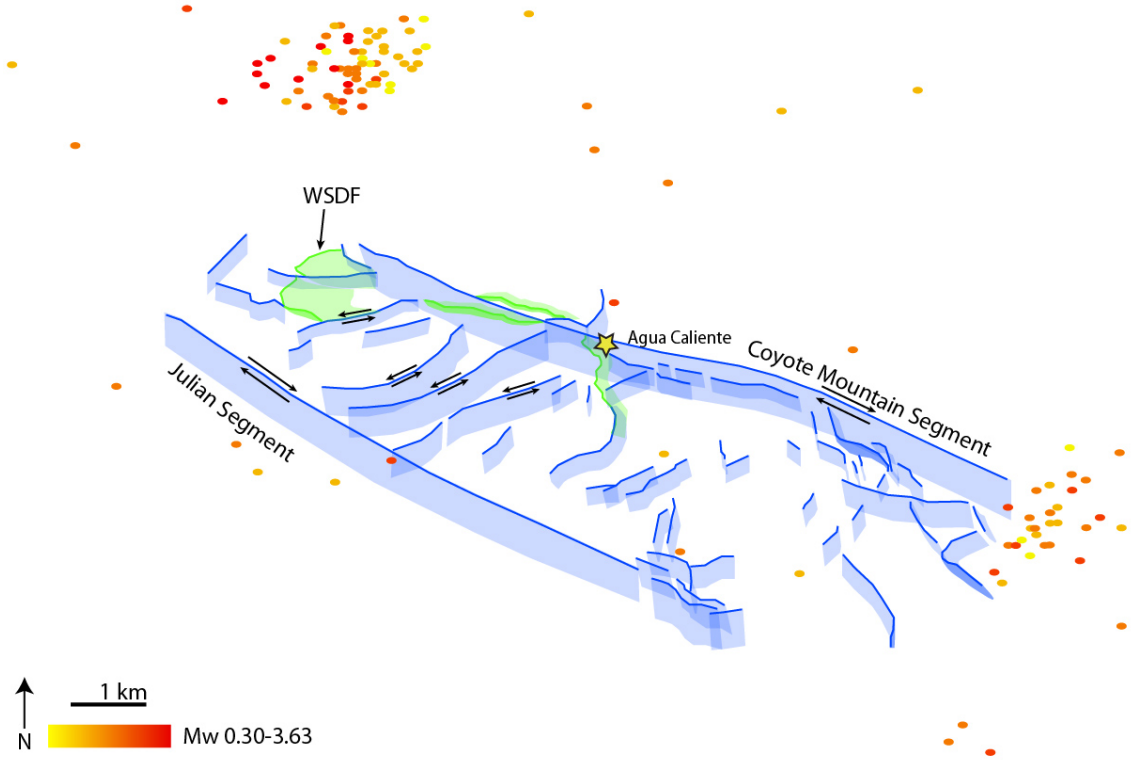

FIGURE 50 A simplified block diagram of the West Salton detachment and Elsinore fault zone geometry within the Tierra Blanca Mountains. The blue northwest-striking faults are the dominant fault planes and the green faults are strands of the detachment fault. Cross faults striking northeast connect the Julian and Coyote Mountain segments. Earthquake epicenters within 10 km of Agua Caliente between June 9-August 22, 2011 occur in the southeast portion of the Tierra Blanca Mountains and north of the mountains in the Vallecito Valley.

DISCUSSION

I define the nature and extent of damage associated with the faults in the Tierra Blanca Mountains, southern California, in order to understand the role of fault zones in fluid migration, determine the intersection geometry of the detachment and strike-slip faults, and identify relationships between hydrogeochemistry, protolith alteration, and local seismic events.

Macroscale Interpretations

The Earthquake Valley fault and the Julian segment of the Elsinore fault encompass the study area, which form a double-stranded section of the central Elsinore fault system. In the Vallecito Mountains the Earthquake Valley fault changes orientation to the southwest and is associated with numerous cross faults within the mountain range (Kairouz, 2005). The Julian segment enters the Tierra Blanca Mountains from the northwest and extends through Inner Pasture and farther south. The Julian segment of the Elsinore fault overlaps with and steps left to the Coyote Mountain segment at the Tierra Blanca Mountains in a complex interplay of smaller faults (Figure 3) much like faults observed by Kairouz (2005) in the Vallecito Mountains. The transition from the double-stranded region of the Elsinore fault system to the single-stranded Coyote Mountain segment resembles a zipper (S. Janecke, personal communication, 2012), as the two main traces appear to distribute strain through the Tierra Blanca Mountains by way of small oblique left-lateral strike-slip faults (Figure 51). Also present in the area is the inactive West Salton detachment fault, whose trace has been dissected and displaced by the Elsinore fault in the Tierra Blanca Mountains (Figure 3) so that the geometry of the intersection

between the inactive low-angle normal fault and the active strike-slip fault is much more complicated than previously interpreted (Figure 51; e.g. Dorsey et al., 2011).

The West Salton detachment fault in the Tierra Blanca Mountains exhibits brittle deformation based on the presence of cataclasite observed in thin section and outcrop (Figure 27D). The detachment fault likely originally wrapped around the northernmost section of the Tierra Blanca Mountains and divided the Palm Spring Formation and Canebrake Conglomerate from the Triassic metasedimentary rocks and the Cretaceous La Posta pluton. The detachment fault trace remains at the mountain front fault immediately west of Agua Caliente County Park and winds through Moonlight Canyon south of the park. As the regional style of tectonics transitioned to strike-slip motion, the fault trace in Moonlight Canyon was re-occupied by a fault associated with the Elsinore fault system. Data supporting this hypothesis are presented in the following section.

Along the eastern flank of the Tierra Blanca Mountains numerous small faults are parallel to the mountain front, and I propose these northeast-dipping subsidiary faults likely truncate into the main Elsinore fault trace because they are not laterally continuous and create a tulip-like structure (Figure 13). Because the Coyote Mountain and Julian segments overlap and bound the Tierra Blanca Mountains, they form an area of compression and uplift the mountain range. The overall slip of the Coyote Mountain and Julian segments is strike slip, but at the Tierra Blanca Mountains, the Coyote Mountain segment also exhibits a normal-oblique component and has the associated paralleling subsidiary faults to the west. If subsidiary faults exist to the east of the main trace, they are hidden beneath Quaternary alluvium.

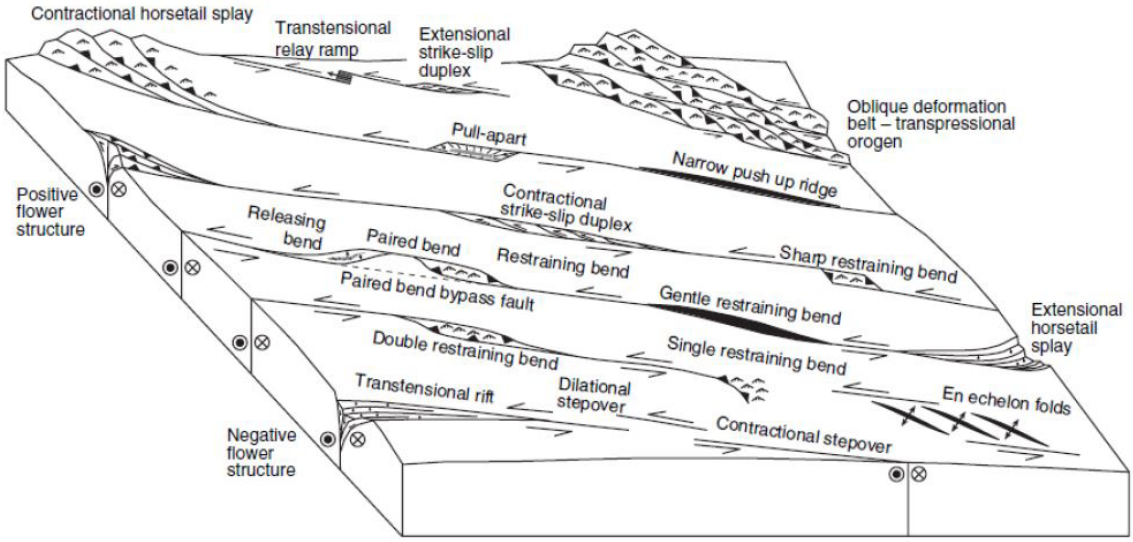

FIGURE 51 Fault stepover geometries and associated tectonic response from Cunningham and Mann, 2007.

MESOSCALE INTERPRETATIONS

Along the trace of the West Salton detachment fault, rock alteration consists of the presence of an ultracataclasite zone directly below the fault, a chlorite-breccia zone in the footwall, and pseudotachylyte scattered along the fault trace near Yaqui Ridge (Axen et al., 2009) northeast of the study area. In the Tierra Blanca Mountains the West Salton detachment fault is distinguished by footwall foliations (Figure 24). At the county park the contact between the bleached fine-grained protolith gouge and the fault surface is sharp and distinct. Because of this relationship, I propose the detachment fault plane behaves as a barrier to fluid flow so fluids in the hanging wall do not infiltrate beyond the fault into the footwall in this location. The bleached areas are focused at the park (Plate 1) and transition to intact tonalite along Moonlight Canyon the alteration and friable tonalite to the north and south of the park along the Coyote Mountain segment damage zone.

The West Salton detachment fault trace along Moonlight Canyon appears to be re-occupied by initiation of the Elsinore fault ~ 1.2-1.0 Ma (Dorsey et al., 2012). Data supporting this interpretation include slip indicators found along the fault in the canyon (Figure 27), the presence of at least two stages of cataclasite in a thin section from an outcrop represented in Figure 39, and the bleaching and staining that extend into the canyon. The first phase of slip, possibly prior to initiation of the Elsinore fault, involved the comminution of the original protolith (Figure 15) and formation of cataclasite (Figure 39). During phase two of fault slip, which may have been when the Elsinore fault took over and shut down slip along the detachment fault, the previous phase of cataclasite was brecciated, and fluids stained the fine-grained groundmass red and orange (Figure 27D).

Cunningham and Mann (2007) propose narrow stepovers have stronger kinematic linkage than wide stepovers along strike-slip faults. The distance between the Julian and Coyote Mountain segments is ~ 2.7-3.8 km with numerous northeast-striking linkage faults between the two main faults. The linkage is in the form of a cross-step left-lateral oblique strike-slip fault system mostly present within (and forming) the northeast-southwest striking valleys through the Tierra Blanca and Vallecito mountain ranges. Such linking fault systems commonly occur in between stepovers and in fault restraining and releasing bends (Dooley and McClay, 1997; McClay and Bonora, 2001). Stepovers create a rhomboidal geometry and may have oblique-slip between the two master faults (Figure 52; Cunningham and Mann, 2007). Dibblee (1996) refers to the blocks between the linkage faults as transverse fault blocks (Figure 53). Fault meshes interconnect main faults and distribute slip amongst the mesh (Janecke, 2009) so the total amount of slip along sections of faults is distributed along hundreds of small interconnected surfaces rather

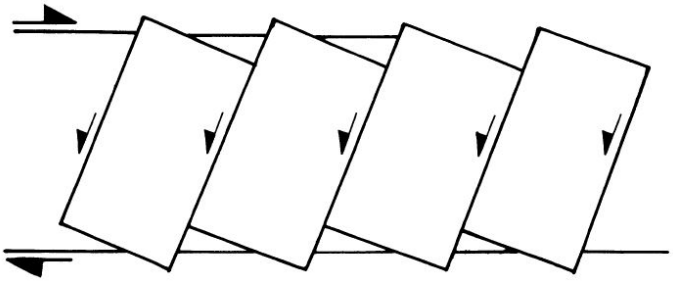

FIGURE 52 Left lateral cross faults bounding rotating blocks between two dominant right lateral faults from Peacock et al., 1998.

than along a main trace.

The thermal springs at Agua Caliente County Park are likely sourced from meteoric groundwater recharged from the nearby basins that was heated to 75-86°C at depths up to 2 km using the geothermal gradient presented by Rothstein and Manning (2003; Figure 54). Temperatures at the ground surface are typically ~ 30°C (Appendix B). Of the eight springs within the northeastern and eastern portions of the Tierra Blanca Mountains, four are in the park and a fifth is located behind Agua Caliente Springs General Store, in close proximity to the springs in the county park. One spring is in Marsh Canyon ~ 600 m northwest of the county park, and Marsh Trail (on the Agua Caliente Springs topographic map) leads to the spring where there are several sizeable palm trees. A seventh spring is little more than a trickle out of the tonalite in Moonlight Canyon (565612 m E 3645421 m N) and provides enough water for scrubby trees and undergrowth to grow in a narrow canyon. The eighth spring is very small and produces enough water for a pool ~ 1 m long, 0.5 m wide, and ~ 20 cm deep located approximately at 567555 m E 3644936 m N. All of the springs are within the damage zone of the Coyote Mountain segment. The location of the warm springs at the convergence of two fault zones suggests there is structural control

on the upward flow of the thermal waters. In order for the fluids to retain heat long enough to be heated at the surface the flow rate must be rapid, and either the fault damage zones or the sedimentary basin-plutonic rock contact would extend to the depth of the fluid source (> 2 km).

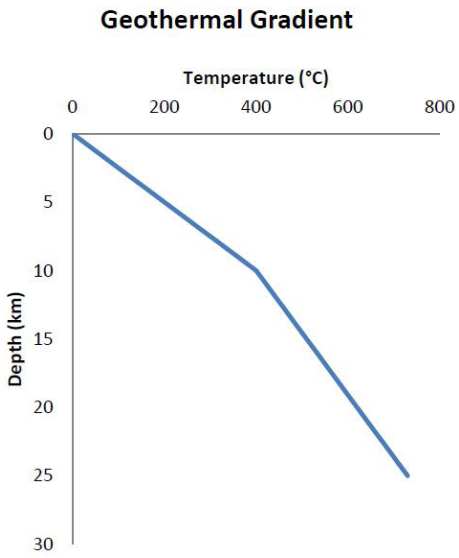

FIGURE 53 The geothermal gradient in the Peninsular Ranges batholith is 40°C/km for the uppermost 10 km and changes to 22°C/km at depths greater than 10 km based on work by Rothstein and Manning, 2003.

The damage zone associated with the Elsinore fault is up to 500-m wide and is composed of numerous parallel subsidiary faults of varying orientations and slip directions. The boundary of the damage zone is gradational, but for this study, the boundary is defined as the westernmost subsidiary fault along the mountain flank. The gradational boundary is noticeable in the field as the amount of bleached, fractured, and/or friable tonalite lessens and the cohesive tonalite with euhedral minerals dominates the protolith. Some of the faults exhibited multiple slip indicators plunging in directions from horizontal to vertical. The La Posta protolith is heavily fractured throughout the range, but to a higher degree adjacent to the subsidiary faults. The protolith is very friable, often bleached, and deteriorates into grus. The three sets of scanline data provided fracture densities in three locations within the northeastern regions of the Tierra Blanca Mountains. The highest fracture density (5 fractures per meter) was in Coyote Canyon and is ~ 36 m northeast of the closest observed subsidiary fault, parallel to the Coyote Mountain segment. The lowest fracture density is near the mouth of Moonlight Canyon along a cross fault and was 3.14 fractures per meter.

Structurally, this area appears to have been affected by only the cross faulting unlike the previously mentioned scanline that was affected by the oblique slip associated with the Coyote Mountain segment. I propose more slip occurred along the mountain front faults than the cross faults because the cross faults do not exhibit identifiable displacement, and I interpret them to transfer strain between the Julian segment to the Coyote Mountain segment.

Microscale Interpretations

Features and relationships observed in the thin sections collected from the Tierra Blanca Mountains provide a microscale view of the deformation mechanisms and textures within the faults, damage zones, and protolith. Samples from Canebrake Canyon provide an image of the protolith prior to faulting, fluid infiltration, and alteration. The protolith is composed of large subhedral to euhedral quartz and plagioclase grains and biotite sheets (Figure 15). I presume the large, unaltered crystals in the La Posta pluton composing the Tierra Blanca Mountains were ubiquitous prior to deformation and faulting. The footwall of the West Salton detachment fault adjacent to and south of Agua Caliente County Park contains entrained biotite defining foliation and mode I open fractures (Figure 37B and Figure 38). Clasts within cataclasite along the detachment fault are angular at all scales, and many of the larger clasts are remnants from an earlier cataclasite event (Figure 39).

In areas affected by strike-slip motion along the Coyote Mountain segment of the Elsinore fault, the protolith is altered: samples near the county park experienced significant sericitization and chlorite pseudomorphing after biotite. Farther south the protolith

damage exhibits large mode I fractures filled with chlorite and also contains entrained biotite. Within the same canyon but closer to the mountain front it is evident pore fluid pressures were at least momentarily very high, causing mode I fractures to open within quartz grains in all directions and fill the fractures with precipitated calcite. Not all rocks found near the mountain front are heavily damaged or altered. Fragments from the fractured crystals reworked in shearing along the faults form a dilational breccia within the northern extent of the Coyote Mountain segment of the Elsinore fault system.

Sericitization of plagioclase crystals in many of the samples collected on the eastern flank of the Tierra Blanca Mountains indicates the influences of heated fluids migrating through or accumulating in the La Posta tonalite. Sericitization typically occurs between ~ 230-560°C (Dilles, 2012, written communication). Quartz crystals also found in the sericitized areas exhibit mode I fracturing in multiple orientations and this indicates pore fluid pressure were at least temporarily very high to overcome the tensile strength of quartz (16 GPa in a defect-free crystal, Davis and Reynolds, 1996). Necessary pore fluid pressures may have arisen from local seismic pulses along the Coyote Mountain segment. One quartz grain from Coyote Canyon is dilated 0.313 cm perpendicular to the fault slip surface and 0.137 cm parallel with the fault, increasing the volume of the quartz 5.2% along its width and 8.1% along its length. Fluids within the fault zone may have reached supralithostatic pressure levels, and when the fault ruptures the fluids are released into and can rapidly open fractures, fill them with the fluids, and precipitate out the dissolved minerals. For example, in sample 7-1 (Figure 37E) fractures within a quartz crystal are filled with fine-crystalline calcite. Precipitated calcite is frequently observed in samples from the faults associated with the Coyote Mountain segment damage zone suggest-

ing the fluids associated with later phases of fault movement were enriched in dissolved calcite, possibly from feldspar weathering or deeper sources. Two possible sources for the calcite are dissolved calcium from the La Posta tonalite or from the crystalline limestone and dolostone in the Coyote Mountains southeast of the Tierra Blanca Mountains. The Coyote Mountain segment defines the southern extent of the Coyote Mountains, and calcite in the Tierra Blanca Mountains may have migrated from the marine deposits farther south along the Coyote Mountain segment. Precipitation can occur rapidly because of the increase of surface area within the newly fractured crystal (Mitchell and Faulkner, 2012).

Water Chemistry

In this section I interpret hydrogeochemical data from the spring box and compare these data to local seismicity. The fluids flowing through the Elsinore fault and West Salton detachment fault damage zones emerge in several springs that feed the commercial pools at Agua Caliente. These fault springs provide access to water sampling for water chemistry analyses. Stable isotope ratios analyzed included $^{13}C/^{12}C$, D/H, and $^{18}O/^{16}O$, to which their values were -17.5, -70, and -10.1, respectively. The $\delta^{13}C$ values are reported relative to PDB, and $\delta^{18}O$ and δD are reported relative to SMOW. The values of δD and $\delta^{18}O$ indicate the fluids are consistent with meteorically derived water (Figure 43). The $\delta^{13}C$ measurement of -17.5‰ PDB could indicate the water is from one of several sources including reduced carbon in sedimentary, igneous, or metamorphic rocks, meteorites, higher plants, eukaryotic algae, cyanobacteria, or methanogenic bacteria (Figure 42); however, taking into account regional geology, the most likely source for carbon in the springs at Agua Caliente County Park is dissolved carbon from an organic source, poten-

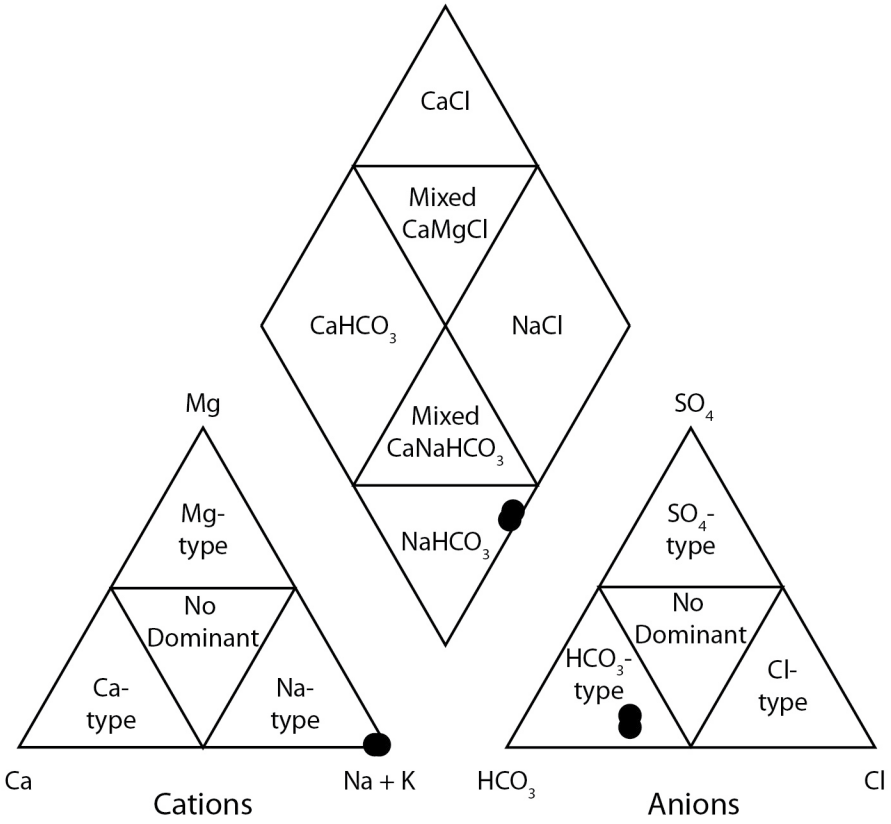

FIGURE 54 Piper diagram from cation and anion concentrations measured in February and November 2011 (classifications after Ravikumar and Somashekar, 2010).

tially vegetation surrounding the spring.

The Na-K-Ca geothermometer yields the maximum temperatures to which waters were heated from 75-86°C (Appendix B). According to the geothermal gradient for the Peninsular Ranges batholith generated by Rothstein and Manning (2003) in Figure 54, the fluids may have been heated at a maximum depth of ~ 2 km. However, the study area is on the western margin of the Salton Trough, which has a significantly higher geothermal gradient (> 150°C; Sass and Priest, 2002) that would allow the fluids to be heated at shallower depths. Several workers have proposed calcite twins can be used for geothermometry (Ferrill et al., 2004; Lacombe, 2010), and the absence of twins suggests calcite

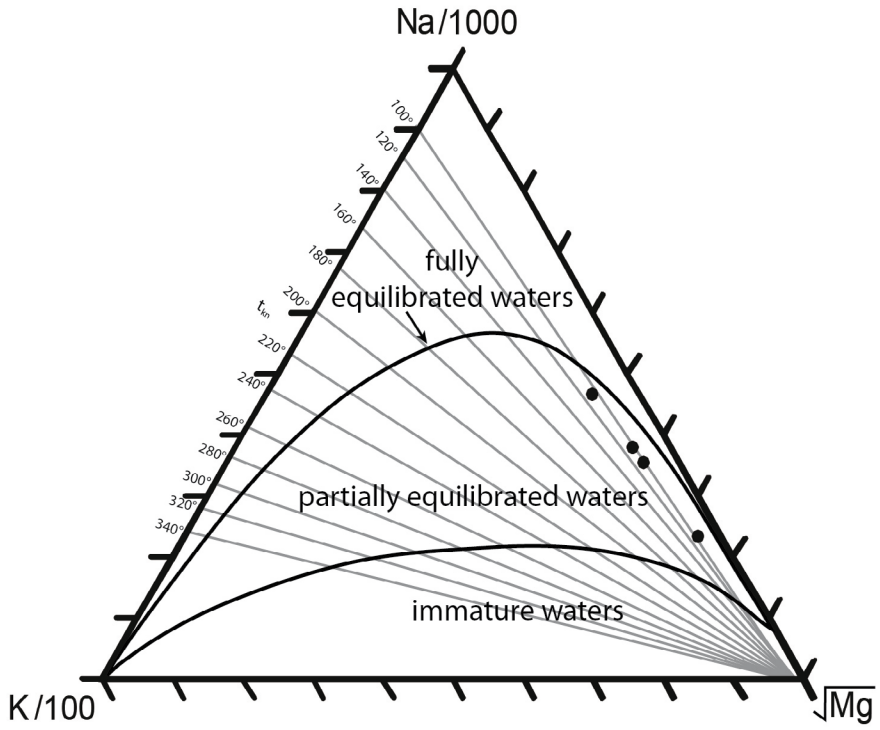

FIGURE 55 Na-K and K-Mg equilibrium temperatures calculated from ion concentrations measured at Agua Caliente County Park in February and November 2011. Diagram modified from Giggenbach, 1988 and Graham and Midgley, 2000.

precipitation, like the calcite found in the damage zones, occurred in low temperature regimes. An equilibrium temperature tri-plot of Na, K, and Mg shows the fluids were partially equilibrated in February and November 2011 (Figure 55).

The pH value measured in November 2011 was 9.55, and this is within the range of the park's occasional measurements which fluctuate around 8-9. Alteration types evolve as pH and temperatures of the fluids and protolith change (Dilles, 2012, unpublished). Measuring pH of the fluid is important because it is one of the factors controlling the solubility and availability of elements involved with alteration.

Water temperature steadily increases as the summer progresses (Figure 45). Electrical conductivity daily averages rise throughout June 2011, drop during July, and

increase in August, where they become more or less consistent (Figure 45). Daily water level averages exhibit some distinct rises and reach a peak of 1.74 m on July 5, 2011 (Figure 45). The level remains nearly consistent from July 28 to August 15. Of the 100 earthquakes within 10 km of the spring box during summer 2011, 8% occurred within 5 km. The region experiences a large amount of seismicity, but the events are almost always < M_w 3.0; 38.5% of the 400 earthquakes within the polygon registered M_w between 0-0.9; 57.25% were M_w 1.0-1.9, and the highest magnitude event was M_w 4.11. All earthquakes recorded occurred while the Levelogger was logging conditions in the spring box, both in February and June-August 2011.

Spring temperatures and conductivity have separate periods and frequency. Spring temperatures and air temperatures display a diurnal cycle (Figure 45). Most of the recorded earthquakes during the logging period occurred from June 9-July 20, and this correlates with the most dispersion in the conductivity periods and frequency. Not all seismic events are associated with jumps or falls in the conductivity, temperature, or water level data. When there is a correlation, hypocenter distances from the spring vary and subsurface structural connectivity is not typically straightforward as the majority of the events occurred south of the Vallecito Mountains along cross faults. A rainfall and barometric pressure archive of the region would likely benefit this study and help determine how much water levels are impacted by precipitation fluxes versus earthquake activity. In addition to daily cycles, spring temperature and water level are coupled and behave similarly. For example, on July 3 water levels jumped from ~ 1.1 m to ~ 1.4 m and temperatures jumped from 30.9°C to 30.98°C. Other temperature rises correspond with rapid jumps in water levels. The fluids may have collected from precipitation runoff and entered the

groundwater system, descended to a maximum depth of 2.14 km (based on the geothermal gradient from Rothstein and Manning, 2003), and returned to the surface during seismic events.

One aim of this study was to produce a set procedure of fluid analysis along fault zones. I suggest the following analyses to be performed when observing effusing fluids:

1. Measure cation and anion concentrations in order to compare the concentrations with the host rock composition. If possible, measure cations and anions in each season and after significant earthquakes in the area to determine seasonal variations and concentration differences from the passage of fluids pre-, syn-, or post-seismicity. Cations and anions are also used to calculate geothermometry.
2. Use a logger for temperature, water level, and conductivity. Make sure the instrument is properly calibrated. Log the fluids through seasons and compare with local earthquake activity.
3. Collect samples for $\delta^{18}O$ and δD to determine the source and rock-water interaction history of the fluids—whether it is magmatic, meteoric, etc.

Protolith Aleteration

The presence of clays at the bleached area of the county park indicates the primary minerals in the protolith have broken down via alteration pathways—possibly reaction pathways listed in Table 13. Though the Tierra Blanca Mountains and Anza Borrego Desert are very arid environments, groundwater rising at Agua Caliente could provide the necessary moisture to spur reactions in the already-fragmented fault-related rocks, thus facilitating bleaching and alteration of the protolith. More realistically, the bulk of the

alteration occurred prior to exhumation. Water-rock alteration conditions required to form the clay, zeolite, and chlorite minerals present within the most intense bleached zones range from low to high water-rock ratios (Schwenzer and Kring, 2009), and some to all alteration would have occurred at depth, especially associated with fault movement, only later exhumed.

The minerals identified in hand sample, thin section, and x-ray diffraction can be assigned to different mineralization phases. Quartz, plagioclase, and biotite are part of the original tonalite. Kaolinite, heulandite, nontronite, laumontite, chlorite, epidote, calcite, and Fe-rich minerals are associated with alteration in the fault damage zone and where the springs emerge. In the bleached region of the county park, plagioclase is broken down and altered to kaolinite, montmorillonite, heulandite, and nontronite. The X-ray diffraction analysis on samples from the outcrop in Figure 26 shows a possible presence of ferrocolumbite and ankerite, both of which contain iron and typically result from iron-rich hydrothermal mineralization within veins. X-ray diffraction analyses of samples collected throughout the Tierra Blanca Mountains, especially from alteration zones, shows the composition of the protolith and alteration products (Table 11 and Figure 46; Appendix D). Based from observations of thin sections, samples associated with the detachment fault, especially along Moonlight Canyon, experienced at least two episodes of cataclasis with iron-rich fluids altering the rocks at a later date. The cataclasis appears to have removed the original biotite and albite minerals from the rock leaving the more-resistant quartz. The staining in some of the thin sections is not uniform; rather it is variable and may be a record of flow pathways (e.g. Figure 39). In the bleached regions in the hanging wall of the detachment fault, it is also apparent an iron-rich fluid resided within the fault

TABLE 10 Alteration reaction pathways if calculated at standard state

Reaction	Formula	Alteration Type	$\Delta H_{25°}$ (kJ/mole)
Microcline to Sericite[1]	$3\ KAlSi_3O_8 + 2\ H^+ = KAl_3Si_3O_{10}(OH)_2 + 6\ SiO_2 + 2\ K^+$	Advanced Argillic Alteration	- 14
Sericite to Kaolinite[1]	$KAl_3Si_3O_{10}(OH)_2 + 1.5\ H_2O + H^+ = 1.5\ Al_2Si_2O_5(OH)_4 + K^+$	Advanced Argillic Alteration	- 27
Albite to Kaolinite[2]	$2\ NaAlSi_3O_8 + 9\ H_2O + 2\ H^+ \leftrightarrow Al_2Si_2O_5(OH)_4 + 2\ Na^+ + 4\ H_4SiO_4$	Intermediate Argillic Alteration	+ 238
Albite to Montmorillonite[1]	$2.33\ NaAlSi_3O_8 + 2\ H^+ = Na_{0.33}Al_{2.33}Si_{3.67}O_{10}(OH)_2 + 3.33\ SiO_2 + 2Na^+$	Intermediate Argillic Alteration	- 42
Montmorillonite to Kaolinite[1]	$3\ Na_{0.33}Al_{2.33}Si_{3.67}O_{10}(OH)_2 + 3.5\ H_2O + H^+ = 3.5Al_2Si_2O_5(OH)_4 + 4\ SiO_2$	Intermediate Argillic Alteration	- 44
Biotite to Chlorite[1]	$2\ KFe_3AlSi_3O_{10}(OH)_2 + 5\ Mg^{2+} + 4\ H_2O \rightarrow Mg_5Al_2Si_3O_{10}(OH)_8 + 3\ SiO_2 + 2\ K^+ + 6\ Fe^{2+}$	Propylitic Alteration	+ 149
Albite to Epidote[1]	$2\ NaAlSi_3O_8 + 2\ Ca^{2+} + Fe^{3+} + 3\ H_2O \rightarrow Ca_2FeAl_2Si_3O_{12}(OH) + 3\ SiO_2 + 2\ Na^+ + 5\ H^+$	Propylitic Alteration	+ 83
Albite to Laumontite[1]	$2\ NaAlSi_3O_8 + Ca^{2+} + 4\ H_2O = CaAl_2Si_4O_{12}(H_2O)_4 + 2\ SiO_2 + 2\ Na^+$	Propylitic Alteration	- 10
1. Barnes, 2000. 2. Faure, 1991.			

Table 11 Water Chemistry reported by Agua Caliente County Park

The Following Are Possibly Found In Water At This County Regional Park		
Constituent	Maximum Contaminant Level mg/L	Level Detected
Copper	1.00	<0.05
Iron	0.30	<0.10
Manganese	0.05	<0.03
Foaming Agents	0.50	<0.50
Zinc	5.0	<0.01
Total Solids	1000	478
Conductance	1600UMHO/Cm	660
Chloride	500	120.2
Sulfate	500	58.9
Fluoride	1.6	5.56
Nitrate (NO3)	45	0.01

rocks post-bleaching (Figure 5).

Laumontite is abundant in the bleached zones at the county park. The exothermic transformation from anorthite to laumontite is irreversible because the reverse reaction is limited by calcite precipitation (Faure, 1991). Laumontite typically forms at near-surface environments (Faure, 1991). Albite can also decompose to laumontite and silica as well as to kaolinite and silica (Table 10; Faure, 1991).

Current water conditions are alkaline, though the alteration assemblages observed require acidic conditions to form. The pH may have been much lower or there could have been a fluid source change. Kaolinite can form from the incongruent dissolution of aluminum silicate minerals when reacting with abundant acidic water (Faure, 1991). Albite can alter to kaolinite when in contact with aqueous solutions (Table 10; Faure, 1991). The exothermic reaction yields excess sodium ions. The elemental analyses of the

spring at Agua Caliente County Park show an abundance of sodium and small amounts of aluminum, presumably because the aluminum is captured within the kaolinite chemical structure. Laumontite also alters to kaolinite (Faure, 1991). Kaolinite within the bleached zones of the study area may be resultant from albite → kaolinite, or anorthite → laumontite → kaolinite reaction pathways (Faure, 1991), and sericite → kaolinite (Barnes, 2000) since all of the required minerals are present within the protolith and altered area (Table 10). Kaolinite can form at surface temperatures and atmospheric pressures in acidic conditions and given a very long time (Kerr, 1955). Dilles (2012, unpublished) proposed kaolinite can form in a more acidic environment below 200°C in the advanced argillic alteration stage. The argillic alteration at the county park may indicate this is the later phase of alteration corresponding to the heated fluids. The spring chemistry presented in this research may shed light into the nature of fluid-rock interactions that produced the alteration assemblages, but it may have changed significantly throughout time.

Biotite is altered to chlorite in an endothermic reaction at standard temperature and pressure (Table 10; Barnes, 2000), but this is unfavorable. Figure 37A shows a chlorite fringe on a biotite flake in thin section. Albite can alter to epidote in an endothermic reaction (Table 10). Though epidote is not detected in x-ray diffraction, thin sections reveal a minute presence of epidote in the area. Sericite is copious within plagioclase crystals. Chlorite and epidote form in less acidic conditions and are associated with propylitic alteration that occurs around 300°C (Dilles, 2012, unpublished). Propylitic alteration may have happened post sericitization of the protolith but prior to advanced argillic alteration. In the geochemical transect (Figure 8) the x-ray diffraction analyses show a consistent appearance of biotite at the exposed detachment fault plane and within the footwall. Sam-

ples from the bleached portions in the hanging wall of the detachment fault contain clays (kaolinite, montmorillonite, nontronite, and fraipontite), zeolites (heulandite and laumontite), and chlorite (clinochlore). Quartz and albite crystals in the bleached zone resisted alteration and grain-size reduction more than biotite. A concentrated chlorite veneer, quartz, and albite separate the bleached area from the foliated facies that grades into undeformed protolith.

Water chemistry reported by the park shows a relatively high concentration of fluoride of 5.56 mg/L (Table 4). Possible sources for fluorine in this region include the breakdown of fluorite, apatite, and micas from the La Posta tonalite. Maximum allowable amounts of fluorine in potable water are < 1.5 mg/L (Fawell et al., 2006) which means the water at the county park requires treatment before human consumption. Concentrations > 1.5 mg/L lead to tooth coloring and bone pitting, and concentrations > 10 mg/L (World Health Organization, no date). The EPA's current maximum contaminant level for Fluoride is 4.0 mg/L, with a secondary standard set at 2.0 mg/L (EPA, 2009).

Fluids transported along the faults at Agua Caliente alter the protolith because of disequilibrium between the fluid system and the wall rock minerals. Agua Caliente is the locus of intense alteration and damage resultant from complex faulting combined with fluid flow. The alteration is consistent with the idea that the fault geometry controls where the fluids migrate (Sibson, 1987). A consistent pH would indicate there is little change in the fluids while a fluctuating one, like exhibited in the springs addressed in this research, would indicate the passage of elements through the system or precipitation of minerals (Appelo, 1994). Elemental analysis data from February 2011 show presence of strontium, silica, sulfur, magnesium, potassium, iron, calcium, barium, boron, and chlorine.

Changes in water conditions and protolith alteration at Agua Caliente are a result of active deformation. I observed spring flow rates increase during earthquake swarms similar to reports of a park ranger (Mark Stockdale, personal communication, 2012). This phenomenon is likely due to P waves creating different pore pressures and trigger fluid migration (Micklethwaite and Cox, 2004; Manga and Wang, 2007). Fluid changes we observed that might be related to seismicity, as well as seasonal influences, include temperature, water level, conductivity, and cations and anions concentrations (Claesson et al., 2004) which appear to be associated, in some cases in complex ways. Seasonal changes are slow and continuous while sudden jumps or drops in the logged attributes are presumed to be directly related to local seismicity. Though the length of this study is not probably long enough in duration to notice significant changes elemental concentrations, there is value in initializing data collection to benefit future comparable studies and to establish a set of tests to conduct at other springs.

Earthquake Activity

Spring characteristics and seismic events during summer 2011 may have a loose connection. A peak in water level on June 20-21 and corresponding rise in water temperature follow earthquakes in Vallecito Valley and Carrizo Valley. Within a day, the water level resumed its earlier level. On July 3, 2011 water level jumped from 32.98 cm to 39.53 cm and reached its peak of 53 cm on July 5, 2011 and then dropped gradually down to 33.98 cm by July 10, 2011. The 13 earthquakes that occurred during this sudden rise in water level ranged from Mw 0.73-1.77 with the largest occurring on July 3, 2011, the same day as the observed rise. This event was ~ 6.71 km (4.17 mi) northwest from

the spring box near Ghost Mountain. Eight aftershocks surrounding the M_w 1.77 event occurred through July 10, 2011 and reached M_w 1.17. A finer look at the water level data reveals the rise began approximately one hour before the reported earthquake event. This may assist in an argument regarding earthquake precursors. Forty-five minutes after an M_w 0.95 quake on July 6, 2011 water level dropped 1.46 cm. In this interval from July 3-10, 2011 there are additional jumps in water level that are not associated with an earthquake event within 10 km of the spring box, and the rise corresponds with a barometric pressure rise during the same time period. The temperature log also increases from July 3-11, 2011. Conductivity, however, is variable during this interval, though it does exhibit a drop from July 6-10, 2011.

General conductivity trends are divided into three periods. The noise diagnostic of the first period (June 9-July 10) may be due to the active seismicity within 10 km. Most of the seismic events occurred ~ 5.5-6 km northwest of the spring box along unnamed left lateral-oblique faults mapped by Kairouz (2005) south of Whale Peak along the Bisnaga Alta Wash and Smuggler Canyon in the northern Vallecito Valley. The second period of conductivity (July 10-August 1) appears to be consistent with expected diurnal fluctuations, and the third (August 1-22) remains fairly constant, and variability decreases to ~ 29 μS/cm between peaks and troughs during the last few days of the logging period. The three variables remain nearly constant in the third period, which may be because there is little flowing into the system in this region during the height of summer.

CONCLUSIONS

This project examined several questions regarding the nature of fault-related damage as observed in the Tierra Blanca Mountains:

1. Is the damage at Agua Caliente area the result of slip on the Elsinore fault, the West Salton detachment fault, or both? Or, was damage localized at the intersection between the two faults?
2. Does fault-related damage vary measurably from the detachment fault to the Elsinore fault zone? Does the damage vary with lithology of the host rock?
3. Is damage proportional to the amount of slip?
4. Does the geometry of the fault intersection control the location of or is it related to fluid accumulation, and does alteration of the protolith occur because it is in disequilibrium with the thermal fluids remaining in the protolith?
5. Are changes in water chemistry and alteration a result of or related to active deformation and local seismicity?

Data presented here support the interpretation that the damage at Agua Caliente County Park in southern California is a result of the transition from the double-stranded Julian segment-Earthquake Valley fault into the northwest-striking single-stranded Coyote Mountain segment and its intersection with the inactive West Salton detachment fault. The eastern side of the Tierra Blanca Mountains hosts an up to 500-m wide damage zone in La Posta plutonic rocks affiliated with the Coyote Mountain segment of the Elsinore fault. The damage zone is exposed on the west side of the main fault plane and likely covered by basin alluvial deposits on the east side. The damage zone consists of bleached

and comminuted tonalite, closely spaced fractures, areas of red staining, and subsidiary faults. The fault system displays a complex geometry as numerous cross faults within arroyos link the Julian and Coyote Mountain segments of the Elsinore fault through the Tierra Blanca Mountains, and the cross faults distribute strain between the two segments. Evidence for these faults includes the linear valleys not traditionally seen as part of weathering granitic plutons. Foliated chloritic rocks are common along the arroyos, and in some places actual fault planes are exposed. Little slip has occurred along cross faults as the heavily fractured and grusified La Posta pluton gradually becomes much more intact and cohesive.

Damage from the oblique strike-slip faults in the Tierra Blanca Mountains is manifested almost completely within La Posta tonalite. The damage zone in the crystalline rock comprises at least five parallel strands of subsidiary faults into the mountains and fractures with a range of orientations. The fault traces in the Carrizo Valley are almost completely concealed though some alluvial fans emerging from the arroyos in the Tierra Blanca Mountains are truncated. Because the valley sediments are not intact, fractures are not identifiable in the host rock. Along Marsh Canyon the Coyote Mountain segment does not appear to generate as much fracturing as farther south along its trace, and no parallel subsidiary faults were seen in the Palm Spring Formation and Canebrake Conglomerate.

Damage along the Coyote Mountain segment southeast of Agua Caliente County Park decays into the mountain range and is identified by intense fracturing, clay development, and red-orange staining of the La Posta pluton. The damage extends up to 500 m from the mountain front into the mountains. The West Salton detachment fault has been cut and offset by faults within the Elsinore fault zone in the Tierra Blanca Moun-

tains (Plate 1). The detachment was once active along Moonlight Canyon but the trace has been re-occupied by a fault associated with the southern Elsinore fault system and the left stepover in the Tierra Blanca Mountains. The width of the damage zone in the Tierra Blanca Mountains does not appear to be proportional to the amount of estimated slip along the southern sections of the Elsinore fault system. I propose the high amounts of damage are a result of the transition from the Julian segment-Earthquake Valley fault double-stranded section to the single-stranded Coyote Mountain segment.

The Agua Caliente warm springs are coincident with the structural knot that formed at the convergence of the older, inactive West Salton detachment fault and the younger, active Elsinore fault. The damage and alteration immediately surrounding the springs are a manifestation of the interaction between the faults and fault rocks at depth and hydrothermal waters. The West Salton detachment fault surface adjacent to Agua Caliente County Park likely behaves as a barrier to fluid flow from the hanging wall to the footwall. Fluids migrate through the damage zone of the Coyote Mountain segment and bleach the protolith, altering the tonalite to kaolinite, montmorillonite, heulandite, and nontronite. Alteration of the protolith occurs as a result of the presence of fluids within the pore spaces of the damage zone, especially at the county park.

Given the water data recorded while logging, changes in water chemistry observed in 2011 are most likely related to seasonal changes and influenced by local seismic events. Water level is the property most influenced by earthquakes, a result of seismic pumping. The fluids accumulate in the subsurface from runoff based from the stable isotope data, and they are heated at depths up to 2.14 km based from Na-K-Ca geothermometry values. After the fluids are heated, they migrate back to the ground surface along the

Coyote Mountain segment of the Elsinore fault damage zone, with the base flow supplemented by enhanced flow associated with Mw 1.0 earthquakes, and accumulate at the base of the Tierra Blanca Mountains. Spring temperature cycle patterns mimic modern air temperatures but have a higher frequency, approximately three water cycles to one air cycle. I propose these fluids were once directly controlled or influenced by atmospheric temperatures but the two systems have been disconnected for some amount of time and the spring cycles are a remnant of the original accumulation.

Fault zone geometry has the potential to influence fluid flow by creating a barrier, a conduit, or a hybrid through the damage zone and core. In this study, I examined two fault systems, the West Salton detachment fault and the Elsinore fault network, and determined how the faults and fluids interact. The West Salton detachment fault behaves as a barrier to fluid flow immediately west of Agua Caliente County Park. The Elsinore fault has springs distributed along the Coyote Mountain segment, and the associated damage zone is commonly bleached or stained as fluids react with the host rock minerals. Local seismic events and spring properties are linked, and pulses of fluid during seismicity may elevate pore pressures necessary for rapid fracturing and fracture fills, enhancing permeability and porosity within the Coyote Mountain segment damage zone.

REFERENCES

Allison, M.L., Whitcomb, J.H., Cheatum, C.E., and McEuen, R.B., 1978, Elsinore fault seismicity—The September 13, 1973, Agua Caliente Springs, California, earthquake series: Bulletin of the Seismological Society of America, v. 68, p. 429-440.

Anderson, T.R., and Fairley, J.P., 2008, Relating permeability to the structural setting of a fault-controlled hydrothermal system in southeast Oregon, USA: Journal of Geophysical Research, v. 113, doi: 10.1029/2007JB004962.

Andrews, D.J., 2005, Rupture dynamics with energy loss outside the slip zone: Journal of Geophysical Research, v. 110, doi: 10.1029/2004JB003191.

Appelo, C.A.J., 1994, Cation and proton exchange, pH variations, and carbonate reactions in a freshening aquifer: Water Resources Research, v. 30, p. 2793-2805.

Atwater, T., 1970, Implications of Plate Tectonics for the Cenozoic Tectonic Evolution of Western North America: Geological Society of America Bulletin, v. 81, p. 3513-3536, doi: 10.1130/0016-7606(1970)81[3513:IOPTFT]2.0.CO;2.

Axen, G., Luther, A., Selverstone, J., and Khalsa, N., 2009, Evidence for stress rotation near the West Salton detachment fault (WSDF), Salton Trough, California: Geological Society of America Abstracts with Programs, v. 41, p. 50.

Axen, G.J., and Fletcher, J.M, 1998, Late Miocene-Pleistocene Extensional Faulting, Northern Gulf of California, Mexico and Salton Trough, California: International Geology Review, v. 40, p. 2170244, doi: 10.1080/00206819809465207.

Bailey, I.W., Ben-Zion, Y., Becker, T.W., and Holschneider, M., 2010, Quantifying focal mechanism heterogeneity for fault zones in central and southern California: Geophysical Journal International, v. 183, p. 433-450.

Barnes, H.L., 2000, Energetics of Hydrothermal Ore Deposition: International Geology Review, v. 42, p. 224-231.

Bellot, J., 2008, Hydrothermal fluids assisted crustal-scale strike-slip on the Argentat fault zone: Tectonophysics, v. 450, p. 21-33, doi: 10.1016/j.tecto.2007.12.009.

Billi, A., Salvini, F., and Storti, F., 2003, The damage zone-fault core transition in carbonate rocks—implications for fault growth, structure and permeability: Journal of Structural Geology, v. 25, p. 1779-1794.

Blisniuk, K., Rockwell, T., Owen, L.A., Lippincott, C., Caffee, M.W., and Dortch, J., 2010, Late Quaternary slip rate gradient defined using high-resolution topography and ^{10}Be dating of offset landforms on the southern San Jacinto Fault zone, California: Journal of Geophysical Research, v. 115, B08401, doi: 10.1029/2009JB006346.

Bouvier, J.D., and Kaars-Sijpesteijn, C.H., 1989, Three-Dimensional Seismic Interpretation and Fault Sealing Investigations, Nun River Field, Nigeria: American Association of Petroleum Geologists Bulletin, v. 73, p. 1397-1414.

Brodsky, E.E., Ma, K.-F., Mori, J., Saffer, D.M., 2009, Rapid response drilling: Past, present, and future: Workshop report, 30 p., http://www.pmc.ucsc.edu/~rapid/Report.pdf.

Brownlow, A.H., 1996, Geochemistry, (2nd edition): Upper Saddle River, New Jersey, Prentice Hall, 1996.

Caine, J.S., Bruhn, R.L., and Forster, C.B., 2010, Internal structure, fault rocks, and inferences regarding deformation, fluid flow, and mineralization in the seismogenic Stillwater normal fault, Dixie Valley, Nevada: Journal of Structural Geology, v. 32, p. 1576-1589, doi: 10.1016/j.jsg.2010.03.004.

Caine, J.S., Evans, J.P., and Forster, C.B., 1996, Fault zone architecture and permeability structure: Geology, v. 24, p. 1025-1028.

California Department of Water Resources, California's Groundwater, Bulletin 118, Update 2003, http://www.water.ca.gov/groundwater/bulletin118/update2003.cfm, November 2011.

Catlos, E.J., Sorensen, S.S., and Harrison, T.M., 2000, Th-Pb ion-microprobe dating of allanite: American Mineralogist, v. 85, p. 633-648.

Chester, F.M., and Logan, J.M., 1986, Implications for Mechanical Properties of Brittle Faults from Observations of the Punchbowl Fault Zone, California: Pageoph, v. 124, p. 79-106.

Chester, F.M., Evans, J.P., and Biegel, R.L., 1993, Internal structure and weakening mechanisms of the San Andreas Fault: Journal of Geophysical Research, v. 98, p. 771-786.

Cicerone, R.D., Ebel, J.E., and Britton, J., 2009, A systematic compilation of earthquake precursors: Tectonophysics, v. 476, p. 371-396.

Claesson, L., Skelton, A., Graham, C., and Morth, C.-M., 2007, The timescale and mechanisms of fault sealing and water-rock interaction after an earthquake: Geofluids, v. 7, p. 427-440, doi: 10.1111/j.1468-8123.2007.00197.x.

Claesson, L., Skelton, A., Graham, C., Dietl, C., Morth, M., Torssander, p., and Kockum, I., 2004, Hydrogeochemical changes before and after a major earthquake: Geology, v. 32, p. 641-644; doi: 10.1130/G20542.1

Clinkenbeard, J.P., 1987, The mineralogy, geochemistry, and geochronology of the La Posta pluton, San Diego and Imperial Counties, California [M.S. thesis]: San Diego State University, San Diego, California, 215 p.

Clinkenbeard, J.P., and Walawender, M.J., 1989, Mineralogy of the La Posta pluton: Implications for the origin of zoned plutons in the eastern Peninsular Ranges batholiths, southern and Baja California: American Mineralogist, v. 74, p. 1258-1269.

Coplen, T.B., 1994, Reporting of stable hydrogen, carbon, and oxygen isotopic abundances: Pure and Applied Chemistry, v. 86, p. 273-276

Cunningham, W.D., and Mann, P., 2007, Tectonics of strike-slip restraining and releasing bends, *in* Cunningham, W.D., and Mann, P., eds., Tectonics of strike-slip restraining and releasing bends: Geological Society, London, Special Publications, v. 290, p. 1-12.

Curewitz, D., and Karson, J.A., 1997, Structural settings of hydrothermal outflow: Fracture permeability maintained by fault propagation and interaction: Journal of Volcanology and Geothermal Research, v. 79, p. 149-168.

Dawson, T.E., Rockwell, T.K., Weldon, R.J., and Wills, C.J., 2008, Summary of Geologic Data and Developments of A Priori Rupture Models for the Elsinore, San Jacinto, and Garlock Faults, Appendix F: USGS Open File Report 2007-1437F.

Dibblee, T.W., Jr., 1996, Stratigraphy and tectonics of the Vallecito-Fish Creek Mountains, Vallecito Badlands, Coyote Mountains, and Yuha Desert, Southwestern Imperial Basin, *in* Abbott, P.L., and Seymour, D.C., eds., Sturzstroms and detachment faults, Anza-Borrego Desert State Park California: South Coast Geological Society Annual Field Trip Guide Book Number 24, p. 59-79.

Dooley, T., and McClay, K., 1997, Analog Modeling of Pull-Apart Basins: AAPG Bulletin, v. 81, p. 1804-1826.

Dor, O., Rockwell, T.K., and Ben-Zion, Y., 2006, Geological observations of damage asymmetry in the structure of the San Jacinto, San Andreas and Punchbowl faults in Southern California—A possible indicator for preferred rupture propagation direction: Pageoph, v. 163, p. 301-349.

Dorsey, R.J., Axen, G.J., Peryam, T.C., and Kairouz, M.E., 2012, Initiation of the Southern Elsinore Fault at ~ 1.2 Ma—Evidence from the Fish Creek-Vallecito Basin, southern California: Tectonics, v. 31, TC2006, doi: 10.1029/2011TC003009.

Dorsey, R.J., Housen, B.A., Janecke, S.U., Fanning, C.M., and Spears, A.L.F., 2011, Stratigraphic record of basin development within the San Andreas fault system: Late Cenozoic Fish Creek—Vallecito basin, southern California: Geological Society of America Bulletin, doi: 10.1130/B30168.1.

Ehlers, T.A., and Chapman, D.S., 1999, Normal fault thermal regimes—conductive and hydrothermal heat transfer surrounding the Wasatch fault, Utah: Tectonophysics, v. 312, p. 217-234.

Elders, W.A., Rex, R.W., Meidav, T., Robinson, P.T., and Biehler, S., 1972, Crustal Spreading in Southern California: Science, v. 178, p. 1-24, doi:10.1029/2004JB003169.

EPA, 2009, National Primary Drinking Water Regulations, http://water.epa.gov/drink/contaminants/upload/mcl-2.pdf, (November 2011).

Evans, J.P., and Chester, F.M., 1995, Fluid-rock interactions in faults of the San Andreas system: Inferences from San Gabriel fault rock geochemistry and microstructures: Journal of Geophysical Research, v. 100, p. 13007-13020.

Evans, J.P., Forster, C.B., and Goddard, J.V., 1997, Permeability of fault-related rocks, and implications for hydraulic structure of fault zones: Journal of Structural Geology, v. 19, p. 1393-1404.

Evans, K.F., Genter, A., and Sausse, J., 2005, Permeability creation and damage due to massive fluid injections into granite at 3.5 km at Soultz—1. Borehole observations: Journal of Geophysical Research, v. 110, B04203.

Fairley, J., Heffner, J., and Hinds, J., 2003, Geostatistical evaluation of permeability in an active fault zone: Geophysical Research Letters, v. 30, doi: 10.1029/2003GL018064.

Fairley, J.P., and Hinds, J.J., 2004, Field observation of fluid circulation patterns in a normal fault system: Geophysical Research Letters, v. 31, doi: 10.1029/2004GL020812.

Faulkner, D.R., Jackson, C.A.L., Lunn, R.J., Schlische, R.W., Shipton, Z.K., Wibberley, C.A.J., and Withjack, M.O., 2010, A review of recent developments concerning the structure, mechanics and fluid flow properties of fault zones: Journal of Structural Geology, v. 32 , p. 1557-1575, doi: 10.1016/j.jsg.1010.06.009.

Faulkner, D.R., Armitage, P.J., Blake, O.O., Mitchell, T.M., 2001, Characterizing fault damage zones in the field and laboratory; Scaling and physical properties: American Geophysical Union, Fall Meeting, abstract #T11E-01.

Faulkner, D.R., Mitchell, T.M., Healy, D., and Heap, M.J., 2006, Slip on ‘weak’ faults by the roatation of regional stress in the fracture damage zone: Nature, v. 444, p. 922-925, doi: 10.1038/nature05353.

Faure, G., 1991, Principles and applications of inorganic geochemistry, MacMillan, New York, 626 p.

Fawell, J., Bailey, K., Chilton, J., Dahi, E., Fewtrell, L., and Magara, Y., 2006, Fluoride in Drinking-water: Padstow, Cornwall, UK, World Health Organization, 144 p.

Fay, N.P., and Humphreys, E.D., 2005, Fault slip rates, effects of elastic heterogeneity on geodetic data, and the strength of the lower crust in the Salton Trough region, southern California: Journal of Geophysical Research, v. 110, doi: 10.1029/2004JB003548.

Ferrill, D.A., Morris, A.P., Evans, M.A., Burkhard, M., Groshong, R.H., Jr., Onasch, C.M., 2004, Calcite twin morphology—a low-temperature deformation geothermometer: Journal of Structural Geology, v. 26, p. 1521-1529.

Fialko, Y., 2006, Interseismic strain accumulation and the earthquake potential on the southern San Andreas fault system: Nature, v. 441, p. 968-971.

Field, E.H., 2007, A summary of previous working groups on California earthquake probabilities: Bulletin of the Seismological Society of America, v. 97, p. 1033-1053.

Finzi, Y., Hearn, E.H., Ben-Zion, Y., and Lyakhovsky, V., 2009, Structural properties and deformation patterns of evolving strike-slip faults—Numerical simulations incorporating damage rheology: Pageoph, v. 166, p. 1537-1573.

Fletcher, K.E.K., Rockwell, T.K., and Sharp, W.D., 2011, Late Quaternary slip rate of the southern Elsinore fault, Southern California—Dating offset alluvial fans via ^{230}Th/U on pedogenic carbonate: Journal of Geophysical Research, v. 116, F02006. DOI

Giggenbach, W.F., 1988, Geothermal solute equilibria. Derivation of Na-K-Mg-Ca geoindicators: Gechimica et Cosmochimica Acta, v. 52, p. 2749-2765.

Graham, D.J., and Midgley, N.G., 2000, Graphical representation of particle shape using triangular diagrams—an Excel spreadsheet method: Earth Surface Processes and Landforms, v. 25, p. 1473-1477.

Grove, M., Lovera, O., and Harrison, M., 2003, Late Cretaceous cooling of the east-central Peninsular Ranges batholith (33°N): Relationship to the La Posta pluton emplacement, Laramide shallow subduction, and forearc sedimentation, *in* Johnson, S.E., Paterson, S.R., Fletcher, J.M., Girty, G.H., Kimbrough, D.L., and Martìn-Barajas, A., eds., Tectonic evolution of northwestern México and the southwestern USA: Boulder, Colorado, Geological Society of America Special Paper 374, p. 355-379.

Hamaker, S.M., 2005, Relationship between fault zone architecture and groundwater compartmentalization in the East Tintic Mining District, Utah: [M.S. Thesis]: Provo, Utah, Brigham Young University, 83 p.

Hartmann, J., Berner, Z., Stuben, D., and Henze, N., 2005, A statistical procedure for the analysis of seismotectonically induced hydrochemical signals: A case study from the Eastern Carpathians, Romania: Tectonophysics, v. 405, p. 77-98.

Hauksson, E., Yang, W., and Shearer, P.M., 2011, Waveform Relocated Earthquake Catalog for Southern California (1981 to 2011), Southern California Earthquake Center Annual Meeting Abstract.

Hayman, N.W., 2006, Shallow crustal fault rocks from the Black Mountain detachments, Death Valley, CA: Journal of Structural Geology, v. 28, p. 1767-1784.

Heath, E.G., Jensen, D.E., and Lukesh, D.W., 1982, Style and age of deformation on the Chino fault, in Cooper, J.D., ed., Neotectonics in southern California: Geological Society of America, 78th Annual Meeting, Cordilleran Section, Volume and Guidebook, p. 123-134.

Heffner, J., and Fairley, J., 2006, Using surface characteristics to infer the permeability structure of an active fault zone: Sedimentary Geology, v. 184, p. 255-265.

Inan, S., Akgul, T., Seyis, C., Saatcilar, R., Baykut, S., Ergintav, S., and Bas, M., 2008, Geochemical monitoring in the Marmara region (NW Turkey): A search for precursors of seismic activity: Journal of Geophysical Research, v. 113, doi: 10.1029/2007/JB005206.

Jahns, R.H., 1954, Investigations and Problems of Southern California Geology, *in* Jahns, R.H., ed., Geology of Southern California, Chapter 1: California Division of Mines, Bulletin 170.

Janecke, S.U., 2009, A "mesh" of crossing faults—Fault networks of southern California: American Geophysical Union Fall Meeting Abstracts, #T31A-1793.

Janecke, S.U., Dorsey, R.J., Forand, D., Steely, A.N., Kirby, S.M., Lutz, A.T., Housen, B.A., Belgarde, B., Langenheim, V.E., and Rittenour, T.M., 2010, High geologic slip rates since Early Pleistocene initiation of the San Jacinto and San Felipe fault zones in the San Andreas fault system—Southern California, USA: Geological Society of America Special Paper 475, 48 p.

Jennings, C.W., and Bryant, W.A., 2010, Fault Activity Map of California: California Geological Survey, Geologic Data Map No. 6, http://www.quake.ca.gov/gmaps/FAM/faultactivitymap.html.

Kairouz, M.E., 2005, Geology of the Whale Peak region of the Vallecito Mountains—Emphasis on the kinematics and timing of the West Salton detachment fault, southern California [M.S. thesis]: Los Angeles, University of California, 156 p.

Karingithi, C.W., 2009, Chemical Geothermometers for Geothermal Exploration: Exploration for Geothermal Resources Short Course, Nov. 1-22.

Kerr, P.F., 1955, Formation and Occurrence of Clay Minerals: Clays and Clay Technology, Bulletin 169, p. 19-32

Kim, Y.-S., Peacock, D.C.P., and Sanderson, D.J., 2003, Mesoscale strike-slip faults and damage zones at Marsalforn, Gozo Island, Malta: Journal of Structural Geology, v. 25, p. 793-812.

Kim, Y.-S., Peacock, D.C.P., and Sanderson, D.J., 2004, Fault damage zones: Journal of Structural Geology, v. 26, p. 503-517, doi: 10.1016/j.jsg.2003.08.002.

Lacombe, O., 2010, Calcite twins, a tool for tectonic studies in thrust belts and stable orogenic forelands: Oil & Gas Science and Technology, Rev. IFP Energies nouvelles, v. 65, p. 809-838.

Lindsey, E.O., and Fialko, Y., 2010, What do formal inversions of space geodetic data tell us about fault slip rates? Examples from Southern California: American Geophysical Union, Fall Meeting Abstracts, #G13A-0668.

Magistrale, H., and Rockwell, T., 1996, The Central and Southern Elsinore Fault Zone, Southern California: Bulletin of the Seismological Society of America, v. 86, p. 1793-1803.

Manga, M., and C.-Y. Wang, 2007, Earthquake hydrology, *in* Schubert, G., ed., Treatise on Geophysics, v. 4, p. 293-320.

Manga, M., and Rowland, J.C., 2009, Response of Alum Rock springs to the October 30, 2007 Alum Rock earthquake and implications for the origin of increased discharge after earthquakes: Geofluids, v. 9, p. 237-250, doi: 10.1111/j.1468-8123.2009.00250.x.

Mathieu, R., and Vieillard, P., 2010, A predictive model for the enthalpies of formation of zeolites: Microporous and Mesoporous Materials, v. 132, p. 335-351.

McCaig, A.M., 1984, Fluid-rock interaction in some shear zones from the Pyrenees: Journal of Metamorphic Geology, v. 2, p. 129-141.

McClay, K., and Bonora, M., 2001, Analog models of restraining stepovers in strike-slip fault systems: American Association of Petroleum Geologists Bulletin, v. 85, p. 233-260.

Micklethwaite, S., and Cox, S.F., 2004, Fault-segment rupture, aftershock-zone fluid flow, and mineralization: Geology, v. 32, p. 813-816.

Miller, J., 1994, Geochemistry, petrography, and structure of the Jurassic Harper Creek and Cuyamaca Reservoir gneisses along the western margin of the CLMSZ, Pine Valley, Southern California, [M.S. Thesis]: San Diego State University, San Diego, California, 165 p.

Mitchell, T.M., and Faulkner, D.R., 2012, Towards quantifying the matrix permeability of fault damage zones in low porosity rocks: Earth and Planetary Science Letters 339-340, p. 24-31.

Odling, N.E., Harris, S.D., and Knipe, R.J., 2004, Permeability scaling properties of fault damage zones in siliclastic rocks: Journal of Structural Geology, v. 26, p. 1727-1747.

Oliver, N.H.S., and Bons, P.D., 2001, Mechanisms of fluid flow and fluid-rock interaction in fossil metamorphic hydrothermal systems inferred from vein-wallrock patterns, geometry and microstructure: Geofluids, v. 1, p. 137-162.

Ottonello, G., 2000, Principles of Geochemistry, New York, Columbia University Press, 894 p.

Peacock, D.C.P., Anderson, M.W., Morris, A., and Randall, D.E., 1998, Evidence for the importance of ‘small’ faults on block rotation: Tectonophysics, v. 299, p. 1-18.

Petersen, M.D., Bryant, W.A., Cramer, C.H., Cao, T., Reichle, M.S., Frankel, A.D., Lienkaemper, J.J., McCrory, P.A., and Schwartz, D.P., 1996, Probabilistic seismic hazard assessment for the State of California: California Department of Conservation, Division of Mines and Geology Open-File Report 96-08 (also U.S. Geological Open-File Report 96-706), 33 p.

Power, W.L., and Tullis, T.E., 1992, The contact between opposing fault surfaces at Dixie Valley, Nevada, and implications for fault mechanics: Journal of Geophysical Research, v. 97, p. 15425-15435.

Ravikumar P., and Somashekar R.K., 2010, Multivariate analysis to evaluate geochemistry of ground water in Varahi river basin of Udupi in Karnataka, India: The Ecoscan, v. 4, p. 153-162

Rothstein, D.A., and Manning, C.E., 2003, Geothermal gradients in continental magmatic arcs: Constraints from the eastern Peninsular Ranges batholith, Baja California, México, *in* Johnson, S.E., Paterson, S.R., Fletcher, J.M., Girty, G.H., Kimbrough, D.L., and Martín-Barajas, A., eds., Tectonic evolution of northwestern México and the southwestern USA: Boulder, Colorado, Geological Society of America Special Paper 374, p. 337–354.

Sadler, P.M., Demirer, A., West, D., and Hilenbrand, J.M., 1993, The Mill Creek Basin, the Potato Sandstone, and fault strands in the San Andreas fault zone south of the San Bernadrdino Mountains: *in* Powell, R.E., Weldon, R.J. II, and Matti, J.C., eds., The San Andreas fault system—Displacement, palinspastic reconstruction, and geologic evolution: Geological Society of America Memoir 178.

Sass, J. and Priest, S., 2002, Geothermal California: Geothermal Resources Council Bulletin, v. 31, p. 183-187.

Savage, H., and Brodsky, E.E., 2011, Collateral damage: Evolution with displacement of fracture distribution and secondary fault strands in fault damage zones: Journal of Geophysical Research, v. 116, doi: 10.1029/2010JB007665.

Schieltz, N.C., and Soliman, M.R., 1966, Thermodynamics of the various high temperature transformations of kaolinite: Thirteenth National Conference on Clays and Clay Minerals, p. 419-428.

Schulz, S.E., and Evans, J.P., 1998, Spatial variability in microscopic deformation and composition of the Punchbowl fault, southern California: Implications for mechanisms, fluid-rock interaction, and fault morphology: Tectonophysics, v. 295, p. 223-244.

Schwenzer, S.P., and Kring, D.A., 2009, Impact–generated hydrothermal alteration on Mars: clay minerals, oxides, zeolites, and more: Lunar and Planetary Science XL: # 1421, Lunar and Planetary Institute, Houston (CD–ROM).

Sheppard, S.M.F., 1986, Characterization and Isotopic Variations in Natural Waters, *in* Valley, J.W., Taylor, H.P., Jr., and O'Neil, J.R., eds., Stable isotopes in high temperature geological processes: Reviews in Mineralogy, v. 16, p. 174.

Shipton, Z.K., and Cowie, P.A., 2003, A conceptual model for the origin of fault damage zone structures in high-porosity sandstone: Journal of Structural Geology, v. 25, p. 333-344.

Shipton, Z.K., Evans, J.P., and Thompson, L.B., 2005, The geometry and thickness of deformation-band fault core and its influence on sealing characteristics of deformation-band fault zones, *in* R. Sorkhabi and Y. Tsuji, eds., Faults, fluid flow, and petroleum traps: AAPG Memoir 85, p. 181-195.

Shirvell, C.R., Stockli, D.F., Axen, G.J., and Grove, M., 2009, Miocene-Pliocene exhumation along the west Salton detachment fault, southern California, from (U-Th)/He thermochronometry of apatite and zircon: Tectonics, v. 28, TC2006.

Sibson, R.H., 1981, Fluid flow accompanying faulting—Field evidence and models, in Simpson, D.W., and Richards, P.G., eds., Earthquake Prediction—An International Review: American Geophysical Union Maurice Ewing Series 4, p. 593-603.

Sibson, R.H., 1987, Earthquake rupturing as a mineralizing agent in hydrothermal systems: Geology, v. 15, p. 701-704.

Sibson, R.H., 1992, Implications of fault-valve behavior for rupture nucleation and recurrence: Tectonophysics, v. 211, p. 283-293.

Solinst, Inc., 2011, Levelogger Gold User Guide v3.4.0: http://www.solinst.com/Prod/3001/Levelogger-User-Guide/12-Manual-Barometric-Comp/12-Barometric-Compensation.html.

Southern California earthquake catalog, 2012, Southern California Earthquake Center Database, http://www.data.scec.org/.

Steely, A.N., Janecke, S.U., Dorsey, R.J., and Axen, G.J., 2009, Early Pleistocene initiation of the San Felipe fault zone, SW Salton Trough, during reorganization of the San Andreas fault system: Geological Society of America Bulletin, v. 121, p. 663-687, doi: 10.1130/B26239.1.

Stipp, M., Stünitz, H., Heilbronner, R., and Schmid, S.M., 2002, The eastern Tonale fault zone—a 'natural laboratory' for crystal plastic deformation of quartz over a temperature range from 250 to 700 °C: Journal of Structural Geology, v. 24, p. 1861-1884.

Suer, S., Gulec, N., Mutlu, H., Hilton, D.R., Cifter, C., and Sayin, M., 2008, Geochemical monitoring of geothermal waters (2002-2004) along the North Anatolian fault zone, Turkey: Spatial and temporal variations and relationship to seismic activity: Pageoph, v. 165, p. 17-43, doi: 10.1007/s00024-007-0294-4.

Todd, V.R., 1977, Geologic Map of Agua Caliente Springs 7.5' Quadrangle, San Diego County, California: U.S. Geological Survey Open-file Report 77-742, 20 p., scale 1:24,000.

Todd, V.R., 2004, Preliminary geologic map of the El Cajon 30' x 60' quadrangle, southern California: U.S. Geological Survey Open-File Report 2004-1341, scale 1:100,000, 30 p.

Treiman, J.A., and Lundberg, M.M., compilers, 1998, Fault number 126, Elsinore fault zone, in Quaternary fault and fold database of the United States: U.S. Geological Survey website, http://earthquakes.usgs.gov/regional/qfaults, (January 2011).

Vaughan, P.J., Moore, D.E., Morrow, C.A., and Byerlee, J.D., 1986, Role of cracks in Progressive Permeability Reduction During Flow of Heated Aqueous Fluids Through Granite: Journal of Geophysical Research, v. 91, p. 7517-7530.

Vaughan, P.R., Thorup, K.M., and Rockwell, T.K., 1999, Paleoseismology of the Elsinore Fault at Agua Tibia Mountain, Southern California: Bulletin of the Seismological Society of America, v. 89, p. 1447-1457.

Vermilye, J.M., and Scholz, C.H., 1998, The process zone: A microstructural view of fault growth: Journal of Geophysical Research, v. 103, p. 12,223-12,237.

Walawender, M.J., Gastil, R.G., Clinkenbeard, J.P., McCormick, W.V., Eastman, B.G., Wernicke, F.S., Wardlaw, M.S., Gunn, S.H., and Smith, B.M., 1990, Origin and evolution of the zoned La Posta-type plutons, eastern Peninsular Ranges batholith, southern and Baja California, *in* Anderson, J.L., ed., The nature and origin of Cordilleran magmatism: Boulder, Colorado, Geological Society of America Memoir 174, p. 1-18.

World Health Organization, Naturally Occurring Hazards, no date, Online Fact Sheet, http://www.who.int/water_sanitation_health/naturalhazards/en/print.html (November 2011)

APPENDICES

APPENDIX A: THIN SECTION DESCRIPTIONS

Sample	Notes
2-1	Significant calcite filling void spaces between preserved angular clasts of quartz and plagioclase; shattered quartz; minor chlorite; a mess
7-1	Angular quartz clasts, twinned plagioclase, biotite; crystals size varies a lot and crystals are shattered/brecciated; quartz is preferentially shattered but some plagioclase too; “Berlin Blue” chlorite (blue in XPL and green in PPL) pseudomorphing biotite; fluid tracks in quartz; heavily brecciated; calcite filling void spaces between preserved clasts of quartz and plagioclase
8-1	Kinked plagioclase & biotite; large quartz crystals
10-1	Quartz subgrains; subhedral crystals; plagioclase, biotite, quartz; kinked and zoned plagioclase; biotite altering to chlorite
10a-2	Rust-colored biotite veins enclosing angular clasts of preserved quartz and plagioclase; shattered quartz; overall clast sizes are small; entrained biotite with associated cataclasite zone up to 720 μm wide containing clasts up 10 109 μm wide; beyond the cataclasite adjacent to the entrained biotite is another cataclasite containing clasts up to ~3 mm.
10-2	Biotite parallel veins/foliation/alignment; fragments of quartz and plagioclase crystals; some chlorite in biotite; shattered quartz; aggregates of clasts; anastomosing biotite veins
11-1	Chlorite within biotite crystals; quartz, plagioclase; large crystals; zoned plagioclase; minor hornblende adjacent to chlorite pseudomorphing biotite; minor allanite, muscovite, and epidote
12-1	Beautiful large crystals of biotite, zoned plagioclase, subgrained quartz, and some chlorite
13-1	Similar to 12-1; chlorite pseudomorphing biotite crystals; sericitization of kinked and resorbed plagioclase; subgrained quartz; minor allanite
14-1	Large crystals of plagioclase, quartz, and biotite; small chlorite
14a	Calcite fills fractures; rock heavily crushed; broken; plagioclase, biotite, quartz; some chlorite; subgrained; sutures; kinks; some dirty plagioclase crystals; minor allanite and epidote
15-2	Quartz subgrains; kinked plagioclase and biotite; tiny chlorite; few calcite-filled fractures
16-1	Cataclasite, possibly two or more generations; small angular clasts composed of smaller angular clasts; calcite forms some linear pathways around preserved fragments of quartz, plagioclase, and biotite; open fractures often in center of sheared biotite zones; biotite shear zones are parallel to one another
17-1	Foliated shearing; large aggregates and many small angular clasts encompassed within biotite shear zones; intact biotite crystals are often kinked; shattered quartz; grain sizes vary; minor remnant epidote
18-2	Large crystals of plagioclase, quartz, and biotite; biotite appears “eaten into”; shattered quartz; through-going fractures filled with calcite; minor allanite

19-2	Calcite-filled fractures; large quartz, plagioclase, and biotite crystals; sub-grained quartz
22	Quartz and plagioclase crystals are heavily fractured and shattered; anhedral biotite; calcite beginning to fill fractures
25	Fractures through quartz and plagioclase; biotite is eaten away along edges; calcite-filled fractures; quartz and biotite shards strewn along a fractures; quartz contains subgrains; minor amounts of epidote
27	Pegmatite; very large quartz and plagioclase; subgrained quartz; calcite veins
28	Mess of quartz, plagioclase, and biotite; fractured; zoned plagioclase; some calcite in fractures
33	Calcite in fractures; typical grains of quartz, plagioclase, and biotite
37	Large crystals of plagioclase, quartz, and biotite; many calcite veins even inside quartz cracks; fluid inclusions and subgrains in quartz
40	Chlorite inside biotite; quartz and zoned plagioclase; fluid inclusion path-ways; little to no calcite
41	Subgrained quartz, zoned plagioclase, biotite; suturing in quartz
44	Gnarly and beat-up; very fractured; quartz veins; dirty crystals; plagioclase; quartz , biotite; chlorite
46	Very altered; epidote vein; many, many chlorite crystals; quartz, sericitization of plagioclase, biotite, chlorite pseudomorphs after biotite; heavily fractured and altered; sutured and subgrained quartz; euhedral biotite
48	Bimodal grain sizes; large crystals and small fragments of quartz, plagio-clase, and biotite; kinked biotite; biotite smeared along fracture; beautiful twinning in plagioclase; subgrained quartz; yellow allanite (XPL); schmutzy biotite
49	Minor fractured hornblende; wispy bands in biotite; subgrained and partially shattered quartz; through-going fractures; kinked plagioclase and biotite; larger grains; biotite schmutz in fractures; altered and dirty; minor allanite and epidote are present but plagioclase, biotite, and quartz crystals are pris-tine and large
52	Altered schmutz in cracks; eating away inside plagioclase; large quartz, pla-gioclase, and biotite crystals; fluid inclusion pathways; kinked biotite; minor allanite; minor epidote clusters
53	Chlorite; plagioclase, quartz, and biotite; zoned plagioclase; subgrained quartz; plagioclase cores are altered; chlorite pseudomorphing biotite; minor epidote
55	Chlorite; large quartz crystals and plagioclase clusters; some sericitization of plagioclase; corrosion and alteration but not throughout; biotite; kinked plagioclase; subgrained quartz; quartz veins; calcite; minor fragments of hornblende; minor epidote and allanite

58	Chlorite, biotite, plagioclase, and quartz; chlorite altering biotite; subgrained quartz; zoned plagioclase; large crystals; alteration not confined to certain zones; large quartz clusters; sutures; fractures in quartz; not shattered though; minor amounts of allanite
61	Quartz subgrained; plagioclase zoned; biotite and some chlorite pseudomorphing biotite; some alteration; kinked biotite; suturing
70	Sericitized plagioclase and fractured rock; quartz veins; shattered; kinked plagioclase and biotite; chlorite; epidote cluster
72	The plagioclase crystals are heavily altered and corroded while the quartz crystals are not; they have fluid pathways and fractures and are split by fractures (filled with chlorite); very few biotite remaining and only in smeared form; calcite (?) in quartz crystal; epidote clusters; minor allanite
73	Biotite, chlorite, large and small grains of quartz and plagioclase; allanite and epidote; zoned plagioclase; subgrained quartz; kinked biotite; some calcite in fractures; rock looks pretty intact
74	Kinked biotite; large quartz and plagioclase crystals; fractured hornblende clusters with biotite; sericitization of plagioclase; some calcite; chlorite from biotite but not much; still large biotite crystals; subgrained quartz; minor epidote
75	Kinked plagioclase and biotite; zoned plagioclase; kind of dirty sample; fractured, sutured, and subgrained quartz; large crystals; some chlorite; euhedral zoned epidote crystal and minor scattered anhedral epidote clusters
78	Quartz, plagioclase, biotite, and some chlorite; kinked biotite and plagioclase; subgrained, sutured, and fractured quartz; fluid pathways; a little altered and gunky; zoned plagioclase; small quartz veins; sub- to euhedral hornblende crystal; minor allanite clusters
83	A little dirty; plagioclase, quartz, and lots of biotite; very little chlorite; kinks; subgrains; fractures; zoned plagioclase; sutures in quartz
84	Cataclasite; possibly two (or more) generations of cataclasis; natural red iron stain; contains clasts of quartz clusters; very few plagioclase and biotite